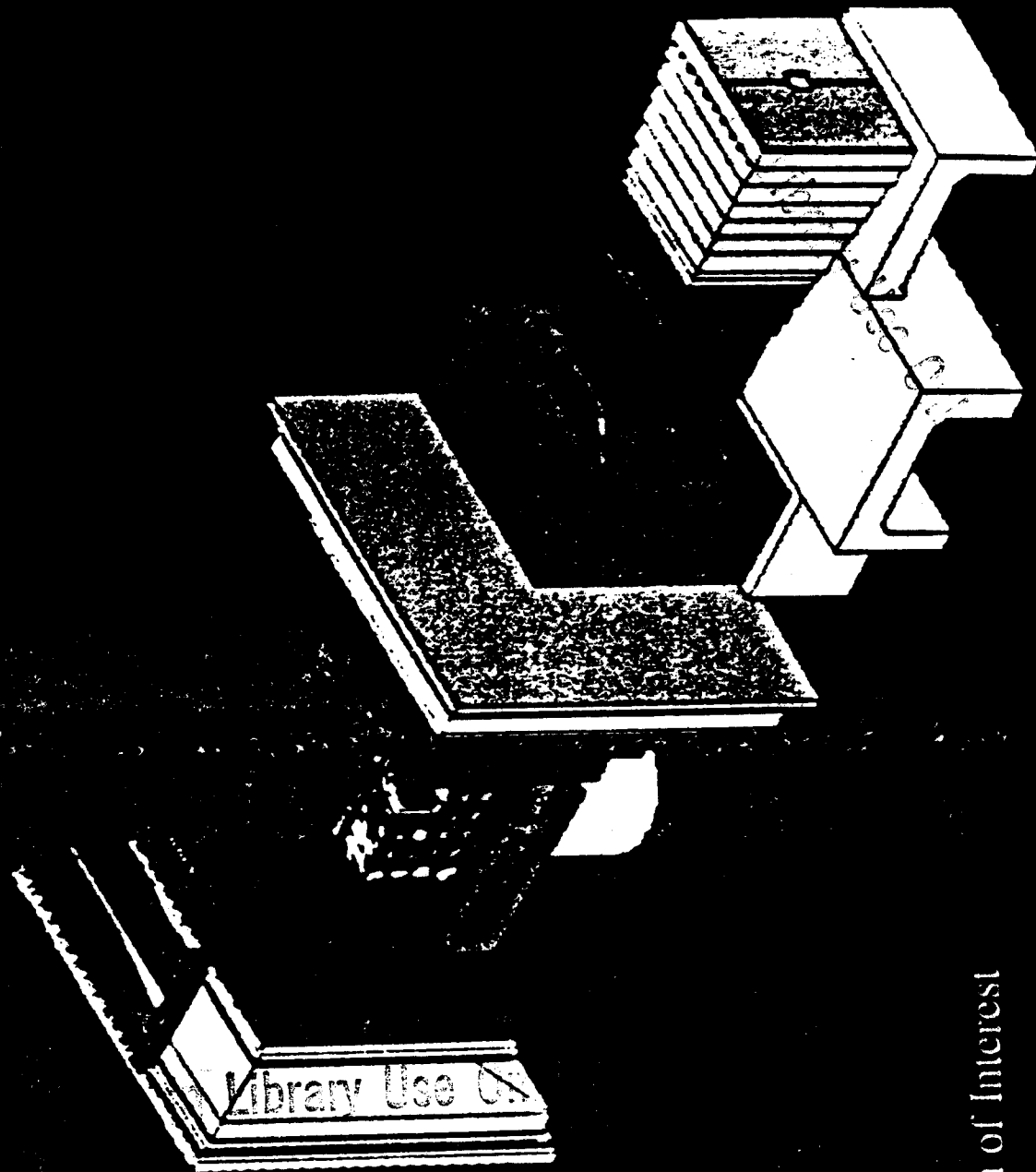


SSCL-SR-1163  
SSC-E01008

# Bottom Collider Detector



Expression of Interest

# Expression of Interest for A Bottom Collider Detector at the SSC

(May 25, 1990)

## Executive Summary

This Expression of Interest describes a physics program to collect and analyze a sample of  $> 10^{12}$   $B\bar{B}$  pairs. The emphasis is on the study of  $CP$  violation in the Standard Model via direct measurements of CKM-matrix elements. This physics occurs at low transverse momentum and over a broad rapidity range, which complements the program of other SSC experiments that explore high- $P_t$  and high mass.

The Bottom Collider Detector (BCD) incorporates all features needed for reconstruction of a  $B\bar{B}$  pair via charged secondaries. A spectrometer based on a large dipole magnet covers the central seven units of pseudorapidity while a single forward arm extends the coverage by two units. The detector design emphasizes 3-D vertex reconstruction, precise momentum measurement,  $e/\mu/\pi/K/p$  identification at low transverse momenta, and excellent mass resolution at the  $B$  mass. Hadron calorimetry is not needed since jet mass and missing  $E_t$  are not important for  $B$  physics at low  $P_t$ . The detector will be triggered on  $J/\psi$  decay into leptons, on single leptons, and on separated vertices. The trigger design places emphasis on software triggers in general-purpose processors.

The Bottom Collider Detector addresses physics within the context of the Standard Model, and physics outside the Standard Model. The former includes the study of  $B$ -meson and -baryon production and decay, gluon structure functions at low  $x$ ,  $B_s$  mixing,  $CP$  violation, and intermediate  $P_t$ -physics such as  $H \rightarrow b\bar{b}$ . Physics outside the Standard Model includes searches for exotic  $B$  decays, and for  $CP$  violation in modes where the Standard Model prediction is zero.

**Members of the BCD collaboration are:**

H. Castro, B. Gomez, F. Rivera, J.-C. Sanabria, *Universidad de los Andes*  
J.F. Arens, G. Jernigan, *U.C. Berkeley, Space Sciences Lab*  
P. Yager, *U.C. Davis*  
S. Childress, L.A. Garren, H. Jöstlein, S. Kwan, P. Lebrun, J. Morfin, L. Stutte, *Fermilab*  
P. Avery, J. Yelton, *U. Florida*  
K. Lau, *University of Houston*  
M. Adams, D. McLeod, C. Halliwell, *U. Illinois, Chicago*  
R. Burnstein, H. Rubin, *Illinois Institute of Technology*  
E.R. McCliment, Y. Onel, *U. Iowa*  
D. W. Kim, *Kang Reung National College*  
D. Son, *Kyungpook National University*  
Y.M. Park, *Kyungsung U.*  
D. London, *U. Montreal*  
M.S. Alam, A. Deogirikar, W. Gibson, *S.U.N.Y. at Albany*  
G. Alverson, W. Faissler, D. Garelick, M. Glaubman, I. Leedom, S. Reucroft,  
*Northeastern U.*  
S.K. Willis, *Northern Illinois University*  
C.L. Britton, K. Castleberry, C. Nowlin, C. Sohns, *Oak Ridge National Lab*  
P. Gutierrez, G.R. Kalbfleisch, D.H. Kaplan, P. Skubic, J. Snow, *U. Oklahoma*  
L.D. Gladney, N.S. Lockyer, K. Ragan, R. Van Berg, *U. Pennsylvania*  
D.J. Judd, D.E. Wagoner, K. Paick, L. Turnbull, *Prairie View A&M U.*  
J.G. Heinrich, C. Lu, K.T. McDonald, M.V. Purohit, *Princeton U.*  
A.M. Lopez, J.C. Palathingal, A. Mendez, J. Millan, R. Palomera-Garcia, *Universidad de Puerto Rico*  
B. Hoeneisen, C. Marin, C. Jimenez, *Universidad San Francisco de Quito*  
R. Stefanski, H. Fenker, L.A. Roberts, *SSC Laboratory*  
M. Sheaff, *U. Wisconsin*  
P.E. Karchin, A.J. Slaughter, E. Wollin, *Yale University*

**Industrial collaborators:**

A. Pitas, *Baker Manufacturing*  
J. Cooper, *E-Systems Garland Division*  
G. Kramer, C. Pfeiffer, S. Augustine, *Hughes Aircraft Company*  
J. Rattner, *Intel Scientific Computers*

# Contents

<b>1</b>	<b>Introduction</b>	<b>1</b>
<b>2</b>	<b><i>B</i> Physics at the SSC</b>	<b>2</b>
2.1	Nonleptonic Decay Modes of the <i>B</i> Mesons . . . . .	5
2.2	$B_s$ - $\bar{B}_s$ Mixing . . . . .	14
2.3	<i>CP</i> Violation in Self-Tagging <i>B</i> Decays . . . . .	16
2.4	<i>CP</i> Violation in Decays of Neutral <i>B</i> 's to <i>CP</i> Eigenstates . . . . .	18
2.4.1	A <i>CP</i> Primer . . . . .	18
2.4.2	Sensitivity of the BCD to CKM Phase . . . . .	27
2.5	Gluon and Sea-Quark Distributions at Small $x$ . . . . .	29
<b>3</b>	<b>Detector Overview</b>	<b>30</b>
3.1	Detector Subsystems . . . . .	34
<b>4</b>	<b>Detector Description</b>	<b>39</b>
4.1	Silicon Vertex Detector . . . . .	39
4.1.1	Overview . . . . .	39
4.1.2	Geometrical Layout . . . . .	40
4.1.3	Beam-to-Detector Distance . . . . .	40
4.1.4	Detector Segmentation . . . . .	43
4.1.5	Silicon <i>p-i-n</i> Detectors . . . . .	44
4.1.6	Readout Electronics . . . . .	46
4.1.7	Radiation Damage . . . . .	46
4.1.8	Mechanical and Thermal Stability . . . . .	47
4.1.9	Data Transmission . . . . .	48
4.1.10	Data Processing . . . . .	48
4.1.11	Simulations of Vertex-Detector Performance . . . . .	48
4.2	Straw-Tube Tracking System . . . . .	50
4.2.1	Mechanical Design . . . . .	50
4.2.2	Electronics . . . . .	51
4.2.3	Momentum Resolution . . . . .	53
4.2.4	Straw Tracking Simulation Study . . . . .	53
4.3	Time-of-Flight System . . . . .	59
4.3.1	Introduction to Hadron Identification . . . . .	59
4.3.2	The Time-of-Flight System . . . . .	61
4.4	Ring Imaging Čerenkov Counters . . . . .	62
4.4.1	The Čerenkov Radiator . . . . .	62
4.4.2	The Photodetector . . . . .	65
4.4.3	Readout . . . . .	66
4.5	Transition Radiation Detectors . . . . .	68
4.5.1	Overview of Electron Identification . . . . .	68
4.5.2	Transition Radiation Detector . . . . .	71
4.6	Electromagnetic Calorimeter . . . . .	74

4.7	Muon Detector . . . . .	76
4.7.1	Overview . . . . .	76
4.7.2	Detector Layout . . . . .	77
4.7.3	Radiation Damage Consideration for the Muon Chambers . . . . .	80
4.7.4	Backgrounds . . . . .	80
4.7.5	Muon Momentum Resolution . . . . .	82
4.7.6	Single Muon Rates . . . . .	82
4.8	Luminosity Monitor . . . . .	84
<b>5</b>	<b>Triggers and Data Acquisition</b>	<b>84</b>
5.1	Introduction . . . . .	84
5.2	Triggers . . . . .	85
5.2.1	Electron Trigger . . . . .	85
5.2.2	Prompt Muon Trigger . . . . .	86
5.2.3	Prompt High Luminosity $J/\psi$ Trigger . . . . .	86
5.2.4	Secondary-Vertex Trigger . . . . .	86
5.3	Data-Acquisition Architecture . . . . .	86
5.4	Archival Mass Storage . . . . .	89
5.5	Offline Computing Needs . . . . .	90
<b>6</b>	<b>Collision Hall</b>	<b>90</b>
<b>7</b>	<b>An Interim Experiment</b>	<b>92</b>
<b>8</b>	<b>Milestones and Schedule</b>	<b>93</b>
<b>9</b>	<b>Request for R&amp;D Support</b>	<b>93</b>
9.1	Vertex Detector . . . . .	93
9.2	Time of Flight . . . . .	93
9.3	Trigger Simulation . . . . .	95
9.4	RICH . . . . .	95
9.5	Computing . . . . .	96
<b>10</b>	<b>Cost Estimate</b>	<b>96</b>
<b>11</b>	<b>References</b>	<b>99</b>

## List of Figures

1	Preliminary signal for $B \rightarrow J/\psi K$ from CDF. . . . .	1
2	The unitarity triangle . . . . .	4
3	Graphs for nonleptonic decays of $B$ mesons. . . . .	6
4	$\eta$ and $P_i$ for $B$ -decay products. . . . .	10
5	Allowed regions of the $\sin 2\varphi_i$ . . . . .	25
6	Isometric view of the BCD. . . . .	32

7	Section View of the BCD. . . . .	33
8	Possible beam-pipe configuration. . . . .	34
9	Distribution in polar angle for particles from $B$ -decay. . . . .	41
10	Arrangement of wafers in the silicon vertex detector. . . . .	42
11	Multihit-confusion probability in the vertex detector. . . . .	44
12	A $B$ event in the vertex detector . . . . .	45
13	Mass plot of non- $B$ vertices . . . . .	49
14	Possible layout of the Central straw-tube tracker. . . . .	52
15	Straw-tube endplug. . . . .	52
16	Momentum resolution in the tracking system. . . . .	54
17	View of an alternative straw tracking system. . . . .	55
18	A typical event in the straw-tube system. . . . .	58
19	Found minivectors in a typical event. . . . .	58
20	Reconstructed invariant mass from $B \rightarrow \pi^+ \pi^-$ . . . . .	59
21	Integral momentum spectra. . . . .	60
22	The multistep avalanche chamber. . . . .	65
23	The wedge and strip pad readout. . . . .	67
24	Resistive pad readout scheme. . . . .	67
25	Rate of Electrons. . . . .	69
26	Three modules of the TRD. . . . .	74
27	The Central TRD. . . . .	75
28	Electronics for the Electromagnetic Calorimeter. . . . .	76
29	PVC Streamer Tube Module . . . . .	79
30	Data-acquisition architecture, I. . . . .	85
31	Data-acquisition-system architecture, II. . . . .	87
32	The barrel-switch event builder. . . . .	88
33	Distributed Event Builder Model . . . . .	89
34	Possible data-acquisition archival capacities. . . . .	90
35	BCD Experimental Hall. . . . .	91
36	A mini-BCD at Fermilab. . . . .	92
37	BCD Schedule. . . . .	94

## List of Tables

1	$B$ - $\bar{B}$ production at various colliders . . . . .	3
2	The 21 basic nonleptonic decay modes of the $B_u$ . . . . .	7
3	The 28 basic nonleptonic decay modes of the $B_d$ . . . . .	8
4	The 29 basic nonleptonic decay modes of the $B_s$ . . . . .	9
5	Geometric acceptance for single $B$ decays. . . . .	11
6	Acceptance for a tagging $B$ decays. . . . .	11
7	Geometric acceptance for tagged $B$ decays. . . . .	12
8	Extended acceptance for tagged $B$ decays. . . . .	12
9	Rate estimates for reconstructed $B$ decays. . . . .	14
10	Rate estimates for self-tagging $B$ decays. . . . .	18

11	Minimum $\sin 2\varphi$ resolvable in the BCD. . . . .	29
12	Multiple scattering versus $\eta$ . . . . .	42
13	Strip sizes for the vertex detector. . . . .	43
14	Momentum coverage of the RICH counters. . . . .	60
15	Momentum coverage of the time-of-flight system. . . . .	61
16	Parameters of the RICH counters. . . . .	64
17	Electron Rates from Various Sources . . . . .	70
18	Efficiency and rejection of a TRD. . . . .	72
19	Physical properties of the TRD. . . . .	73
20	Single Muon Rates. . . . .	83
21	Vertex Detector R&D Costs . . . . .	95
22	Summary of R&D Costs . . . . .	97
23	Cost estimate. . . . .	98

# 1 Introduction

The SSC is a prolific bottom factory, with  $B$ -pair production rates orders of magnitude larger than at any other existing or proposed machine. As such, it will provide a unique opportunity for a comprehensive study of  $CP$  violation in the  $B-\bar{B}$  system.<sup>[1, 2, 3, 4, 5]</sup> Such a study will either confirm and refine the Standard Model, or be a sensitive indicator of new physics. In addition, copious production of top and other intermediate-mass states decaying into bottom are expected at the SSC.

The design of the Bottom Collider Detector (BCD) is tailored to probe transverse momenta of order of the  $b$ -quark mass, i.e., low- and intermediate- $P_t$  physics at the SSC. The forward production of relatively light particles, with masses less than 1% of the machine energy (40 TeV), can be well analyzed in a dipole magnetic spectrometer which emphasizes 3-D vertex reconstruction, precision tracking and momentum analysis, particle identification (leptons, kaons, protons...) and a high-rate data-acquisition system.

In proposing detailed studies of  $B$  physics at the SSC we must extract the  $B$ -meson signal in an environment often considered less favorable than at an  $e^+e^-$  collider. Experimental evidence that this is possible is now available in a recent, preliminary result of the CDF collaboration in which  $16 \pm 6$  events have been reconstructed from the decay chain  $B^\pm \rightarrow J/\psi K^\pm \rightarrow \mu^+\mu^- K^\pm$ , as shown in Fig. 1. This is the largest sample of  $B \rightarrow J/\psi X$  decays reconstructed in any experiment to date.

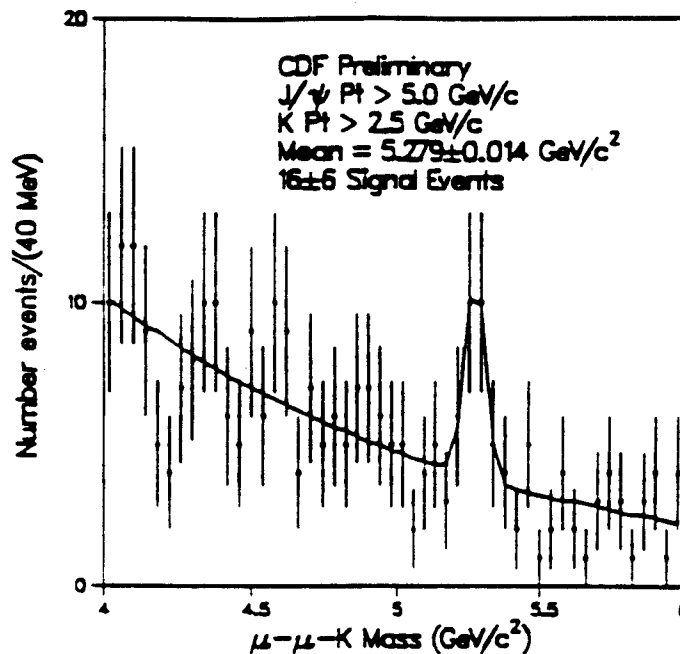


Figure 1: Preliminary analysis of the CDF collaboration showing reconstruction of the decay chain  $B^\pm \rightarrow J/\psi K^\pm \rightarrow \mu^+\mu^- K^\pm$ .



## 2 *B* Physics at the SSC

Several developments during the 1980's indicate that *B*-meson physics will be a rich topic for study at the SSC:

- The *B*-meson lifetime was first measured by the MAC<sup>[6]</sup> and Mark II<sup>[7]</sup> groups to be 1.2 picoseconds, which is longer than that for *D* mesons. Thus with the use of a silicon vertex detector, perfected during the early 1980's, charged secondaries from *B*-meson decay can be isolated from the primary interaction vertex. This will permit *B* physics to be done at a hadron collider, but with the important restriction that complete reconstruction will typically be possible only for all-charged decay modes.
- The cross section for  $b\bar{b}$  pairs in hadron-hadron interactions is enhanced by order- $\alpha_s^3$  QCD corrections<sup>[8]</sup> and is anticipated to be approximately 500  $\mu$ barn at the SSC. This is nearly  $10^6$  times larger than the cross section for  $b\bar{b}$  production for an  $e^+e^-$  collider operating at the  $\Upsilon(4s)$  resonance.
- The  $B_d^0$ - $\bar{B}_d^0$  mixing parameter,  $x_d = \Delta M/\Gamma$ , has been measured at Argus<sup>[9]</sup> (and subsequently at CLEO<sup>[10]</sup>) to be about 0.7. This demonstrates that the neutral *B*-meson system, like the neutral kaon system, is rich in quantum-mechanical phenomena.
- It is expected that *CP* violation in the decays of neutral *B* mesons to *CP* eigenstates will have an especially clean interpretation. Such decays, when dominated by a single weak amplitude, exhibit *CP* violation via interference due to mixing, which results in an effect directly dependent on a phase of a CKM-matrix element without strong-interaction ambiguities. However, it is probable that discovery of this type of *CP* violation will require a sample of  $10^8$  reconstructible *B* decays. Detailed exploration of consistency of the Standard Model explanation of *CP* violation will require at least 100 times more events, possible only at the SSC.

We are embarking on a long-range program, initiated at Fermilab<sup>[11]</sup> and continuing at the SSC, with the ultimate goal being the detailed investigation of *CP* violation in the *B*- $\bar{B}$  system. Of all known phenomena, we believe that the existence of *CP* violation provides the clearest indication that new physics is to be found at energy scales above 1 TeV.

Speculations about the role of *CP* violation encourage study of the phenomena outside its present preserve in the  $K^0$ - $\bar{K}^0$  system:

- Cosmological models that try to explain the matter-antimatter asymmetry in the universe usually invoke *CP* violation and some Grand Unified Theory. Thus the existence of the universe is thought to be related to *CP* violation in some way. Further study is justified on these grounds alone.
- Multiple Higgs bosons can lead to relative complex phases that in turn have *CP*-violating effects. Thus the understanding of mass generation and *CP* violation is related.

- $CP$  violation is relevant to the generation puzzle. Of the 21 free parameters in the standard model, 18 are related to the fact that we have 3 generations of families. If there were two families, no complex phase would exist in the standard model and thus no simple explanation of  $CP$  violation. With 3 families, there is one complex phase, and this is consistent with present data. If there are 4 families, then there are 3 complex phases and new  $CP$  phenomena might be expected. Phenomena involving the  $b$ -quark of the third generation should reveal the origin of  $CP$  violation more clearly than in the  $K-\bar{K}$  system.
- Measurements of  $CP$  violation in the  $B-\bar{B}$  system (unlike the  $K-\bar{K}$  system) can determine CKM angles with little strong-interaction uncertainty. By the study of several  $B$ -decay modes, the CKM system can be overconstrained.
- When the CKM elements are well determined it may be possible to deduce regularities in the mass matrices of the quarks, and hence among their Yukawa couplings. This is an approach that might lead to discovery of a higher symmetry beyond the present standard model.
- Left-right symmetric models predict smaller  $CP$ -violating effects in the  $B-\bar{B}$  system than does the standard model.

The greatest opportunity to explore  $CP$  violation in a new way, via the  $B-\bar{B}$  system, is at a hadron collider such as the SSC. As summarized in Table 1, the cross-section for  $B$ -meson production is about 0.5 millibarn, nearly  $10^6$  times larger at the SSC than at the  $\Upsilon(4S)$  resonance at an  $e^+e^-$  collider. One in every 200 events at the SSC will contain a  $B-\bar{B}$  pair. A comprehensive study of  $CP$  violation requires the production of approximately  $10^{12}$   $B-\bar{B}$  pairs, possible at the SSC in one year of running at a luminosity of  $10^{32}$   $\text{cm}^{-2}\text{sec}^{-1}$ , which corresponds to a total interaction rate of 10 MHz.

Table 1:  $B-\bar{B}$  production at various colliders.

Collider	$\sqrt{s}$ (TeV)	$\sigma_{b\bar{b}}$ ( $\mu\text{b}$ )	$\sigma_{b\bar{b}}/\sigma_{\text{tot}}$	$\mathcal{L}_{\text{ave}}$ ( $\text{cm}^{-2}\text{sec}^{-1}$ )	$N_{b\bar{b}}/10^7$ sec
TEV I	1.8	45	1/1000	$5 \times 10^{31}$	$2 \times 10^{10}$
SSC	40	500	1/200	$10^{32}$	$5 \times 10^{11}$
CESR	0.01	0.001	1/5	$10^{33}$	$10^7$
LEP	0.09	0.005	1/7	$10^{32}$	$5 \times 10^6$

The study of  $CP$  violation in the  $B-\bar{B}$  system can be accomplished by measurement of an asymmetry in the decay of  $B$  mesons to all-charged final states:

$$A = \frac{\Gamma(B \rightarrow f) - \Gamma(\bar{B} \rightarrow \bar{f})}{\Gamma(B \rightarrow f) + \Gamma(\bar{B} \rightarrow \bar{f})}$$

While the asymmetry  $A$  may be as large as 30% (even after dilution due to  $B$ - $\bar{B}$  mixing), this likely occurs only in modes with branching fractions  $\Gamma \sim 10^{-8}$ . This requires at least  $10^8$  reconstructible decays for a significant signal to be discerned. Further, the cleanest signals are for modes with  $f = \bar{f}$ , so the particle-antiparticle character of the parent  $B$  must be 'tagged' by observation of the second  $B$  in the interaction. Of course, a detailed study should include measurement of asymmetries in several different decay modes.

Some of the elegance of measurements in the  $B$ - $\bar{B}$  system may be inferred from consideration of the CKM matrix (in the Wolfenstein notation):

$$V_{CKM} = \begin{pmatrix} V_{ud} & V_{us} & V_{ub} \\ V_{cd} & V_{cs} & V_{cb} \\ V_{td} & V_{ts} & V_{tb} \end{pmatrix} \approx \begin{pmatrix} 1 & \lambda & A\lambda^3(\rho - i\eta) \\ -\lambda & 1 & A\lambda^2 \\ A\lambda^3(1 - \rho - i\eta) & -A\lambda^2 & 1 \end{pmatrix}.$$

Parameter  $\lambda$  is essentially the Cabibbo angle,  $A$  is known via the  $B$  lifetime, while  $\eta \neq 0 \leftrightarrow CP$  violation. But,  $\rho$  and  $\eta$  are not well determined from the  $K$ - $\bar{K}$  system. Rather, the  $B$ - $\bar{B}$  system will be the place for detailed measurements of these parameters.

Further, unitarity of  $V_{CKM}$  implies

$$V_{ud} + \lambda V_{ts} + V_{ub}^* \approx 0.$$

Hence if these three complex matrix elements are regarded as vectors they form a closed triangle in the complex plane. On dividing their lengths by  $A\lambda^3$ , we obtain the picture of Figure 2 in the  $(\rho, \eta)$  plane. Since the base is known, the experimental challenge of measuring the amplitudes  $V_{ub}$  and  $V_{ud}$  is equivalent to measuring the three interior angles  $\varphi_1, \varphi_2, \varphi_3$ .

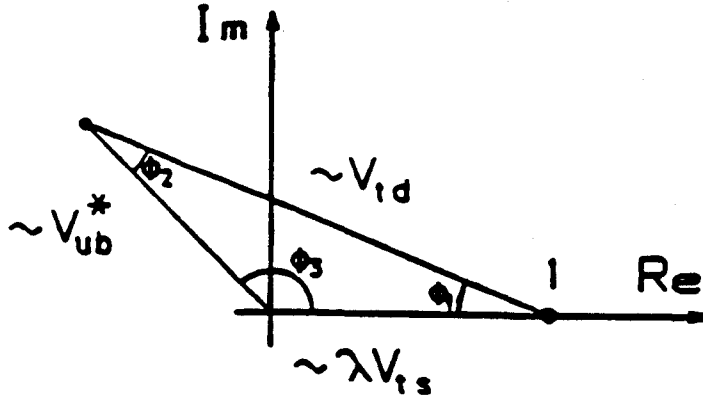


Figure 2: The unitarity triangle.

A favorable theoretical result is that for decays  $B \rightarrow f$  with  $f$  a  $CP$  eigenstate, the asymmetry  $A$  depends only on one of the angles  $\varphi_i$ :

$$A \sim \sin 2\varphi_1 \text{ for } B_d^0 \rightarrow J/\psi K_S, D\bar{D}, \text{ and } D_s^+ D_s^-.$$

$$A \sim \sin 2\varphi_2 \text{ for } B_d^0 \rightarrow \pi^+ \pi^-, K^+ K^-, \text{ and } \rho^0 K_S.$$

$$A \sim \sin 2\varphi_3 \text{ for } B_d^0 \rightarrow \rho^0 K_S, \pi^+ \pi^-, \text{ and } K^+ K^-.$$

Hence the experimentally accessible asymmetries rather directly measure the  $V_{CKM}$  amplitudes. It will require a general purpose, low- $P_t$  detector to take full advantage of this splendid opportunity.

The program to measure  $CP$  violation in the  $B-\bar{B}$  system is ambitious. There will be four phases to this program, some of which will likely be accomplished in part prior to the SSC:

1. Study of the branching ratios of nonleptonic decay modes of  $B$  mesons and baryons. From the associated measurement of  $\sigma_{b\bar{b}}$  at a hadron collider will come determinations of the gluon structure function at very low  $x$ . The BCD will produce even larger samples of decays of charmed-particles.
2. Study of  $B_s-\bar{B}_s$  mixing, which is expected to be quite large, and hence difficult to observe due to the rapid oscillations. At a hadron collider the  $B$ 's are produced with sufficient laboratory energy that their time evolution may be observed in detail. (Only  $e^+e^-$  colliders more ambitious than those in Table 1 could resolve this mixing.)
3. Study of  $CP$  violation in decays  $B \rightarrow f$  where  $f \neq \bar{f}$ , which does not require tagging of the other  $B$  in the event. This might provide the first evidence of  $CP$  violation in the  $B$ -meson system, but the interpretation of the results will be subject to theoretical uncertainty from strong-interaction effects.
4. Study of  $CP$  violation in decays of neutral  $B$  mesons to  $CP$  eigenstates, which will provide the critical test of our understanding of  $CP$  violation in the Standard Model. This difficult but rewarding task sets the standards for detector performance of the  $B$ -physics program.

In the following four subsections we elaborate on each of the four aspects of the  $B$ -physics program.

## 2.1 Nonleptonic Decay Modes of the $B$ Mesons

A survey of seven possible graphs describing  $B$ -meson decay indicates that the  $B_u$  will have 21 basic 2-body nonleptonic decays, the  $B_d$  will have 28, and  $B_s$  will have 29 (see Tables 2-4). This contrasts with the case for the  $K_u (= K^+)$  and  $K_d (= K^0)$  which each only have 2 such decays (not all distinct!). In the  $B$  system there are 26 basic decays to  $CP$  eigenstates compared to the 2 in the  $K$  system. All 79 of the basic two-body decays of the  $B$  system have all-charged final states (at some price in secondary branching fraction), while only 1 of the basic  $K$  decays is all charged.

We have not displayed the catalog of decays of the  $B_c^+ (= \bar{b}c)$ , which decays to such states as  $D^+\bar{D}^0$  and  $J/\psi\pi^+$ . Both the  $B_s$  and the  $B_c$  will be better studied at a hadron collider than at a low-energy  $e^+e^-$  collider.

The Tables refer to seven kinds of graphs, two spectator, annihilation, exchange, penguin/annihilation, and two penguin/spectator, as shown in Fig. 3. We can roughly estimate that for graphs I and II

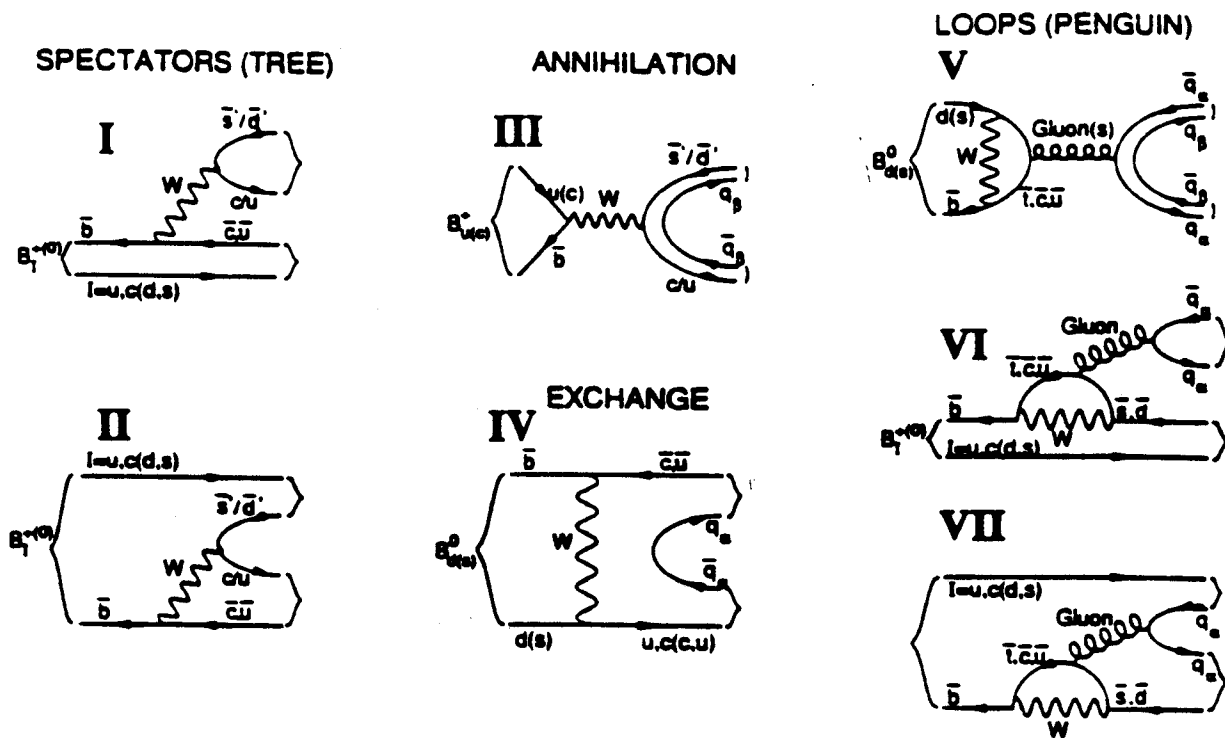


Figure 3: Seven graphs for the nonleptonic decays of  $B$  mesons. The dashed lines are  $W$  bosons; gluons are not shown.

CKM-favored decays have branching fractions of  $10^{-2}$ - $10^{-3}$ ;

CKM-suppressed decays have branching fractions of  $3 \times 10^{-4}$ - $3 \times 10^{-5}$ ;

CKM-doubly-suppressed decays have branching fractions of  $10^{-6}$ - $10^{-8}$ .

Graphs III-VII are typically suppressed by an additional factor of 0.1-0.01 compared to graphs I and II of the same CKM coupling. However,  $D$ -meson decays show some cases where graphs III-VII give large amplitudes.

The two-body final states listed in the Tables are representative of the particular  $q\bar{q}/q\bar{q}$  combination for each entry. All final states could be augmented by  $n(\pi^+\pi^-)$ , with possibly larger branching fractions. Likewise, every spin-0 final-state particle could be replaced by its spin-1 partner, and *vice versa*. Typically the branch to the spin-1 meson will be 3 times that to the spin-0 partner.

The secondary decays used in constructing the last column of the Tables are:

Decay Mode	Branching Ratio
$K_S^0 \rightarrow \pi^+\pi^-$	0.69
$\rho^0 \rightarrow \pi^+\pi^-$	1.00
$K^{*0} \rightarrow K^+\pi^-$	0.67
$\phi \rightarrow K^+K^-$	0.50
$D^+ \rightarrow K^-\pi^+\pi^+$	0.08
$D^0 \rightarrow K^-\pi^+$	0.04
$D_s^+ \rightarrow \phi\pi^+$	0.03
$D_s^+ \rightarrow \phi\pi^+\pi^+\pi^-$	0.04

Table 2: The 21 basic 2-body nonleptonic decays of the  $B_u^+$  ( $= \bar{b}u$ ). Figure 3 illustrates the seven types of graphs. The subscripts  $F$ ,  $S$ , and  $D$  to the type of graph in this and following two tables refer to CKM-favored, -suppressed, and -doubly-suppressed, respectively.

Graph	Final Quarks	Final State	All-Charged Daughters
$I_F, II_F$	$u\bar{c}/u\bar{d}$	$\bar{D}^0\pi^+$	$K^+\pi^-\pi^+$
$I_F, III_D, VII_F$	$c\bar{s}/u\bar{c}$	$D_s^+\bar{D}^0$	$K^+K^-\pi^+K^+\pi^-$
$II_F, VI_F$	$c\bar{c}/u\bar{s}$	$J/\psi K^+$	$e^+e^-K^+$
$III_D, VII_F$	$d\bar{s}/u\bar{d}$	$K^{*0}\pi^+$	$K^+\pi^-\pi^+$
$III_D, VI_F, VII_F$	$s\bar{s}/u\bar{s}$	$\phi K^+$	$K^+K^-K^+$
$I_S, II_S, III_S, VI_F, VII_F$	$u\bar{u}/u\bar{d}$	$\rho^0\pi^+$	$\pi^+\pi^-\pi^+$
$I_D, II_D, III_D, VI_F, VII_F$	$u\bar{u}/u\bar{s}$	$\rho^0K^+$	$\pi^+\pi^-K^+$
$I_S, II_S$	$u\bar{c}/u\bar{s}$	$\bar{D}^0K^+$	$K^+\pi^-K^+$
$I_S, III_S, VII_S$	$c\bar{d}/u\bar{c}$	$D^+\bar{D}^0$	$K^-\pi^+\pi^+K^+\pi^-$
$I_S$	$c\bar{s}/u\bar{u}$	$D_s^+\rho^0$	$K^+K^-\pi^+\pi^+\pi^-$
$II_S, VI_S$	$c\bar{c}/u\bar{d}$	$J/\psi\pi^+$	$e^+e^-\pi^+$
$II_S, III_S$	$c\bar{u}/u\bar{s}$	$D^0K^+$	$K^-\pi^+K^+$
$III_S, VII_S$	$u\bar{s}/s\bar{d}$	$K^+K^{*0}$	$K^+K^+\pi^-$
$III_S$	$c\bar{d}/d\bar{s}$	$D^+K^{*0}$	$K^-\pi^+\pi^+K^+\pi^-$
$III_S$	$c\bar{s}/s\bar{s}$	$D_s^+\phi$	$K^+K^-\pi^+K^+K^-$
$III_S$	$c\bar{c}/c\bar{s}$	$J/\psi D_s^+$	$e^+e^-K^+K^-\pi^+$
$VI_S$	$s\bar{s}/d\bar{u}$	$\phi\pi^+$	$K^+K^-\pi^+$
$I_D, III_D$	$c\bar{d}/u\bar{u}$	$D^+\rho^0$	$K^-\pi^+\pi^+\pi^+\pi^-$
$II_D, III_D$	$c\bar{u}/u\bar{d}$	$D^0\pi^+$	$K^-\pi^+\pi^+$
$III_D$	$c\bar{s}/s\bar{d}$	$D_s^+K^{*0}$	$K^+K^-\pi^+K^+\pi^-$
$III_D$	$c\bar{c}/c\bar{d}$	$J/\psi D^+$	$e^+e^-K^-\pi^+\pi^+$

$J/\psi \rightarrow e^+e^- \dots\dots\dots 0.07$

Tables 2-4 suggest that a study of only the all-charged nonleptonic decay modes of  $B$ -mesons will be very rich, as all basic 4-quark decays of the  $B$ 's can be accessed in this way. Clearly a thorough study will require charged particle identification:  $\pi^\pm$ ,  $K^\pm$ ,  $e^\pm$ , and also  $\mu^\pm$  should all be recognized in the apparatus.

We will use nine of the more interesting basic nonleptonic decay modes to guide our thinking about the design of the apparatus. The ISAJET Monte Carlo program was used to generate samples of the production and decay of  $B$  mesons at the SSC, by numerical calculation of the gluon-gluon production process.

Prominent results of such simulation is that the  $B$ -decay products are spread over  $\pm 7$  units of pseudorapidity  $\eta$  at the SSC, and that the typical transverse momentum of the decay products is less than the  $B$  mass, 5 GeV (see Fig. 4) Now  $\eta = -\ln \tan \theta/2$  where  $\theta$  is the polar angle with respect to the beam direction, so that  $d\eta = d\theta/\theta$ . Hence the population

Table 3: The 28 basic 2-body nonleptonic decays of the  $B_d^0 (= \bar{b}d)$ . The numbers in the 'CP Eigenstate' column refer to the classification described in section 2.4 regarding the relevant CKM phases governing the decay asymmetries.

Graph	Final Quarks	Final State	CP Eigenstate	All-Charged Daughters
$I_F, IV_F$	$d\bar{c}/u\bar{d}$	$D^- \pi^+$		$K^+ \pi^- \pi^- \pi^+$
$I_F, VII_F$	$c\bar{s}/d\bar{c}$	$D_s^+ D^-$		$K^+ K^- \pi^+ K^+ \pi^- \pi^-$
$II_F$	$u\bar{c}/d\bar{d}$	$\bar{D}^0 \rho^0$		$K^+ \pi^- \pi^+ \pi^-$
$II_F, VI_F$	$c\bar{c}/d\bar{s}$	$J/\psi K_S^0$	1	$e^+ e^- \pi^+ \pi^-$
$IV_F$	$u\bar{c}/u\bar{u}$	$\bar{D}^0 \rho^0$		$K^+ \pi^- \pi^+ \pi^-$
$IV_F$	$s\bar{c}/u\bar{s}$	$D_s^- K^+$		$K^+ K^- \pi^- K^+$
$IV_F$	$c\bar{c}/u\bar{c}$	$J/\psi \bar{D}^0$		$e^+ e^- K^+ \pi^-$
$II_D, VI_F, VII_F$	$u\bar{u}/d\bar{s}$	$\rho^0 K_S^0$	2, 1	$\pi^+ \pi^- \pi^+ \pi^-$
$VI_F, VII_F$	$s\bar{s}/d\bar{s}$	$\phi K_S^0$	1	$K^+ K^- \pi^+ \pi^-$
$I_D, VII_F$	$u\bar{s}/d\bar{u}$	$K^+ \pi^-$		$K^+ \pi^-$
$I_S$	$d\bar{c}/u\bar{s}$	$D^- K^+$		$K^+ \pi^- \pi^- K^+$
$I_S, IV_S, V_S, VII_S$	$c\bar{d}/d\bar{c}$	$D^+ D^-$	1, 4	$K^- \pi^+ \pi^+ K^+ \pi^- \pi^-$
$I_S, IV_S, V_S, VII_S$	$u\bar{d}/d\bar{u}$	$\pi^+ \pi^-$	2, 4	$\pi^+ \pi^-$
$I_S$	$c\bar{s}/d\bar{u}$	$D_s^+ \pi^-$		$K^+ K^- \pi^+ \pi^-$
$II_S$	$u\bar{c}/d\bar{s}$	$\bar{D}^0 K^{*0}$		$K^+ \pi^- K^+ \pi^-$
$II_S, VI_S$	$c\bar{c}/d\bar{d}$	$J/\psi \rho^0$	1, 4	$e^+ e^- \pi^+ \pi^-$
$II_S, IV_S, V_S, VI_S, VII_S$	$u\bar{u}/d\bar{d}$	$\rho^0 \rho^0$	2, 4	$\pi^+ \pi^- \pi^+ \pi^-$
$II_S$	$c\bar{u}/d\bar{s}$	$D^0 K^{*0}$		$K^- \pi^+ K^+ \pi^-$
$IV_S, V_S$	$c\bar{u}/u\bar{c}$	$D^0 \bar{D}^0$	1, 4	$K^- \pi^+ K^+ \pi^-$
$IV_S, V_S$	$c\bar{s}/s\bar{c}$	$D_s^+ D_s^-$	1, 4	$K^+ K^- \pi^+ K^+ K^- \pi^-$
$IV_S, V_S$	$u\bar{s}/s\bar{u}$	$K^+ K^-$	2, 4	$K^+ K^-$
$V_S$	$s\bar{s}/s\bar{s}$	$\phi \phi$	4	$K^+ K^- K^+ K^-$
$VI_S$	$s\bar{s}/d\bar{d}$	$\phi \rho^0$	4	$K^+ K^- \pi^+ \pi^-$
$V_S, VII_S$	$s\bar{d}/d\bar{s}$	$K^{*0} \bar{K}^{*0}$	4	$K^+ \pi^- K^- \pi^+$
$I_D, IV_D$	$c\bar{d}/d\bar{u}$	$D^+ \pi^-$		$K^- \pi^+ \pi^+ \pi^-$
$II_D, IV_D$	$c\bar{u}/d\bar{d}$	$D^0 \rho^0$		$K^- \pi^+ \pi^+ \pi^-$
$IV_D$	$c\bar{s}/s\bar{u}$	$D_s^+ K^-$		$K^+ K^- \pi^+ K^-$
$IV_D$	$c\bar{c}/c\bar{u}$	$J/\psi D^0$		$e^+ e^- K^- \pi^+$

of decay products is roughly  $dN/d\theta \sim k/\theta$ , where a value of  $k \sim 6$  is expected at the SSC. The relevant  $\theta_{\min}$  corresponding to  $\eta = 7$  is 2 mrad. Thus a detector for  $B$  physics must emphasize low transverse momentum and forward angles, in contrast to a detector for Higgs physics.

A large range of angle  $\theta$  cannot be covered in a single detector module, and we are led to conceive of an experiment with three angular regions whose approximate boundaries are

Table 4: The 29 basic 2-body nonleptonic decays of the  $B_s^0$  ( $= \bar{b}s$ ).

Graph	Final Quarks	Final State	CP Eigenstate	All-Charged Daughters
$I_F$	$s\bar{c}/u\bar{d}$	$D_s^- \pi^+$		$K^+ K^- \pi^- \pi^+$
$I_F, IV_F, V_F, V_S, VII_F$	$c\bar{s}/s\bar{c}$	$D_s^+ D_s^-$	4	$K^+ K^- \pi^+ K^+ K^- \pi^-$
$II_F$	$u\bar{c}/s\bar{d}$	$\bar{D}^0 K^{*0}$		$K^+ \pi^- K^+ \pi^-$
$II_F, VI_F$	$c\bar{c}/s\bar{s}$	$J/\psi \phi$	4	$e^+ e^- K^+ K^-$
$IV_F, IV_D, V_F, V_S$	$c\bar{u}/u\bar{c}$	$D^0 \bar{D}^0$	4, 3	$K^- \pi^+ K^+ \pi^-$
$IV_F, V_F, V_S$	$c\bar{d}/d\bar{c}$	$D^+ D^-$	4	$K^- \pi^+ \pi^+ K^+ \pi^- \pi^-$
$IV_D, V_F, V_S$	$u\bar{u}/u\bar{u}$	$\rho^0 \rho^0$	3, 4	$\pi^+ \pi^- \pi^+ \pi^-$
$II_D, VI_F$	$s\bar{s}/u\bar{u}$	$\phi \rho^0$	3, 4	$K^+ K^- \pi^+ \pi^-$
$V_F, V_S, VII_F$	$s\bar{s}/s\bar{s}$	$\phi \phi$	4	$K^+ K^- K^+ K^-$
$I_D, IV_D, V_F, V_S, VII_F$	$u\bar{s}/s\bar{u}$	$K^+ K^-$	3, 4	$K^+ K^-$
$V_F, V_S, VII_F$	$d\bar{s}/s\bar{d}$	$K^{*0} \bar{K}^{*0}$	4	$K^+ \pi^- K^- \pi^+$
$IV_D, V_F, V_S$	$u\bar{d}/d\bar{u}$	$\pi^+ \pi^-$	3, 4	$\pi^+ \pi^-$
$I_S$	$s\bar{c}/u\bar{s}$	$D_s^- K^+$		$K^+ K^- \pi^- K^+$
$I_S, VII_S$	$s\bar{c}/c\bar{d}$	$D_s^- D^+$		$K^+ K^- \pi^- K^- \pi^+ \pi^+$
$I_S, VII_S$	$s\bar{u}/u\bar{d}$	$K^- \pi^+$		$K^- \pi^+$
$I_S, IV_S$	$c\bar{s}/s\bar{u}$	$D_s^+ K^-$		$K^+ K^- \pi^+ K^-$
$II_S$	$u\bar{c}/s\bar{s}$	$\bar{D}^0 \phi$		$K^+ \pi^- K^+ K^-$
$II_S, VI_S$	$c\bar{c}/s\bar{d}$	$J/\psi K_S^0$	4, 1	$e^+ e^- \pi^+ \pi^-$
$II_S, VI_S, VII_S$	$u\bar{u}/s\bar{d}$	$\rho^0 K_S^0$	3, 1	$\pi^+ \pi^- \pi^+ \pi^-$
$II_S$	$c\bar{u}/s\bar{s}$	$D^0 \phi$		$K^- \pi^+ K^+ K^-$
$IV_S$	$u\bar{c}/u\bar{u}$	$\bar{D}^0 \rho^0$		$K^+ \pi^- \pi^+ \pi^-$
$IV_S$	$d\bar{c}/u\bar{d}$	$D^- \pi^+$		$K^+ \pi^- \pi^- \pi^+$
$IV_S$	$c\bar{c}/u\bar{c}$	$J/\psi \bar{D}^0$		$e^+ e^- K^+ \pi^-$
$IV_S$	$c\bar{u}/u\bar{u}$	$D^0 \rho^0$		$K^- \pi^+ \pi^+ \pi^-$
$IV_S$	$c\bar{d}/d\bar{u}$	$D^+ \pi^-$		$K^- \pi^+ \pi^+ \pi^-$
$IV_S$	$c\bar{s}/s\bar{u}$	$D_s^+ K^-$		$K^+ K^- \pi^+ K^-$
$VI_S, VII_S$	$s\bar{s}/s\bar{d}$	$\phi K_S^0$	1	$K^+ K^- \pi^+ \pi^-$
$I_D$	$c\bar{d}/s\bar{u}$	$D^+ K^-$		$K^- \pi^+ \pi^+ K^-$
$II_D$	$c\bar{u}/s\bar{d}$	$D^0 K^{*0}$		$K^- \pi^+ K^+ \pi^-$

given by:

1. the Central Region, with  $|\eta| < 1.2$  ( $\theta > 600$  mrad),
2. the Intermediate Region, with  $1.2 < |\eta| < 3.5$  ( $60$  mrad  $< \theta < 600$  mrad),
3. the Forward Region, with  $3.5 < |\eta| < 5.5$  ( $8$  mrad  $< \theta < 60$  mrad).



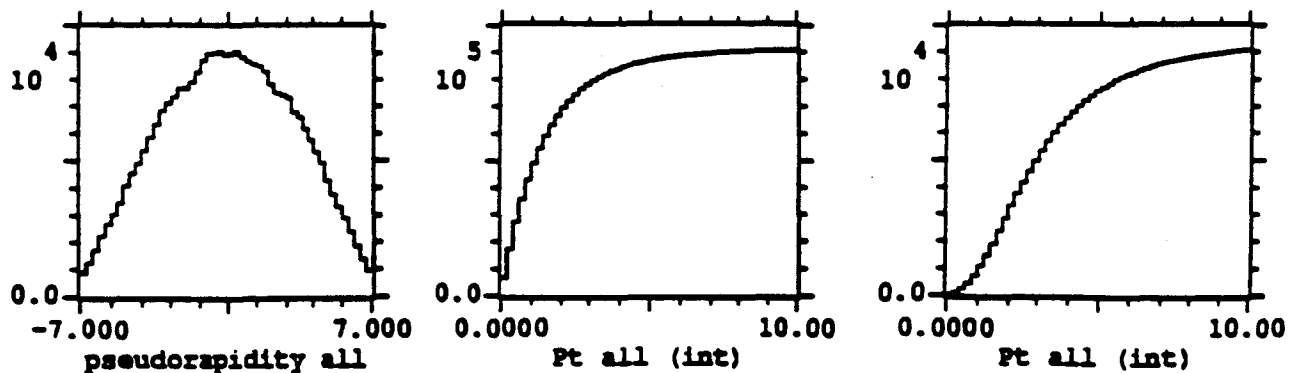


Figure 4: a) Distribution in pseudorapidity  $\eta$ , and b) integral of the  $P_t$  distribution for  $B$ -decay products at the SSC, according to an ISAJET simulation that averages over the ten decay modes in Table 5. c) Integral of the  $P_t$  distribution for the decay  $B_d^0 \rightarrow \pi^+\pi^-$ , which has the stiffest  $P_t$  spectrum of any  $B$  decay. 80% of all  $B$ -decay products have  $P_t < 2.5$  GeV/c, and 80% of the pions from the  $\pi^+\pi^-$  mode have  $P_t < 4.5$  GeV/c

Table 5 lists the geometrical acceptance for various basic nonleptonic decay modes, requiring that all decay products be accepted. Results are presented for each of the three detector regions separately, and in combination. We have applied a few additional cuts, anticipating some details of a realistic detector:

1. in the Central Region, the azimuthal regions within  $\pm 15^\circ$  from the vertical are excluded, anticipating an effective dead region due to use of a transverse dipole analysis magnet.
2. the  $P_t$  of all detected  $\pi^\pm$  and  $K^\pm$  must be greater than 0.3 GeV/c,
3. the  $P_t$  of all detected electrons (or muons) must be greater than 1.0 GeV/c,
4. any  $K_S^0$  must decay before leaving the silicon vertex detector. If this cut is not applied it is likely that the  $K_S$  cannot be associated reliably with the  $B$ -decay vertex.

The eventual goal of the BCD is to study  $CP$  violation in neutral  $B$  decays, which requires tagging of the second  $B$  in the event. Tagging will imply an additional loss of acceptance, especially for detector configurations with only partial coverage. While the precise tagging strategy will evolve over time, we estimate the effect of tagging on acceptance by supposing that the second  $B$  in the event decays according to  $B^0 \rightarrow D^{*-}e^+\nu$ , with  $D^{*-} \rightarrow \bar{D}^0\pi^-$  and  $\bar{D}^0 \rightarrow K^+\pi^-$ , and that we must accept the electron and two of three daughter hadrons for a valid tag. Table 6 presents calculations for the acceptance for this tag, and then Table 7 extends the results of Table 5 to include the requirement of a tag.

We draw our main conclusions as to how the acceptance influences the detector configuration from Table 7:

1. Of the three regions, Central, Intermediate, and Forward, the Intermediate Region is the most important.

Table 5: Geometric acceptance for single  $B$  decays, estimated with an ISAJET simulation. The geometric (and  $P_t$ ) cuts are described in the text. Region C = Central, I = Intermediate, and F = Forward.

Decay Mode	All-Charged Daughters	Detector Region					
		C	I	F	C+I	I+F	C+I+F
$B^+ \rightarrow \bar{D}^0 \pi^+$	$K^+ \pi^- \pi^+$	0.066	0.166	0.089	0.395	0.415	0.649
$B^+ \rightarrow D_s^+ \bar{D}^0$	$K^+ K^- \pi^+ K^+ \pi^-$	0.037	0.115	0.058	0.260	0.291	0.438
$B^+ \rightarrow J/\psi K^+$	$e^+ e^- K^+$	0.049	0.128	0.065	0.271	0.287	0.431
$B_s^0 \rightarrow D^- \pi^+$	$K^+ \pi^- \pi^- \pi^+$	0.043	0.119	0.065	0.269	0.301	0.453
$B_s^0 \rightarrow J/\psi K_S^0$	$e^+ e^- \pi^+ \pi^-$	0.021	0.061	0.011	0.133	0.102	0.174
$B_s^0 \rightarrow \pi^+ \pi^-$	$\pi^+ \pi^-$	0.111	0.233	0.117	0.506	0.496	0.777
$B_s^0 \rightarrow D_s^- \pi^+$	$K^+ K^- \pi^- \pi^+$	0.054	0.152	0.084	0.331	0.363	0.545
$B_s^0 \rightarrow D_s^- \pi^+$	$K^+ K^- \pi^- \pi^+ \pi^- \pi^+$	0.024	0.068	0.034	0.129	0.144	0.204
$B_s^0 \rightarrow D_s^- \pi^+ \pi^+ \pi^-$	$K^+ K^- \pi^- \pi^+ \pi^- \pi^+ \pi^-$	0.009	0.026	0.012	0.052	0.058	0.084
$B_s^0 \rightarrow \bar{D}^0 K^{*0}$	$K^+ \pi^- K^+ \pi^-$	0.042	0.134	0.069	0.296	0.337	0.501
$B_s^0 \rightarrow \rho^0 K_S^0$	$\pi^+ \pi^- \pi^+ \pi^-$	0.033	0.075	0.012	0.178	0.128	0.233
$B_s^0 \rightarrow K^+ K^-$	$K^+ K^-$	0.111	0.233	0.117	0.506	0.496	0.777
Average		0.050	0.126	0.061	0.277	0.285	0.439

Table 6: Geometric acceptance for the tagging decay  $B_s^0 \rightarrow D^{*-} e^+ \nu$ , estimated with an ISAJET simulation. We require the  $e^+$  and only two of three hadrons.

Decay Mode	All-Charged Daughters	Detector Region					
		C	I	F	C+I	I+F	C+I+F
$B_s^0 \rightarrow D^{*-} e^+ \nu$	$K^+ \pi^- \pi^- e^+$	0.058	0.137	0.070	0.273	0.288	0.425

- Adding either a Central or a Forward region to the Intermediate increases the acceptance by a factor of 4. The Central and Forward regions are equally good in augmenting the Intermediate region.
- Adding the third region to the other two doubles the acceptance again.
- Because of the  $P_t$  cuts the acceptance is lower for high-multiplicity decays, and for decays with  $J/\psi \rightarrow e^+ e^-$  or  $\mu^+ \mu^-$ . The soft pion from  $D^*$  decays typically fails the  $P_t$  cut.

In Table 8 we explore the gain in acceptance by extending the Forward region out to  $|\eta| = 7$ , corresponding to angles above 2 mrad from the beams. For tagged  $B$  decays, this

Table 7: Geometric acceptance for tagged  $B$  decays, estimated with an ISAJET simulation. We assume that all decays of the second  $B$  are useful for tagging, but use the decay  $B_d^0 \rightarrow D^{*-} e^+ \nu$  to estimate the correlation in acceptance of the tagging and tagged  $B$ 's.

Decay Mode	All-Charged Daughters	Detector Region					
		C	I	F	C+I	I+F	C+I+F
$B^+ \rightarrow \bar{D}^0 \pi^+$	$K^+ \pi^- \pi^+$	0.009	0.032	0.014	0.147	0.156	0.301
$B^+ \rightarrow D_s^+ \bar{D}^0$	$K^+ K^- \pi^+ K^+ \pi^-$	0.006	0.022	0.010	0.099	0.108	0.209
$B^+ \rightarrow J/\psi K^+$	$e^+ e^- K^+$	0.007	0.025	0.011	0.098	0.110	0.197
$B_d^0 \rightarrow D^- \pi^+$	$K^+ \pi^- \pi^- \pi^+$	0.007	0.022	0.009	0.098	0.113	0.208
$B_d^0 \rightarrow J/\psi K_S^0$	$e^+ e^- \pi^+ \pi^-$	0.003	0.011	0.002	0.052	0.036	0.084
$B_d^0 \rightarrow \pi^+ \pi^-$	$\pi^+ \pi^-$	0.013	0.046	0.020	0.182	0.182	0.350
$B_s^0 \rightarrow D_s^- \pi^+$	$K^+ K^- \pi^- \pi^+$	0.008	0.031	0.014	0.124	0.141	0.256
$B_s^0 \rightarrow D_s^- \pi^+$	$K^+ K^- \pi^- \pi^+ \pi^- \pi^+$	0.004	0.014	0.006	0.050	0.058	0.102
$B_s^0 \rightarrow D_s^- \pi^+ \pi^+ \pi^-$	$K^+ K^- \pi^- \pi^+ \pi^- \pi^+ \pi^+ \pi^-$	0.003	0.005	0.002	0.023	0.023	0.047
$B_s^0 \rightarrow \bar{D}^0 K^{*0}$	$K^+ \pi^- K^+ \pi^-$	0.007	0.025	0.012	0.112	0.122	0.233
$B_s^0 \rightarrow \rho^0 K_S^0$	$\pi^+ \pi^- \pi^+ \pi^-$	0.004	0.014	0.002	0.066	0.046	0.109
$B_s^0 \rightarrow K^+ K^-$	$K^+ K^-$	0.013	0.046	0.020	0.182	0.182	0.350
Average		0.007	0.024	0.010	0.103	0.106	0.204

Table 8: Geometric acceptance for tagged  $B$  decays, with a Forward detector  $F'$  that extends to  $|\eta| = 7$  (2 mrad). Otherwise the results were obtained as in Table 7.

Decay Mode	All-Charged Daughters	Detector Region					
		C	I	F'	C+I	I+F'	C+I+F'
$B^+ \rightarrow \bar{D}^0 \pi^+$	$K^+ \pi^- \pi^+$	0.009	0.032	0.060	0.147	0.228	0.375
$B^+ \rightarrow D_s^+ \bar{D}^0$	$K^+ K^- \pi^+ K^+ \pi^-$	0.006	0.022	0.042	0.099	0.159	0.262
$B^+ \rightarrow J/\psi K^+$	$e^+ e^- K^+$	0.007	0.025	0.040	0.098	0.155	0.243
$B_d^0 \rightarrow D^- \pi^+$	$K^+ \pi^- \pi^- \pi^+$	0.007	0.022	0.043	0.098	0.166	0.264
$B_d^0 \rightarrow J/\psi K_S^0$	$e^+ e^- \pi^+ \pi^-$	0.003	0.011	0.004	0.052	0.041	0.089
$B_d^0 \rightarrow \pi^+ \pi^-$	$\pi^+ \pi^-$	0.013	0.046	0.067	0.182	0.256	0.426
$B_s^0 \rightarrow D_s^- \pi^+$	$K^+ K^- \pi^- \pi^+$	0.008	0.031	0.052	0.124	0.200	0.316
$B_s^0 \rightarrow D_s^- \pi^+$	$K^+ K^- \pi^- \pi^+ \pi^- \pi^+$	0.004	0.014	0.023	0.050	0.081	0.125
$B_s^0 \rightarrow D_s^- \pi^+ \pi^+ \pi^-$	$K^+ K^- \pi^- \pi^+ \pi^- \pi^+ \pi^+ \pi^-$	0.003	0.005	0.023	0.023	0.034	0.058
$B_s^0 \rightarrow \bar{D}^0 K^{*0}$	$K^+ \pi^- K^+ \pi^-$	0.007	0.025	0.050	0.112	0.179	0.292
$B_s^0 \rightarrow \rho^0 K_S^0$	$\pi^+ \pi^- \pi^+ \pi^-$	0.004	0.014	0.004	0.066	0.053	0.117
$B_s^0 \rightarrow K^+ K^-$	$K^+ K^-$	0.013	0.046	0.067	0.182	0.256	0.426
Average		0.007	0.024	0.040	0.103	0.151	0.249

would raise the acceptance in an Intermediate + Forward detector by 50%, and by 25% for a Central + Intermediate + Forward combination.

We now estimate how many  $B$  decays into various modes might be reconstructed in a year of running at the SSC. For this we need three further ingredients. First, we suppose that a  $b\bar{b}$  pair materializes only into mesons, and in the ratios

$$B_u : B_d : B_s = \frac{1-\epsilon}{2} : \frac{1-\epsilon}{2} : \epsilon.$$

We estimate that  $\epsilon = 0.25$ , and hence

$$B_u : B_d : B_s = 0.375 : 0.375 : 0.25.$$

We also need an estimate of the efficiency of the tracking and vertexing of the  $B$  decay, which we take to be 0.33. This is a representative value emerging from simulations described later in this document.

Finally, we need estimates of the branching ratios of the  $B$ 's to the modes of interest, as well as for the secondary decays. The latter branching ratios have been already listed.

A sample rate calculation follows:

- Luminosity .....  $10^{32} \text{ cm}^{-2}\text{sec}^{-1}$
- Standard running year of  $10^7 \text{ sec} \Rightarrow$  .....  $1 \text{ fb}^{-1}$
- $\sigma_{b\bar{b}} = 500 \mu\text{b} \Rightarrow$  .....  $5 \times 10^{11} B\text{-}\bar{B}$  pairs
- $3/4 B^\pm$  per  $B\text{-}\bar{B}$  pair  $\Rightarrow$  .....  $3.75 \times 10^{11} B^\pm$   
 $3/4 B_d^0$  or  $\bar{B}_d^0$  per  $B\text{-}\bar{B}$  pair  $\Rightarrow$  .....  $3.75 \times 10^{11} B_d^0$   
 $1/2 B_s^0$  or  $\bar{B}_s^0$  per  $B\text{-}\bar{B}$  pair  $\Rightarrow$  .....  $2.5 \times 10^{11} B_s^0$
- B.R. for  $B^+ \rightarrow \bar{D}^0 \pi^+$ ;  $\bar{D}^0 \rightarrow K^+ \pi^-$ :  $(0.004)(0.04) = 1.6 \times 10^{-4}$   
 $\Rightarrow$  .....  $6 \times 10^7 B^+ \rightarrow K^+ \pi^- \pi^+$
- Geometric acceptance (column C+I+F of Table 5) = 0.65;  
 Vertexing and tracking efficiency = 0.33;  
 $\Rightarrow$  Overall efficiency = 0.21  $\Rightarrow$  .....  $1.3 \times 10^7$  reconstructed  $B^+ \rightarrow K^+ \pi^- \pi^+$

In this manner we obtain the rate estimates of Table 9, taking branching ratios for  $B$  decay from the model calculations of Bauer, Stech, and Wirbel.<sup>[12]</sup> That paper does not directly predict branching ratios for the  $B_s$ . In the spectator model we expect that  $\text{B.R.}(B_s \rightarrow D_s^- \pi^+) = \text{B.R.}(B_d \rightarrow D^- \pi^+)$ ,  $\text{B.R.}(B_s \rightarrow \rho^0 K_S^0) = \text{B.R.}(B_d \rightarrow \rho^0 \pi^0)$ , and  $\text{B.R.}(B_s \rightarrow K^+ K^-) = \text{B.R.}(B_d \rightarrow K^+ \pi^-) \approx \lambda^2 \text{B.R.}(B_d \rightarrow \pi^+ \pi^-)$ , which leads to the values in Table 9. According to Ref. [12],  $\text{B.R.}(B_s \rightarrow \rho^0 K_S^0)$  will be suppressed by strong-interaction effects and will be comparable to that for  $B_s \rightarrow K^+ K^-$ , although the latter is doubly-CKM-suppressed. For  $B_s \rightarrow K^+ K^-$  we are ignoring the possibility of an important contribution from penguin graphs. This contrasts with sec. 2.3 below where effects of large penguin contributions are considered.

Table 9: Rate estimates for reconstructed  $B$  decays.  $B.R.(B)$  is the branching ratio for the two-body  $B$  decay, estimated according to Bauer *et al.*<sup>[12]</sup>  $B.R.(Tot)$  is the product of  $B.R.(B)$  and the secondary branching ratios. Eff. is the product of the geometric acceptance from column C+I+F of Table 5 and a factor 0.33 for the efficiency of tracking and vertexing. The reconstructed event samples are for an integrated luminosity of  $1 \text{ fb}^{-1}$ , collectable in 1 year of running at a luminosity of  $10^{32} \text{ cm}^{-2}\text{sec}^{-1}$ .

Decay Mode	All-Charged Daughters	B.R.( $B$ )	B.R.(Tot)	Eff.	Recon. Decays
$B^+ \rightarrow \bar{D}^0 \pi^+$	$K^+ \pi^- \pi^+$	0.004	$1.6 \times 10^{-4}$	0.21	$1.3 \times 10^7$
$B^+ \rightarrow D_s^+ \bar{D}^0$	$K^+ K^- \pi^+ K^+ \pi^-$	0.008	$4.8 \times 10^{-6}$	0.14	$2.5 \times 10^6$
$B^+ \rightarrow J/\psi K^+$	$e^+ e^- K^+$	$6 \times 10^{-4}$	$4.2 \times 10^{-5}$	0.14	$2.2 \times 10^6$
$B_d^0 \rightarrow D^- \pi^+$	$K^+ \pi^- \pi^- \pi^+$	0.006	$4.8 \times 10^{-4}$	0.15	$2.7 \times 10^7$
$B_d^0 \rightarrow J/\psi K_S^0$	$e^+ e^- \pi^+ \pi^-$	$3 \times 10^{-4}$	$1.4 \times 10^{-5}$	0.057	$3.0 \times 10^6$
$B_d^0 \rightarrow \pi^+ \pi^-$	$\pi^+ \pi^-$	$2 \times 10^{-5}$	$2 \times 10^{-5}$	0.26	$2.0 \times 10^6$
$B_s^0 \rightarrow D_s^- \pi^+$	$K^+ K^- \pi^- \pi^+$	0.005	$1.5 \times 10^{-4}$	0.18	$6.8 \times 10^6$
$B_s^0 \rightarrow D_s^- \pi^+$	$K^+ K^- \pi^- \pi^+ \pi^- \pi^+$	0.005	$2 \times 10^{-4}$	0.067	$3.3 \times 10^6$
$B_s^0 \rightarrow D_s^- \pi^+ \pi^+ \pi^-$	$K^+ K^- \pi^- \pi^+ \pi^- \pi^+ \pi^+ \pi^-$	0.01	$4 \times 10^{-4}$	0.028	$2.8 \times 10^6$
$B_s^0 \rightarrow \bar{D}^0 K^{*0}$	$K^+ \pi^- K^+ \pi^-$	0.005	$1.3 \times 10^{-4}$	0.17	$5.4 \times 10^6$
$B_s^0 \rightarrow \rho^0 K_S^0$	$\pi^+ \pi^- \pi^+ \pi^-$	$10^{-6}$	$7 \times 10^{-7}$	0.077	$1.3 \times 10^4$
$B_s^0 \rightarrow K^+ K^-$	$K^+ K^-$	$8 \times 10^{-7}$	$8 \times 10^{-7}$	0.26	$5.2 \times 10^4$

If the detector can perform as stated, even doubly-CKM-suppressed decay modes should yield of order 100 reconstructed events per year.

An important first phase of the BCD will be the measurement of the branching ratios of the rarer decays modes that are of interest for studies of  $CP$  violation. Many of these modes, such as those for  $B_s$  decay and for modes with significant penguin contributions, will likely only be studied at a hadron collider.

## 2.2 $B_s$ - $\bar{B}_s$ Mixing

The neutral  $B$ -meson systems  $B_d$ - $\bar{B}_d$  and  $B_s$ - $\bar{B}_s$  each exhibit mixing, characterized by the parameters  $x = \Delta M/\Gamma$ . Theoretically, the mixing arises from a box diagram that is dominated by the top quark, and that is the same for  $B_d$  and  $B_s$ , except for  $d \leftrightarrow s$  interchange.<sup>[13]</sup> Then we can write

$$x_s = x_d \left| \frac{V_{ts}}{V_{td}} \right|^2 \left[ \frac{\tau_s f_s^2 B_s}{\tau_d f_d^2 B_d} \right],$$

where  $\tau$ ,  $f$ , and  $B$  are the lifetime, decay constant and bag constant. The quantity in brackets is near unity, and may eventually be calculable in lattice gauge models. If so,

mixing measurement will provide extra constraints on the CKM matrix elements. For now we suppose this quantity is unity.

We now have

$$x_s \simeq \frac{x_d}{\lambda^2((1-\rho)^2 + \eta^2)} \simeq \frac{14.5}{(1-\rho)^2 + \eta^2},$$

referring to our previous parametrization of the CKM matrix, and noting the experimental results that  $\lambda = 0.22$  and  $x_d \simeq 0.7$ . Present knowledge of parameters  $\rho$  and  $\eta$  then suggests that  $8 < x_s < 20$  for  $100 < M_t < 150 \text{ GeV}/c^2$ .

At a hadron collider the measurement of  $B_s$  mixing previews many of the challenges of  $CP$  violation in neutral  $B$ 's. This is because we must know the particle/antiparticle character of the  $B$  when it is produced to complete the analysis. To study mixing, we must also know the particle/antiparticle character of the  $B$  when it decays. Hence the observed decay mode must not be self-conjugate. We will use the modes  $B_s \rightarrow D_s^- \pi^+$  and  $\bar{D}^0 K^{*0}$  as examples.

If we start with  $N$   $B_s$  mesons at  $t = 0$ , at time  $t$  we have

$$N_{B(B)} = (N/2)e^{-t}(1 \pm \cos xt),$$

where in this section we measure the proper time  $t$  in units of the  $B$  lifetime (assumed equal for the two mass eigenstates). We actually start with an equal number of  $B$  and  $\bar{B}$  mesons at  $t = 0$ , and so collect four decay distributions, labelled by the particle/antiparticle character at creation and decay. By taking the appropriate sum and difference of these four distributions we can isolate the distribution

$$D(t) = Ne^{-t} \cos xt,$$

while the number of  $B$ 's left at time  $t$  is, of course,  $Ne^{-t}$ .

The value of  $x$  can be determined if the oscillations of  $D(t)$  are well resolved. First we consider the statistical power required to determine  $x$ , supposing that the time resolution is perfect. A simple criterion is that the size of the oscillations must be clearly non-zero; we require that the first few quarter cycles each to have 25 events to maintain a 5- $\sigma$  distinction. In, say, the 8th quarter cycle there are  $\sim (N\pi/2x)e^{-4\pi/x}$  events, so we need  $N \gtrsim 50xe^{4\pi/x}/\pi$ . Then about 600 events would be needed to measure the oscillations for any  $x$  from 8 to 25.

However, if the time resolution deteriorates to a quarter cycle, the oscillation will become unrecognizable. Thus we desire an resolution  $\sigma_s < \pi/2x$ , and hence  $\sigma_s < 1/16$  to resolve  $x$  up to 25. The achieved value of  $\sigma_s$  depends on the quality of the vertex detector. To a good approximation  $\sigma_s = \sigma_z/c\tau$  where  $\sigma_z$  is the spatial resolution of the vertex detector, and  $\tau$  is the  $B$  lifetime. Since  $c\tau = 360 \mu\text{m}$  for  $B$ 's, and  $\sigma_z \sim 20 \mu\text{m}$  is typically obtained with silicon vertex detectors, we expect that mixing parameters of  $x \lesssim 25$  should indeed be resolvable. Extreme care in the construction of the vertex detector will be required to resolve larger values of  $x_s$ .

Thus 600  $B_s$  decays will be sufficient to measure  $x_s$  over its presently expected range, provided each decay is tagged as to whether the  $B$  started as a particle or antiparticle. For the tag we must look at the other  $B$  in the event. If we are to maintain a reasonable tagging efficiency, we must identify decays of the other  $B$  that contain neutrals. To have confidence that we are associating tracks with a  $B$  decay and not the primary hadronic interaction, the

tracks of the second  $B$  must come from a secondary vertex. Neutral tracks are not useful for this. Hence we will have only a partial reconstruction of the second  $B$  in general. Without a mass constraint we cannot be sure that all charged tracks from the second  $B$  have been found, and so we will not be able, in general, to tell whether the second  $B$  was a  $B_u$ ,  $B_d$ , or  $B_s$ .

If the second  $B$  is neutral, it may have oscillated before we detect it. Thus the tag cannot be perfect. Indeed, a neutral  $B$  with mixing parameter  $x$  decays in the opposite particle/antiparticle state to that in which it was created with probability  $x^2/2(1+x^2)$ . For a  $B_d$  with  $x_d = 0.7$  the probability of a mistag is  $1/6$ , but for a  $B_s$  with  $x_s > 8$  it is essentially  $1/2$ . The  $B_s$  oscillates so rapidly that it is useless as a tag.

If a fraction  $p$  of our events are mistagged, the distribution  $D(t)$  describing the oscillation becomes  $(1-2p)Ne^{-t} \cos xt$ , and the error on  $x$  extracted from analysis of  $D$  grows by a factor  $1/(1-2p)$ . It will now require  $1/(1-2p)^2$  as many events to achieve a given statistical significance. This dilution of the tag is largely unavoidable at a hadron collider.

We estimate the dilution factor by recalling our hypothesis as to the relative product of the various  $B$ 's, assumed uncorrelated with the type of the other  $B$ ,

$$B_u : B_d : B_s = \frac{1-\epsilon}{2} : \frac{1-\epsilon}{2} : \epsilon.$$

We can then write

$$1-2p = \frac{1-\epsilon}{2} + \frac{1-\epsilon}{2} \frac{1}{1+x_d^2} + \epsilon \frac{1}{1+x_s^2} \approx 0.6,$$

using  $\epsilon = 0.25$ ,  $x_d = 0.7$ , and  $x_s > 8$ . Our earlier requirement of 600 perfectly tagged  $B_s$  decays now becomes 1500 decays with a diluted tag.

The question remains as to the mechanism of the tag. The most straightforward tag is on the sign of the leading lepton in a semileptonic  $B$  decay. Even if both electrons and muons are identified, only about 20% of all  $B$ 's could be tagged. In Table 6 (based on calculations similar to those for Table 5) we estimated that the geometric acceptance for a semileptonic decay would be about 40%, taking into account  $P_t$  cuts. Also, only about 30% of the semileptonic decays would be clearly identified as belonging to a secondary vertex. Hence the overall efficiency of a semileptonic tag would be about 3%. Then instead of needing 1500 reconstructed  $B_s$  decays for the oscillation analysis, we will need about 56,000.

In Table 9 we estimated the yield of reconstructed  $B_s$  decays to be  $2 \times 10^7$  in 4 modes useful for an oscillation study. Other modes can be added as well, raising the yield to at least  $5 \times 10^7$ , or 1000 times that needed to demonstrate the oscillation signal. Equivalently, even if the SSC ran at a luminosity of only  $10^{29} \text{ cm}^{-2}\text{sec}^{-1}$ , the BCD could detect  $B_s$  mixing.

### 2.3 $CP$ Violation in Self-Tagging $B$ Decays

The study of  $CP$  violation in the decays of neutral  $B$ 's to  $CP$  eigenstates will also require us to confront the complexities of tagging. First we consider the prospects for demonstration of  $CP$  violation in the  $B$ -meson system without the need for tagging.

Recall that the proposed method to study  $CP$  violation is measurement of the asymmetry

$$A = \frac{\Gamma(B \rightarrow f) - \Gamma(\bar{B} \rightarrow \bar{f})}{\Gamma(B \rightarrow f) + \Gamma(\bar{B} \rightarrow \bar{f})}.$$

In this measurement we need only know the particle/antiparticle character of the  $B$  at the time of its decay. So if final state  $f$  is distinct from  $\bar{f}$  then no tagging is needed. Decays such as  $B^+ \rightarrow \bar{D}^0 \pi^+$ ,  $B_d^0 \rightarrow D^- \pi^+$ , and  $B_s^0 \rightarrow D_s^- \pi^+$  are all of this type, which is often called self-tagging.

For a decay rate  $\Gamma$  to be different from its  $CP$ -conjugate rate  $\bar{\Gamma}$ , the decay process must involve the interference of two amplitudes. Labelling these  $a_1$  and  $a_2$  and supposing  $a_1$  to be real, we can write

$$\Gamma = |a_1 + a_2 e^{i\delta_{wk}} e^{i\delta_{st}}|^2.$$

For the  $CP$ -conjugate decay, the weak-interaction phase changes sign while the strong-interaction phase does not (due to  $CP$  invariance of the strong interaction). Hence

$$\bar{\Gamma} = |a_1 + a_2 e^{-i\delta_{wk}} e^{i\delta_{st}}|^2.$$

To have  $\Gamma \neq \bar{\Gamma}$ , not only must two amplitudes interfere, but also both the weak and strong phases must differ between the two amplitudes. For a large effect, the two amplitudes should be of comparable magnitude.

As such, the more prominent two-body nonleptonic  $B$  decays to self-tagging final states are likely to have very small  $CP$  asymmetries. Referring to Tables 2-4, we see that the decays with a high rate are due to the (tree-level) spectator graphs. Even when both spectator graphs contribute, their CKM structure is the same. The speculation is that the largest asymmetries in self-tagging modes will occur when penguin graphs interfere with suppressed spectator graphs.<sup>[14, 15, 16]</sup> Table 10 summarizes the events rates expected in BCD for three self-tagging modes whose  $CP$  asymmetries may be in the range 10-40% in the optimistic view of Ref. [15], although a more typical prediction<sup>[16]</sup> is for asymmetries of 1-3%. Even the size of the penguin contribution to the branching ratios is somewhat controversial, and the values given below are considerably larger than those calculated in the model of Bauer, Stech, and Wirbel.<sup>[17]</sup>

If we collect  $N$  events in a self-tagging mode with  $CP$  asymmetry  $A$ , then the statistical significance of our measurement of  $A$  is

$$S = \frac{A}{\sigma_A} = \sqrt{N} \frac{A}{\sqrt{1 - A^2}}.$$

The minimum value of  $A$  that could be resolved to  $S$  standard deviations is

$$A_{\min, S\sigma} = \frac{S}{\sqrt{N + S^2}}.$$

Thus with  $10^6$  events we could resolve an asymmetry as small as  $A = 0.005$  to  $5\sigma$ .

Ref. [16] argues that decays with penguin contributions involving  $b \rightarrow d$  such as  $B^+ \rightarrow K^+ K^0$  should have an asymmetry of 10-15%, but the branching ratios will be more like  $10^{-6}$ . The BCD should be sensitive to asymmetries of about 2% or greater in such modes.

Should the branching ratios and  $CP$  asymmetries in self-tagging modes be as large as the most optimistic predictions they will likely provide the first evidence for  $CP$  violation in the  $B$  system. For the typical predicted asymmetry, the signal in self-tagging modes is only comparable to that in decays to  $CP$  eigenstates, discussed in the next section. The



Table 10: Rate estimates for self-tagging  $B$  decays. B.R.( $B$ ) is the branching ratio for the two-body  $B$  decay, estimated according to Chau.<sup>[16]</sup> B.R.(Tot) is the product of B.R.( $B$ ) and the secondary branching ratios. Eff. is the product of the geometric acceptance in a detector configuration C+I+F as in Table 5 and a factor 0.33 for the efficiency of tracking and vertexing. The reconstructed event samples are for an integrated luminosity of  $1 \text{ fb}^{-1}$ , collectable in 1 year of running at a luminosity of  $10^{32} \text{ cm}^{-2}\text{sec}^{-1}$ .

Decay Mode	All-Charged Daughters	B.R.( $B$ )	B.R.(Tot)	Eff.	Recon. Decays
$B^+ \rightarrow \rho^0 K^+$	$\pi^+\pi^-K^+$	$10^{-5}$	$10^{-5}$	0.20	$7.3 \times 10^6$
$B_s^0 \rightarrow K^{*+}\pi^-$	$\pi^+\pi^-\pi^+\pi^-$	$10^{-4}$	$2.2 \times 10^{-5}$	0.08	$6.7 \times 10^6$
$B_s^0 \rightarrow K^{*+}K^-$	$\pi^+\pi^-\pi^+K^-$	$2 \times 10^{-4}$	$6.7 \times 10^{-5}$	0.08	$1.3 \times 10^6$

theoretical interpretation in terms of CKM-matrix parameters of an observed asymmetry in a self-tagging decay may be unclear, due to uncertainties in the calculation of the penguin graphs.

## 2.4 $CP$ Violation in Decays of Neutral $B$ 's to $CP$ Eigenstates

The most detailed knowledge to be gained from the BCD is in the study of  $CP$  violation in the decays of neutral  $B$ 's to  $CP$  eigenstates. This topic is interesting in part because of its intricacy. We first present a review of the context of  $CP$  violation in the  $B$ -meson system in some detail.<sup>[18]</sup>

### 2.4.1 A $CP$ Primer

Perhaps the best way to understand  $CP$  violation in the  $B$  system is by comparison with the  $K$  system. In the  $K$  system, the states  $|K^0\rangle$  and  $|\bar{K}^0\rangle$  are eigenstates of the strong and electromagnetic interactions, which conserve strangeness. However, these states are not eigenstates of the weak interactions, which violate strangeness, and which are responsible for Kaon decay. Taking into account the weak interactions, one writes the  $2 \times 2$  Hamiltonian (in the  $K^0$ - $\bar{K}^0$  basis)

$$H = M - \frac{i}{2}\Gamma, \quad (1)$$

where the mass matrix  $M$  and the decay matrix  $\Gamma$  are Hermitian. (Since neutral Kaons do decay,  $H$  itself is not Hermitian.)  $CPT$  invariance implies that the diagonal components of  $H$  are equal, and if  $CP$  is conserved  $M$  and  $\Gamma$  are real. Allowing for the possibility of  $CP$  violation, diagonalizing the Hamiltonian

$$H = \begin{bmatrix} m & M_{12} \\ M_{12}^* & m \end{bmatrix} - \frac{i}{2} \begin{bmatrix} \gamma & \Gamma_{12} \\ \Gamma_{12}^* & \gamma \end{bmatrix} \quad (2)$$

yields the eigenstates

$$\begin{aligned} |K_S^0\rangle &= \frac{1}{\sqrt{2(1+|\epsilon|^2)}} \left[ (1+\epsilon)|K^0\rangle - (1-\epsilon)|\bar{K}^0\rangle \right], \\ |K_L^0\rangle &= \frac{1}{\sqrt{2(1+|\epsilon|^2)}} \left[ (1+\epsilon)|K^0\rangle + (1-\epsilon)|\bar{K}^0\rangle \right], \end{aligned} \quad (3)$$

where

$$\frac{1-\epsilon}{1+\epsilon} = \sqrt{\frac{M_{12}^* - \frac{i}{2}\Gamma_{12}^*}{M_{12} - \frac{i}{2}\Gamma_{12}}}. \quad (4)$$

If  $M$  and  $\Gamma$  were real, then  $\epsilon$  would be zero, so that a nonzero  $\epsilon$  is evidence for  $\Delta S = 2$   $CP$  violation. (In the limit of vanishing  $\epsilon$ , the weak states would be  $CP$  eigenstates:  $K_S$  would have  $CP +$ ;  $K_L$  would have  $CP -$ .) This will be referred to as  $CP$  violation in the mixing. The mass and width differences between the states  $|K_L^0\rangle$  and  $|K_S^0\rangle$  are given by

$$\begin{aligned} \Delta M &= 2 \operatorname{Re} \left[ \left( M_{12} - \frac{i}{2}\Gamma_{12} \right) \left( M_{12}^* - \frac{i}{2}\Gamma_{12}^* \right) \right]^{1/2}, \\ \Delta \Gamma &= -4 \operatorname{Im} \left[ \left( M_{12} - \frac{i}{2}\Gamma_{12} \right) \left( M_{12}^* - \frac{i}{2}\Gamma_{12}^* \right) \right]^{1/2}. \end{aligned} \quad (5)$$

It is also possible to have  $CP$  violation in the decays of Kaons, parametrized by the  $\Delta S = 1$   $CP$ -violating parameter  $\epsilon'$ , which arises from different isospin phases in the amplitudes for the decays  $K \rightarrow 2\pi$ :

$$\begin{aligned} a_0 &= \langle \pi\pi, I=0 | H_W | K^0 \rangle, \\ a_2 &= \langle \pi\pi, I=2 | H_W | K^0 \rangle, \end{aligned} \quad (6)$$

and

$$\epsilon' \propto \operatorname{Im} \left( \frac{a_2}{a_0} \right). \quad (7)$$

In the standard model, it is expected that  $\epsilon' \ll \epsilon$ , and experimentally one finds that

$$\frac{\epsilon'}{\epsilon} \lesssim O(10^{-3}). \quad (8)$$

Therefore, in the Kaon system,  $CP$  violation with  $\Delta S = 2$  is much larger than that with  $\Delta S = 1$ .

For  $B$  mesons, the mixing formalism is identical to that given in Eqs. 1-5. However, there are some significant differences between the  $B$  system and the  $K$  system. First of all, since  $B$  mesons are so heavy, the phase space for their decays is quite large. Therefore both  $B$  and  $\bar{B}$  have essentially the same lifetime, so that  $\Delta\Gamma/\Gamma \ll 1$ . Furthermore, calculations based on the box diagram in the standard model have shown that, for the  $B$  system,  $\Gamma_{12} \ll M_{12}$ , which leads to the result that  $\Delta\Gamma \ll \Delta M$ . (We note that this is quite different than the  $K$  system, where there is a substantial lifetime difference, due to the difference between the  $2\pi$  and  $3\pi$  channels.) We will therefore neglect  $\Delta\Gamma$  in what follows.

For the same reason, the  $\Delta B = 2$   $CP$ -violating parameter in the  $B$  system,  $\epsilon_B$ , is also small:

$$\left| \frac{1+\epsilon_B}{1-\epsilon_B} \right| \simeq 1 + \operatorname{Im} \frac{\Gamma_{12}}{M_{12}}. \quad (9)$$

Using the box diagram,  $\epsilon_B$  has been calculated in the Standard Model:

$$\epsilon_B = \begin{cases} O(10^{-4}), & B_d, \\ O(10^{-6}), & B_s. \end{cases} \quad (10)$$

It therefore seems that the prospects for observation of  $\Delta B = 2$   $CP$ -violating phenomena are essentially hopeless.

However, in the  $B$  system, the situation is reversed with respect to the Kaon system, namely,  $CP$  violation in  $B$  decays ( $\Delta B = 1$ ) can be large. In order to observe  $CP$  violation, one needs interference between two amplitudes with different phases. The most interesting processes are those involving a final state  $f$  to which both the  $B^0$  and  $\bar{B}^0$  can decay. Then the needed interference will arise because of  $B^0$ - $\bar{B}^0$  mixing.<sup>1</sup> Even more interesting is the case when  $f$  is a  $CP$  eigenstate, and also when only a single weak amplitude (and its  $CP$ -conjugate) are involved, so that certain strong-interaction complications cancel, as noted later.

First, for  $B$ - $\bar{B}$  mixing the relevant parameter is  $x_q$ , the ratio of the energy of the oscillation (i.e., the mass difference) and the total width for the  $B_q$  mesons ( $q = d, s$ ):

$$x_q = \frac{\Delta M}{\Gamma} \frac{(\text{transition energy})}{(\text{mean total width})}. \quad (11)$$

After all, mixing hardly matters if the particle decays before it has a chance to oscillate into its antiparticle.

This can be seen explicitly by considering the time evolution of  $B$  mesons. Because of  $B^0$ - $\bar{B}^0$  mixing, a state which starts out as a pure  $B^0$  or  $\bar{B}^0$  will evolve in time to a mixture of  $B^0$  and  $\bar{B}^0$ :

$$\begin{aligned} |B^0(t)\rangle &= f_+(t)|B^0\rangle + \frac{q}{p}f_-(t)|\bar{B}^0\rangle, \\ |\bar{B}^0(t)\rangle &= \frac{q}{p}f_-(t)|B^0\rangle + f_+(t)|\bar{B}^0\rangle. \end{aligned} \quad (12)$$

Here,  $|B^0\rangle$  represents a pure  $B^0$  state at  $t = 0$ ,  $|\bar{B}^0\rangle$  represents a pure  $\bar{B}^0$  state at  $t = 0$ ,

$$\frac{q}{p} = \frac{1 - \epsilon_B}{1 + \epsilon_B}, \quad (13)$$

and

$$\begin{aligned} f_+(t) &= e^{-iMt}e^{-\Gamma t/2} \cos(\Delta Mt/2), \\ f_-(t) &= ie^{-iMt}e^{-\Gamma t/2} \sin(\Delta Mt/2). \end{aligned} \quad (14)$$

From Eq. 14, it is clearly seen that the competition between  $\Delta M$  and  $\Gamma$  is the important consideration for seeing  $CP$  violation in  $B$  decays.

$CP$  violation is manifested in a nonzero value of the asymmetry

$$A_f(t) = \frac{\Gamma(B^0(t) \rightarrow f) - \Gamma(\bar{B}^0(t) \rightarrow \bar{f})}{\Gamma(B^0(t) \rightarrow f) + \Gamma(\bar{B}^0(t) \rightarrow \bar{f})}. \quad (15)$$

<sup>1</sup>There are also decays in which the  $CP$  violation is due to final state interactions as discussed in the previous subsection, but these are less useful theoretically, since knowledge of hadronic matrix elements is needed to extract information about the CKM matrix.

If we consider a nonleptonic final state  $f$  such that both  $B^0$  and  $\bar{B}^0$  can decay both to it (and to its  $CP$ -conjugate state  $\bar{f}$ ), this asymmetry can be calculated from Eqs. 12 and 14. We have

$$\begin{aligned} \Gamma(\bar{B}^0(t) \rightarrow f) &= \left| \langle f | \bar{B}^0(t) \rangle \right|^2 \\ &= \left| \langle f | \bar{B}^0 \rangle \right|^2 e^{-t/\tau} \left[ \cos^2 \frac{\Delta M t}{2} + \left| \bar{\alpha}_f \right|^2 \sin^2 \frac{\Delta M t}{2} - \text{Im } \bar{\alpha}_f \sin \Delta M t \right] \end{aligned} \quad (16)$$

where we have introduced

$$\alpha_f = \frac{q}{p} \rho_f, \quad \bar{\alpha}_f = \frac{p}{q} \bar{\rho}_f, \quad (17)$$

and

$$\rho_f = \frac{\langle f | \bar{B}^0 \rangle}{\langle f | B^0 \rangle}, \quad \bar{\rho}_f = \frac{\langle \bar{f} | B^0 \rangle}{\langle \bar{f} | \bar{B}^0 \rangle}. \quad (18)$$

There are several points worth noting here. First of all,  $q/p$  is a pure phase. This can be seen from Eqs. 4 and 13, for  $\Gamma_{12} \ll M_{12}$ :

$$\frac{q}{p} = \sqrt{\frac{M_{12}^*}{M_{12}}}. \quad (19)$$

Secondly, when only one amplitude contributes to  $B^0 \rightarrow f$  (and its  $CP$ -conjugate to  $\bar{B}^0 \rightarrow \bar{f}$ ) then (recall the argument of the previous subsection about the converse)

$$\left| \langle f | B^0 \rangle \right| = \left| \langle \bar{f} | \bar{B}^0 \rangle \right|, \quad \left| \langle \bar{f} | B^0 \rangle \right| = \left| \langle f | \bar{B}^0 \rangle \right|, \quad (20)$$

i.e.,  $|\rho_f| = |\bar{\rho}_f|$ . If there were no mixing there would now be no  $CP$  violation. However, in the presence of mixing case Eq. 15 becomes

$$A_f(t) = \frac{-(\text{Im } \alpha - \text{Im } \bar{\alpha}) \sin \Delta M t}{2 \cos^2(\Delta M t/2) + 2 |\rho_f|^2 \sin^2(\Delta M t/2) - (\text{Im } \alpha + \text{Im } \bar{\alpha}) \sin \Delta M t} \quad (21)$$

There may still be complications, however, due to  $\rho_f$  (and  $\bar{\rho}_f$ ). To see this, it is helpful to introduce the Cabibbo-Kobayashi-Maskawa (CKM) matrix here. A convenient parametrization of the CKM matrix (slightly different from that used earlier) is<sup>[19]</sup>

$$V_{CKM} = \begin{pmatrix} V_{ud} & V_{us} & V_{ub} \\ V_{cd} & V_{cs} & V_{cb} \\ V_{td} & V_{ts} & V_{tb} \end{pmatrix} \approx \begin{pmatrix} 1 - \frac{\lambda^2}{2} & \lambda & A\lambda^3 \rho e^{-i\phi} \\ -\lambda & 1 - \frac{\lambda^2}{2} & A\lambda^2 \\ A\lambda^3(1 - \rho e^{i\phi}) & -A\lambda^2 & 1 \end{pmatrix}. \quad (22)$$

In this parametrization the CKM matrix elements are expanded in powers of  $\lambda$ , the Cabibbo angle ( $\lambda = 0.22$ ).<sup>2</sup> This is particularly convenient because one can estimate the size of certain  $B$ -decay diagrams just by counting powers of  $\lambda$ . For example, consider the final state  $D^+ \pi^-$ . Here,

$$\begin{aligned} \langle D^+ \pi^- | B^0 \rangle &\sim V_{ub}^* V_{cd} \sim \mathcal{O}(\lambda^4), \\ \langle D^+ \pi^- | \bar{B}^0 \rangle &\sim V_{cb} V_{ud}^* \sim \mathcal{O}(\lambda^2). \end{aligned} \quad (23)$$

<sup>2</sup>Note that, in  $V_{CKM}$ , other terms have phases as well, but they are of higher order in  $\lambda$ . Large phases appear only in  $V_{ub}$  and  $V_{td}$ .

Therefore  $\rho_f \sim \lambda^{-2} \sim 20$ . According to Eq. 15 the asymmetry goes like  $1/\rho_f$  for large  $\rho_f$ , so it will be quite small for most values of  $t$ . If we had considered the final state  $D^-\pi^+$ , then we would have  $\rho_f \sim \lambda^2 \sim 0.05$ , and the asymmetry would again be small since  $\text{Im } \alpha_f$  is proportional to  $\rho_f$ . Furthermore, for both of these final states, hadronization effects are important. For example, for the final state  $D^+\pi^-$  from  $B^0$  decay the  $W$  hadronizes into the  $D$ , while from  $\bar{B}^0$  decay it hadronizes into the  $\pi$ . There is no reliable way to calculate these effects.

These problems can be avoided by considering final states which are  $CP$  eigenstates ( $f = \pm \bar{f}$ ). Because of mixing, interference will occur between  $\langle f|B^0\rangle$  and  $\langle f|\bar{B}^0\rangle$ , but now the latter is equal to  $\pm\langle \bar{f}|\bar{B}^0\rangle$ , which is equal in magnitude to  $\langle f|B^0\rangle$  according to Eq. 20. Hence the amplitude ratio  $\rho_f$  will also be a pure phase (i.e.,  $|\rho_f| = 1$ ).

For example, in the decay  $B^0 \rightarrow \pi^+\pi^-$  we have

$$\begin{aligned} \langle \pi^+\pi^-|B^0\rangle &\sim V_{ub}^*V_{ud} = A\rho\lambda^3e^{i\delta}, \\ \langle \pi^+\pi^-|\bar{B}^0\rangle &\sim V_{ub}V_{ud}^* = A\rho\lambda^3e^{-i\delta}. \end{aligned} \quad (24)$$

In addition, any hadronization phases must cancel in  $\rho_f$ , since the two diagrams are  $CP$  conjugates of one another, and the strong interactions are  $CP$  invariant. We therefore obtain  $\rho_f = \exp(-2i\delta)$ . And, from  $|\rho_f| = 1$  we get

$$\text{Im } \bar{\alpha}_f = -\text{Im } \alpha_f. \quad (25)$$

Eq. 25 holds for any decay to a  $CP$  eigenstate that is described by a single weak amplitude. Thus, for this class of final states we have (using Eqs. 11 and 16)

$$\Gamma(\bar{B}_q^0(t) \rightarrow \bar{f}) = |\langle f|B_q^0\rangle|^2 e^{-t/\tau} [1 \mp \text{Im } \alpha_f \sin x_q \frac{t}{\tau}] \quad (26)$$

Now Eq. 15 assumes the elegantly simple form

$$A_f(t) = -\text{Im } \alpha_f \sin x_q \frac{t}{\tau}. \quad (27)$$

For decays to  $CP$  eigenstates, the  $CP$ -violating parameter  $\alpha_f$  is therefore a pure phase, and keeps track of all phase information in the process. This is related to the parameters of the CKM matrix as follows. The expression for  $\alpha_f$  is (Eq. 17, repeated here for clarity)

$$\alpha_f = \frac{q}{p} \rho_f.$$

There are therefore two sources of phase information - in the mixing ( $q/p$ ), and in the decay ( $\rho_f$ ). As discussed earlier, to a good approximation,  $q/p$  is a pure phase (Eq. 19). Now,  $M_{12}$  is calculable from the Standard Model box diagram for  $B_q^0$ - $\bar{B}_q^0$  mixing ( $q = d, s$ ), which is dominated by  $t$ -quark exchange:

$$M_{12} \sim f(M_t) (V_{tb}V_{tq}^*)^2, \quad (28)$$

and therefore the phase information from the mixing is

$$\frac{q}{p} = \begin{cases} (V_{tb}^*/V_{tb})(V_{td}/V_{td}^*) = (V_{td}/V_{td}^*) \equiv e^{-2i\phi}, & (B_d), \\ (V_{tb}^*/V_{tb})(V_{ts}/V_{ts}^*) \simeq 1, & (B_s). \end{cases} \quad (29)$$

In Eq. 29,  $\phi$  is the phase of  $V_{td}$ . The phase information in the decay depends on whether the  $b$ -quark decays into a  $c$ - or a  $u$ -quark:

$$\rho_f = \begin{cases} (V_{ub}/V_{ub}^*) \equiv e^{-2i\delta}, & b \rightarrow u, \\ (V_{cb}/V_{cb}^*) = 1, & b \rightarrow c. \end{cases} \quad (30)$$

As before,  $\delta$  is the phase of  $V_{ub}$ . Thus it can be immediately seen that there are four classes of decays measuring different combinations of phases in the CKM matrix:

$$\begin{aligned} \text{Class 1. } & B_d \text{ decays with } b \rightarrow c \text{ (e.g. } B_d \rightarrow J/\psi K_S \text{)}: \quad \text{Im } \alpha_1 = -\sin 2\phi, \\ \text{Class 2. } & B_d \text{ decays with } b \rightarrow u \text{ (e.g. } B_d \rightarrow \pi^+ \pi^- \text{)}: \quad \text{Im } \alpha_2 = -\sin 2(\delta + \phi), \\ \text{Class 3. } & B_s \text{ decays with } b \rightarrow u \text{ (e.g. } B_s \rightarrow \rho K_S \text{)}: \quad \text{Im } \alpha_3 = -\sin 2\delta, \\ \text{Class 4. } & B_s \text{ decays with } b \rightarrow c \text{ (e.g. } B_s \rightarrow J/\psi \phi \text{)}: \quad \text{Im } \alpha_4 \simeq 0. \end{aligned} \quad (31)$$

The  $CP$  violation in class-1 decays originates in the mass matrix, that of class-3 decays is from the decay amplitude, while that of class-2 decays is due to both effects. In addition to measuring the decay asymmetries in classes 1-3, it will be an important test of the Standard Model to search for  $CP$  violation in class-4 decays. A nonzero measurement of a  $CP$  asymmetry in this class would be a clear signal of physics beyond the Standard Model.

We summarize the main arguments of this section, with an attempt to trace their historical development:

1.  $CP$  violation in the  $B$  system is not primarily due to the magnitude of  $CP$  violation in the mass eigenstates,  $\epsilon_B \ll \epsilon_K$ . However, the relative amplitudes of  $|B^0\rangle$  and  $|\bar{B}^0\rangle$  in the mass eigenstates is given by a pure phase (since  $\Gamma_{12} \ll M_{12}$  in Eqs. 4 and 13). The phase is that of  $V_{td}$ , due to the dominance of the top-quark in the box diagram that governs  $B^0$ - $\bar{B}^0$  mixing.<sup>[20]</sup>
2.  $CP$  violation can be due to interference of two decay amplitudes with different weak phases. When comparing rates for  $B^0 \rightarrow f$  and  $\bar{B}^0 \rightarrow f$ , the phase in the mass eigenstates can enter due to  $B^0$ - $\bar{B}^0$  mixing.<sup>[21]</sup>
3. If the final state  $f$  is a  $CP$  eigenstate then strong-interaction effects cancel, and the  $CP$  violation can be entirely due to the phase in the mass eigenstates.<sup>[22]</sup> Hence a direct measurement of the phase of a CKM-matrix element is possible.
4. There can be a large weak phase in the decay amplitudes also, that of  $V_{ub}$ . (This phase can only enter in higher order in  $K$  decays.) As a consequence there are four classes of neutral- $B$  decays to  $CP$  eigenstates, yielding three different measures of phases in the CKM matrix.<sup>[18]</sup>

The interpretation of experimental asymmetries in terms of phases of CKM-matrix elements is dependent on the phase convention adopted. The Miani-Wolfenstein representation of the CKM matrix is convenient in that here  $V_{tb}$  has, in general, a nonzero phase, which serves to emphasize the importance of mixing in  $CP$ -violation studies.

The CKM phases that govern the three classes of nonzero asymmetries are often demonstrated using the unitarity triangle,<sup>[23]</sup> shown earlier in Fig. 2. The unitarity of  $V_{CKM}$  implies

$$V_{td} + \lambda V_{ts} + V_{tb}^* \approx 0. \quad (32)$$

Hence, if these three complex matrix elements are regarded as vectors, they form a closed triangle. The goal is then to measure the three interior angles  $\varphi_1, \varphi_2, \varphi_3$ , and to see if the triangle closes, i.e., to see if the angles add up to  $180^\circ$ . These three angles are exactly the three CKM phases that appear in the above classification of  $CP$  asymmetries:  $\varphi_1 = \phi$ ,  $\varphi_2 = \delta + \phi$ , and  $\varphi_3 = \delta$ .

The quantities that will be directly determined by measurement of the  $CP$ -violating asymmetries (15) in decays to  $CP$  eigenstates are

$$\sin 2\varphi_1 = \sin 2\phi = \text{Im} \left( \frac{V_{td}^*}{V_{ub}^*} \right) = \frac{2\rho \sin \delta (1 - \rho \cos \delta)}{1 + \rho^2 - 2\rho \cos \delta}, \quad (33)$$

$$\sin 2\varphi_2 = \sin 2(\delta + \phi) = \text{Im} \left( \frac{V_{ub}^*}{V_{ub}^*} \right) \left( \frac{V_{td}^*}{V_{td}^*} \right) = \frac{2 \sin \delta (\cos \delta - \rho)}{1 + \rho^2 - 2\rho \cos \delta}, \quad (34)$$

$$\sin 2\varphi_3 = \sin 2\delta = \text{Im} \left( \frac{V_{ub}^*}{V_{ub}^*} \right). \quad (35)$$

where  $\rho$  is the CKM-matrix parameter defined in Eq. 22. It is interesting to estimate the allowed regions of the  $\sin 2\varphi_i$  based on present knowledge of the CKM-matrix parameters, and on the top-quark mass. The relevant experimental results are

$$\lambda = 0.22 \text{ (the Cabibbo angle),}$$

The CKM parameter  $A = 1$  to good accuracy from the  $B$ -meson lifetime,

$$|\epsilon| = (2.26 \pm 0.02) \times 10^{-3} \text{ from } K \text{ decay,}$$

$$x_d = 0.72 \pm 0.10 \text{ from ARGUS and CLEO,}$$

$$V_{cb} = 0.046 \pm 0.010,$$

$$\rho = 0.52 \pm 0.08 \text{ from } |V_{ub}/V_{cb}| = 0.115 \pm 0.018 \text{ at ARGUS and CLEO,}$$

$$\tau_B = 1.18 \pm 0.12 \text{ ps.}$$

From these constraints we deduce the 90% confidence limits shown in Fig. 5 for three values of  $M_t$ . We infer that  $\sin 2\varphi_1$  and  $\sin 2\varphi_2$  cannot both be small, but that  $\varphi_2$  could be near  $90^\circ$  for  $M_t \sim 150 \text{ GeV}/c^2$ .

The example final states given in (31) for the asymmetry classes are the most useful for BCD. From Tables 3 and 4 we find for the tree-level graphs

**Class 1:**  $B_d^0 \rightarrow J/\psi K_S^0, J/\psi \rho^0, D^+ D^-, D^0 \bar{D}^0$ , and  $D_s^+ D_s^-$ . All but the first of these are CKM-suppressed. Not shown in the Tables are such related decays as  $\chi K_S^0$ , and  $\eta_c K_S^0$ . The pure penguin decays  $B_d^0 \rightarrow \phi K_S^0$  and  $B_s^0 \rightarrow \phi K_S^0$  also belong to this class.

**Class 2:**  $B_d^0 \rightarrow \pi^+ \pi^-, \rho^0 \rho^0, K^+ K^-, D^0 \bar{D}^0$ , and  $\rho^0 K_S^0$ . The first 4 are CKM-suppressed, and the fourth is doubly CKM-suppressed. Because  $D^0 \bar{D}^0$  belongs to both classes 1 and 2 with similar strength its utility in determining the CKM phases is limited.

Class 3:  $B_s^0 \rightarrow \rho^0 K_S^0$ ,  $\rho^0 \phi$ ,  $K^+ K^-$ ,  $\pi^+ \pi^-$ , and  $\rho^0 \rho^0$ . The first is CKM-suppressed, and the last four are doubly CKM-suppressed (although penguin contributions to all but  $\rho^0 K_S^0$  are CKM-favored).

Class 4:  $B_s^0 \rightarrow D_s^+ D_s^-$ ,  $J/\psi \phi$ ,  $D^0 \bar{D}^0$ ,  $D^+ D^-$ , and  $J/\psi K_S^0$ . The last is CKM-suppressed.

Note that the interesting classes 2 and 3 are always CKM suppressed.

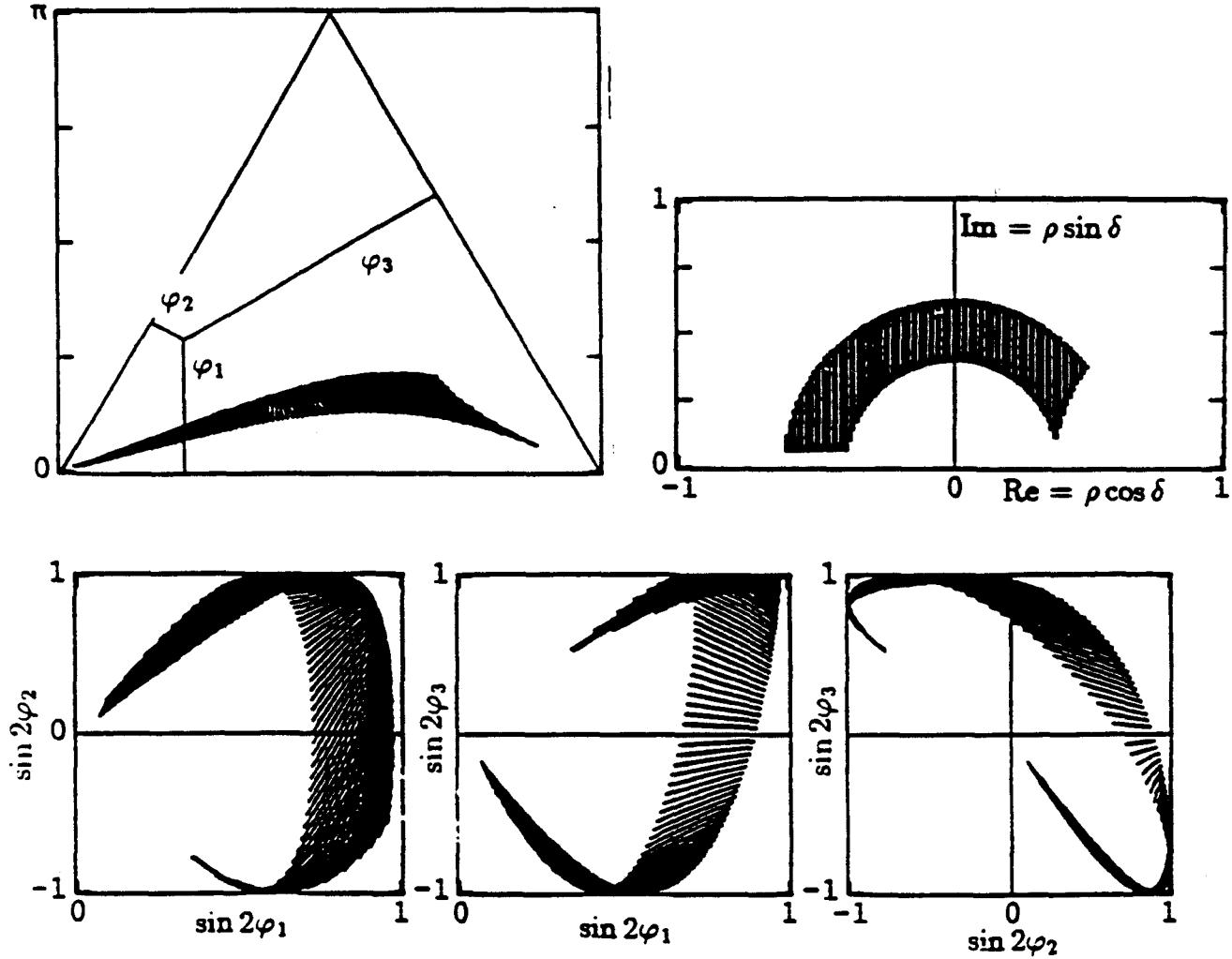


Figure 5: Allowed regions of the  $\varphi_i$  at 90% confidence, based on present knowledge of the CKM matrix. In the triangle plot,  $\varphi_1 + \varphi_2 + \varphi_3 = \pi$ . The top-quark mass was taken to be  $150 \text{ GeV}/c^2$ .

There are some theoretical uncertainties in the modes such as  $B_d \rightarrow \pi^+ \pi^-$  and  $B_s \rightarrow \rho K_S$  in which there is a penguin-graph contribution in addition to the favored tree-level spectator graph. The argument that led to Eqs. 26 and 27 was based on the assumption that only one weak amplitude contributes to the decay of a  $B$  meson to a  $CP$  eigenstate. Therefore



the result  $|\rho_f| = 1$  must be reconsidered. This has been done<sup>[17]</sup> – the effects of the penguin diagrams are difficult to calculate, but have been estimated to be not more than 20%. On the other hand, the prediction for the mode  $B_d \rightarrow J/\psi K_S$  is theoretically quite safe.

The penguin graphs can also be classified on the basis of the CKM-phase information they contain

Class 1.  $B_d$  decays with  $b \rightarrow s$  ( $B_d \rightarrow J/\psi K_S^0, \rho^0 K_S^0, \phi K_S^0$ , and  $\pi^+ \pi^-$ ).

Class 4.  $B_d$  decays with  $b \rightarrow d$  ( $B_d \rightarrow D^+ D^-, J/\psi \rho^0, \rho^0 \rho^0, D^0 \bar{D}^0, D_s^+ D_s^-, K^+ K^-, \phi \phi, \phi \rho^0$ , and  $K^{*0} \bar{K}^{*0}$ ). Here, both mixing and the decay amplitudes depend on  $V_{td}$ , but the phases cancel.

Class 4.  $B_s$  decays with  $b \rightarrow s$  ( $B_s \rightarrow D_s^+ D_s^-, J/\psi \phi, D^0 \bar{D}^0, D^+ D^-, \rho^0 \rho^0, \phi \rho^0, \phi \phi, K^+ K^-, K^{*0} \bar{K}^{*0}$ , and  $\pi^+ \pi^-$ ).

Class 1.  $B_s$  decays with  $b \rightarrow d$  ( $B_s \rightarrow J/\psi K_S^0, \rho^0 K_S^0$ , and  $\phi K_S^0$ ).

Two-body final states in which both particles have nonzero spin are not, in general, pure  $CP$  eigenstates, but mixtures of  $CP +$  and  $CP -$ , due to the different possible orbital angular momenta. For these states, such as  $J/\psi \phi, J/\psi \rho^0, \phi \phi, \phi \rho^0, \rho^0 \rho^0$ , and also  $p\bar{p}$ , the simple relation between the  $CP$  asymmetry and phase of the CKM matrix no longer holds. However, for particular polarizations of the final-state particles the elegant relations can be recovered. Additional measurements of  $CP$  violation will be possible with event samples sufficiently large to permit spin-density-matrix analyses.

Although we have emphasized the time dependence of the  $CP$  asymmetries in Eq. 27, these can also be measured using time-independent techniques. Integrating over time, we find

$$A_f = -\frac{x_q}{1+x_q^2} \text{Im } \alpha_f . \quad (36)$$

For a time-integrated measurement to be interpreted it is necessary to have an accurate measurement of the mixing parameter  $x_q$ . At a hadron collider where a vertex detector must be used to isolate the  $B$ -decay products, the time-resolved measurements will consequently be possible. However, the large mixing parameter  $x_s$  renders time-integrated measurements useless for  $B_s$  decays.

Finally, it is interesting to examine why  $CP$ -violation measurements in the Kaon system do not directly access the phases of the CKM matrix. Many of the needed ingredients are present:  $\pi\pi$  is a  $CP$  eigenstate,  $|p/q|_K \simeq 1$ , and a single weak amplitude dominates the decay. However, the CKM structure of the amplitude (and of  $K^0$ - $\bar{K}^0$  mixing) involves only the  $uc$ - $ds$  submatrix to a first approximation, and the elements  $V_{ub}$  and  $V_{tb}$  that have nontrivial phases enter only as small correction. The Kaon system does not 'know' enough about the third quark generation to be an ideal laboratory for  $CP$  violation.

### 2.4.2 Sensitivity of the BCD to CKM Phase

The principal result of the preceding subsection is that the time-resolved  $CP$ -violating asymmetry in the decay of neutral  $B$  mesons to  $CP$  eigenstates can be written

$$A(t) = \frac{\Gamma(B_q^0(t) \rightarrow f) - \Gamma(\bar{B}_q^0(t) \rightarrow \bar{f})}{\Gamma(B_q^0(t) \rightarrow f) + \Gamma(\bar{B}_q^0(t) \rightarrow \bar{f})} = \sin 2\varphi \sin x_q t / \tau,$$

where  $\varphi$  is a phase directly related to CKM-matrix elements, and  $x_q$  is the mixing parameter of the  $B_q$  mesons. Strictly, this relation holds only when the decay is dominated by a single weak amplitude, and the interference required to produce an asymmetry arises from the mixing.

To extract the amplitude,  $\sin 2\varphi$ , of the time-resolved asymmetry  $A(t)$  we must note a 'dilution factor' not present in a time-independent asymmetry (such as that discussed in sec. 2.3). For a small mixing parameter  $x_q$ , only the first wiggle in Eq. 26 will be significant (due to the relatively rapid decay), and the time-resolved asymmetry measurement reduces to integrating over this wiggle, which becomes equivalent to the time-integrated measurement (36). That is, the effective asymmetry is

$$A \rightarrow \frac{x_q}{1 + x_q^2} \sin 2\varphi, \quad \text{small } x_q.$$

For large  $x_q$ , however,  $\sin x_q t / \tau$  oscillates before the  $B$ 's decay, and the asymmetry measurement can be thought of as comparing alternate half cycles. In this case the effective size of the asymmetry is only reduced by the average amplitude of a half cycle of a sine wave:

$$A \rightarrow \frac{2}{\pi} \sin 2\varphi, \quad \text{large } x_q.$$

A complete analysis shows that we can write

$$A = D(x_q) \sin 2\varphi \quad \text{with} \quad D = \frac{x_q}{1 + x_q^2} \coth(\pi/2x_q).$$

(The dilution factor  $D$  is the Laplace transform of  $|\sin x_q t / \tau|$ , which arises because the effective signal is  $e^{-t/\tau} |\sin x_q t / \tau|$  compared to exponential-decay 'background'.)

Although the dilution  $D$  due to mixing is annoying, without mixing the richness of  $CP$  violation in the  $B$  system would be greatly reduced.

Assuming our vertex detector has sufficient accuracy to resolve the mixing oscillations (cf. sec. 2.2), the statistical significance in standard deviations of a measurement of  $\sin 2\varphi$  via the effective asymmetry  $A = D \sin 2\varphi$  follows from the discussion in sec. 2.3, namely

$$S = \frac{\sin 2\varphi}{\sigma_{\sin 2\varphi}} = \sqrt{N} \frac{D \sin 2\varphi}{\sqrt{1 - D \sin^2 2\varphi}},$$

where  $N$  is the total number of (true) reconstructed, tagged decays. The minimum value of  $\sin 2\varphi$  that could be resolved to three standard deviations with  $N$  events is then

$$\sin 2\varphi_{\min, 3\sigma} = \frac{3}{D\sqrt{N+9}}.$$

To perform the asymmetry measurement we must tag the other  $B$  in the event to determine the initial particle/antiparticle character of the  $B$  that decays to the  $CP$  eigenstate. As discussed in section 2.2 above, at a hadron collider we will likely have only a partial reconstruction of the second  $B$ , and will not distinguish  $B_u$ ,  $B_d$ , and  $B_s$ . Because of the mixing of the neutral  $B$ 's there will be a probability  $p \approx 0.15$  of a mistag, which dilutes the significance of the asymmetry measurement.

We also consider the effect of backgrounds in our sample of  $CP$ -eigenstate decays, supposing that for each true reconstruction of  $B \rightarrow f$  there are  $b$  false reconstructions that exhibit zero asymmetry. Then  $1/b$  is the signal-to-noise for reconstruction of this decay mode.

Taking into the account these two effects, the apparent rate for  $B (\bar{B})$  decay will be

$$\Gamma(\overset{(-)}{B}_q^0(t) \rightarrow \overset{(-)}{f}) = |(f|B_q^0)|^2 e^{-t/\tau} \left[ 1 + b \mp (1 - 2p) \text{Im } \alpha_f \sin \alpha_q \frac{t}{\tau} \right],$$

and the true  $CP$ -violating asymmetry  $A_{CP}$  will be related to the asymmetry  $A_{\text{obs}}$  observed in the laboratory by

$$A_{CP} = \frac{1 + b}{1 - 2p} A_{\text{obs}}.$$

As a consequence, the statistical power of a sample of  $N$  true events is reduced, and we now have (assuming that  $b$  and  $p$  are well known)

$$\sin 2\varphi_{\text{min},3\sigma} = \frac{3(1 + b)}{D(1 - 2p)\sqrt{N(1 + b) + 9}}.$$

With  $p = 0.15$  we expect  $1 - 2p = 0.6$ , as discussed in section 2.2.

Consideration of the tagging efficiency has also been given in section 2.2, where we estimated that a tag based on the sign of the leading electron or muon in semileptonic decays would have about 3% efficiency.

The expectations for rates of three decays to  $CP$  eigenstates are

$\varphi_1$  can be determined from  $B_d^0 \rightarrow J/\psi K_S^0 \rightarrow e^+e^-\pi^+\pi^-$  or  $\mu^+\mu^-\pi^+\pi^-$ . Table 9 indicates that the BCD could reconstruct  $3 \times 10^5$   $e^+e^-\pi^+\pi^-$  decays in  $10^7$  sec of running at a luminosity of  $10^{32} \text{ cm}^{-2}\text{sec}^{-1}$ . As muons are identified only in the Intermediate and Forward regions, the  $\mu^+\mu^-\pi^+\pi^-$  is only about 0.6 times the  $e^+e^-\pi^+\pi^-$  sample, for a total of  $4.8 \times 10^5$   $J/\psi K_S^0$  events. The number of tagged and reconstructed events would then be 14,400. This mode will be relatively background free so long as the mass resolution is smaller than  $M_\pi$ . We estimate the background-to-signal to be  $b \sim 0.1$

$\varphi_2$  can be determined from  $B_d^0 \rightarrow \pi^+\pi^-$ . From the  $2 \times 10^6$  events expected in Table 9, there would be 60,000 tagged, reconstructed events. The  $\pi^+\pi^-$  is one of the most background prone as a fake secondary vertex is more likely for two tracks than for three. From Monte Carlo simulations of the vertexing algorithm we estimate that  $b \sim 1$ .

$\varphi_3$  can be determined from  $B_s^0 \rightarrow \rho^0 K_S^0 \rightarrow \pi^+\pi^-\pi^+\pi^-$ . From the 13,000 events expected in Table 9, only about 400 remain after the tagging requirement. The background in this mode may be significant, and without having made a detailed study we suppose that  $b \sim 1$ .

Table 11: The minimum values of  $\sin 2\varphi$  resolvable to three standard deviations in  $10^7$  sec of running at luminosity of  $10^{32}$   $\text{cm}^{-2}\text{sec}^{-1}$ . The mistagging factor is taken as  $1 - 2p = 0.6$ . The dilution factor  $D$  due to mixing is given by  $x_q \coth(\pi/2x_q)/(1 + x_q^2)$ .

Angle	Mode	Tagged Events	$b$	$x_q$	$D$	$\sin 2\varphi_{\min,3\sigma}$
$\varphi_1$	$B_d^0 \rightarrow J/\psi K_S^0$	14,400	0.1	0.7	0.47	0.094
$\varphi_2$	$B_d^0 \rightarrow \pi^+\pi^-$	60,000	1.0	0.7	0.47	0.062
$\varphi_3$	$B_s^0 \rightarrow \rho^0 K_S^0$	400	1.0	$\sim 10$	0.64	0.55
$\varphi_3$	$B_s^0 \rightarrow K^+K^-$	1,560	$\sim 0.1$	$\sim 10$	0.64	0.21

Table 11 indicates the smallest values of the  $\varphi_i$  that could be resolved in one year of running at the BCD. The rates for the  $B_s$  decays are based on branching ratios (see Table 9) that are lower limits. Still, in view of the limited accuracy in  $\varphi_3$ , it would be desirable to do even better. A significant loss of statistical power occurs because of the tagging requirement, whose overall efficiency is about 3% if the only tag is on the charge of the leading electron or muon in semileptonic  $B$  decays. Clearly it will be very advantageous to devise a tag based on some substantial fraction of the nonleptonic decays that comprise 70% of all  $B$  decays.

The tagging strategy is also closely related to the experimental trigger, which has not been discussed thus far. We anticipate an evolution of thinking about these critical issues in the coming years. It would be extremely valuable to have the opportunity to focus our thought via an interim, smaller-scale  $B$  experiment at a hadron collider prior to running at the SSC.

## 2.5 Gluon and Sea-Quark Distributions at Small $x$

The most recent global analysis of deep inelastic and Drell-Yan scattering at fixed target facilities<sup>[24]</sup> has shown that the low- $x$  ( $< 0.01$ ) behavior of the gluon and sea quarks is very poorly determined. In particular, current data can not discriminate between a low- $x$  power-law behavior ( $x^{-A}$ ), a logarithmic behavior ( $\log^{G(1/x)}$ ) or a composite behavior with both factors. The most efficient way to determine this low- $x$  behavior is to look at exclusive processes at collider facilities that are sensitive to this term. These processes include Drell-Yan and direct photon production as well as  $B-\bar{B}$  pair production.

As a test of a possible power-law behavior Olness and Tung<sup>[25]</sup> have shown that the integrated cross section for  $B-\bar{B}$  pairs can vary by as much as a factor of 7 as the value of  $A$  ranges from 1 to 1.5. A measurement of this cross section to an accuracy of 20% could determine  $A$  to around 10%. Drell-Yan scattering, although orders of magnitude less copious than  $B-\bar{B}$  pair production, is sensitive to  $A$  not only in the total cross section but also differentially. It should thus be able to successfully discriminate between power-law and logarithmic  $x$  dependence. A combined Drell-Yan,  $B-\bar{B}$  analysis should fix the low- $x$

behavior of both the gluon and sea quarks all the way down to  $x = 0.0001$ .

### 3 Detector Overview

The general features of a detector for  $B$  physics at the SSC are determined by the issues discussed in sec. 2. The goal of detailed study of  $CP$  violation in the  $B$  system is very useful in setting a clear standard for detector performance.

- Such a study of  $CP$  violation will require of order  $10^{12}$  produced  $B$ 's. To obtain these in one running year requires the detector to operate at a luminosity of  $\sim 10^{32} \text{ cm}^{-2}\text{sec}^{-1}$ .
- The  $B$ -decay products are distributed over  $\pm 7$  units of pseudorapidity  $\eta$ , and have average transverse momentum of about  $0.6 \text{ GeV}/c$  (see Fig. 4). The density vs. angle of particles from  $B$  decay differs very little from that for a typical  $p$ - $p$  interaction. A  $B$ -physics detector will place much greater emphasis on forward angles and low transverse momentum than a detector for the Higgs sector.
- The  $B$ -decay products can be isolated from the high-multiplicity of particles from the primary  $p$ - $p$  collision by means of a silicon vertex detector ( $c\tau$  for a  $B$  meson is  $360 \mu\text{m}$ ). This restricts the detector to the study of charged tracks; calorimetry for hadrons and photons plays little role. The vertex detector is the most critical item in the experiment. To function well it must be placed with  $\sim 1 \text{ cm}$  of the beams, which exposes the detector to the hazard of radiation damage. This concern alone may limit the operation of the experiment to a luminosity of  $10^{32} \text{ cm}^{-2}\text{sec}^{-1}$ .
- There are 79 basic two-body nonleptonic decay modes of the  $B_u$ ,  $B_d$ , and  $B_s$  mesons (see Tables 2-4). All of these modes have all-charged final states after secondary decay. The exploration of this great variety of decay channels requires a magnetic spectrometer with tracking and identification of  $\pi^\pm$ ,  $K^\pm$ ,  $e^\pm$ , and  $\mu^\pm$ .
- To provide redundancy in the high-multiplicity collider environment, each of the  $\sim 100$  charged tracks per primary interaction should be sampled  $\sim 100$  times. To keep the detector occupancy at the 1% level there should be  $\sim 10^6$  detector elements. Another way of stating this criterion is used often below: we design for up to 10 tracks per unit of pseudorapidity  $\eta$  and desire 1% occupancy; hence each detector layer should have 1000 cells per unit of  $\eta$ .
- The detector must have a very high performance data-acquisition system. Each event will have  $\sim 100$  tracks  $\times \sim 100$  detector layers  $\times \sim 5$  (signal + noise hits)/layer/track  $\times \sim 10$  bytes/sample  $\Rightarrow \sim 5 \times 10^5$  bytes/event. There are  $\sim 10^7$  events/sec at a luminosity of  $10^{32} \text{ cm}^{-2}\text{sec}^{-1}$ , and  $\sim 1\%$  of these contain  $B$ 's. Hence the data-flow rate off the detector will be  $\sim 5 \times 10^{10}$  bytes/sec. This assumes a prompt trigger for the experiment that reduces the primary event rate by a factor of  $10^{-2}$ . A weaker trigger of course implies a greater data flow off the detector.
- The detector must be supported by a very powerful online computer (processor ranch). Even in the year 2000 it will likely be impractical to record  $5 \times 10^{10}$  bytes/sec, so

a software 'trigger' should be implemented to reduce the archival event rate by an additional factor of  $10^{-2}$  to  $\sim 10^{-4}$  of the primary event rate, implying  $5 \times 10^8$  bytes/sec written to 'tape.' If we suppose it requires 10 MIPS-seconds to perform the software-trigger calculation, the online computer must have  $\sim 10^6$  MIPS of processing power to deal with the  $10^5$  events/sec that flow off the detector.

The detector we propose, the Bottom Collider Detector (BCD), to meet these requirements is shown in an isometric view in Fig. 6, and in plan and section in Fig. 7. As previewed in sec. 2, mechanical considerations lead the detector to be divided into three regions:

1. The Central region covers  $|\eta| < 1.2$  ( $\theta > 580$  mrad). The Central detector is inside a 10-kG magnetic field oriented transverse to the beams.
2. The Intermediate region covers  $1.2 < |\eta| < 3.5$  ( $60$  mrad  $< \theta < 580$  mrad). The Intermediate detector consists of two arms on either side of the Central detector.
3. The Forward region covers  $3.5 < |\eta| < 5.5$  ( $8$  mrad  $< \theta < 60$  mrad). The maximum  $\eta$  covered by the Forward detector is subject to further consideration, some of which is presented below. In this Expression of Interest we propose implementing only one of the two possible forward arms, although building both arms remains under consideration. If only one Forward arm is built, the Intermediate arm on the opposite side could be extended to cover  $\eta$  up to 4 ( $\theta > 37$  mrad).

Before discussing the several detector subsystems of the BCD we address the question of how far forward is it practical to observe. The answer is tied to expectations of performance of the silicon vertex detector, and the problem of photon conversions in the beam pipe.

- We place the silicon detector outside the beam pipe, which is taken to have a radius of 1.25 cm. Considerable mechanical difficulties arise in placing the silicon detector inside the beam pipe, which would have the effect, among others, of rendering a Central detector almost useless.
- To survive the radiation damage encountered at a luminosity of  $10^{32}$  cm<sup>-2</sup>sec<sup>-1</sup>, the silicon vertex detector cannot be located closer than 1.25 cm to the beams.
- To survive radiation damage the gas tracking detectors of the Forward arm must be located at least 10 cm from the beams. This is based on estimates of aging in gaseous wire chambers. If  $\theta_{\min}$  is the smallest angle covered, the Forward detector must begin at distance  $D > (0.1 \text{ m})/\theta_{\min}$  from the interaction point.
- The tracks found in the Forward tracking system must extrapolate accurately to their matches in the silicon detector. This should not be a critical limitation, as argued by the following. We require the error on the extrapolation from the Forward tracking into the silicon vertex detector to be 1/10 the typical track separation. We estimate the latter from the angular density of tracks at the SSC, which is  $dN/d\eta \approx 6$ , so  $dN/d\theta \approx 6/\theta$ . The interval  $d\theta$  in which  $dN$  is 1/10 is then  $d\theta = \theta/60$ . In the silicon detector the tracks at angle  $\theta_{\min}$  are measured at a radius of about 1 cm, so an angular separation  $d\theta = \theta/60$  corresponds to a spatial separation of  $dr \sim (1 \text{ cm})d\theta/\theta \approx 167 \mu\text{m}$ .

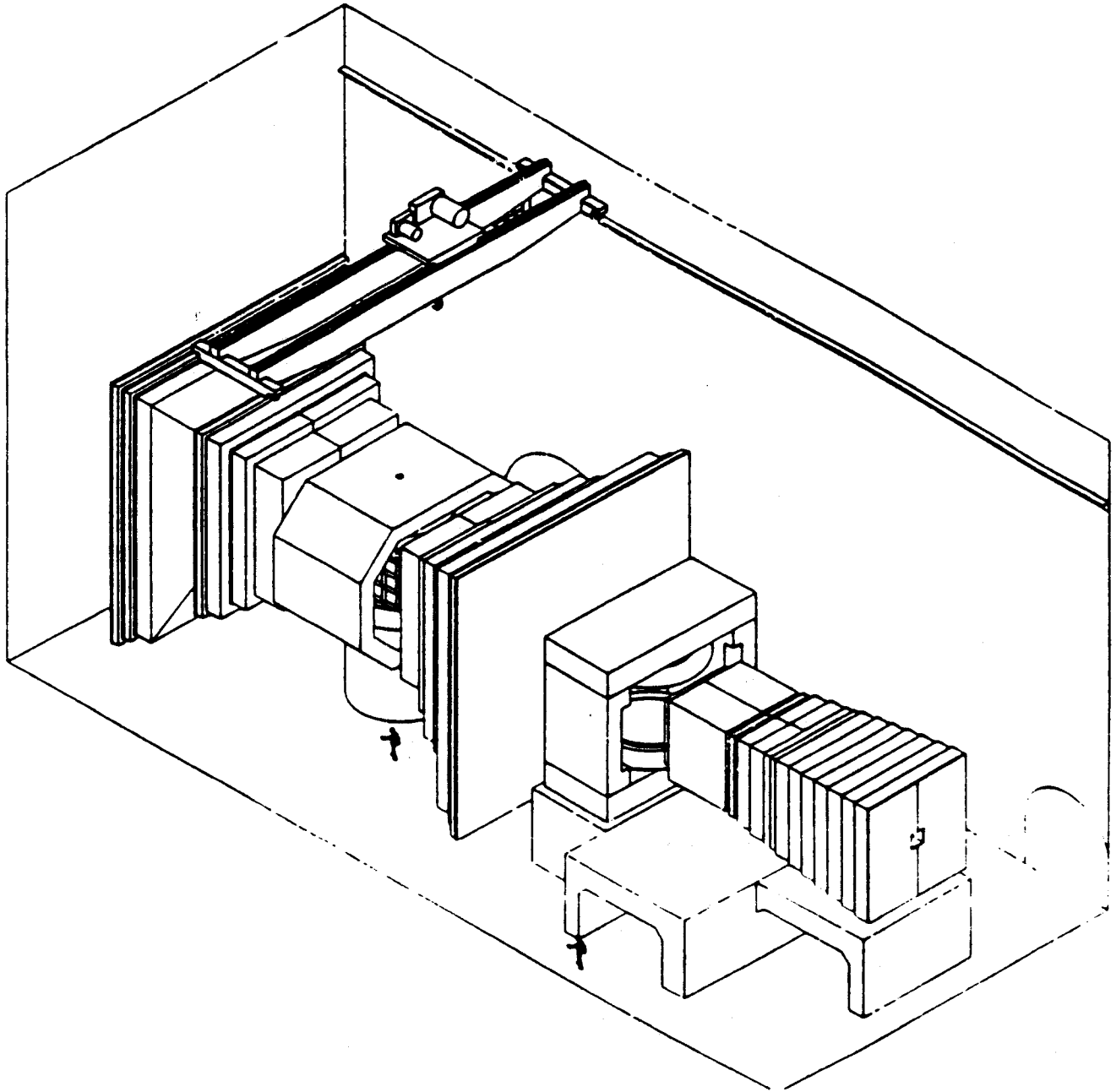


Figure 6: Isometric view of the BCD.

This is the required error on the extrapolation of the tracks measured in the Forward tracking system. The latter quantity is given by  $D\sigma_r/L$ , where  $\sigma_r$  is the resolution in the Forward tracking system, and  $L$  is the path length over which tracks are measured in that system. Plausible values are  $\sigma_r \approx 50 \mu\text{m}$ , and  $L = 10 \text{ m}$ . If so,  $D$  could be as large as 30 m, and  $\theta_{\text{min}} = 1/300$  corresponding to  $\eta_{\text{max}} \approx 6.4$ .

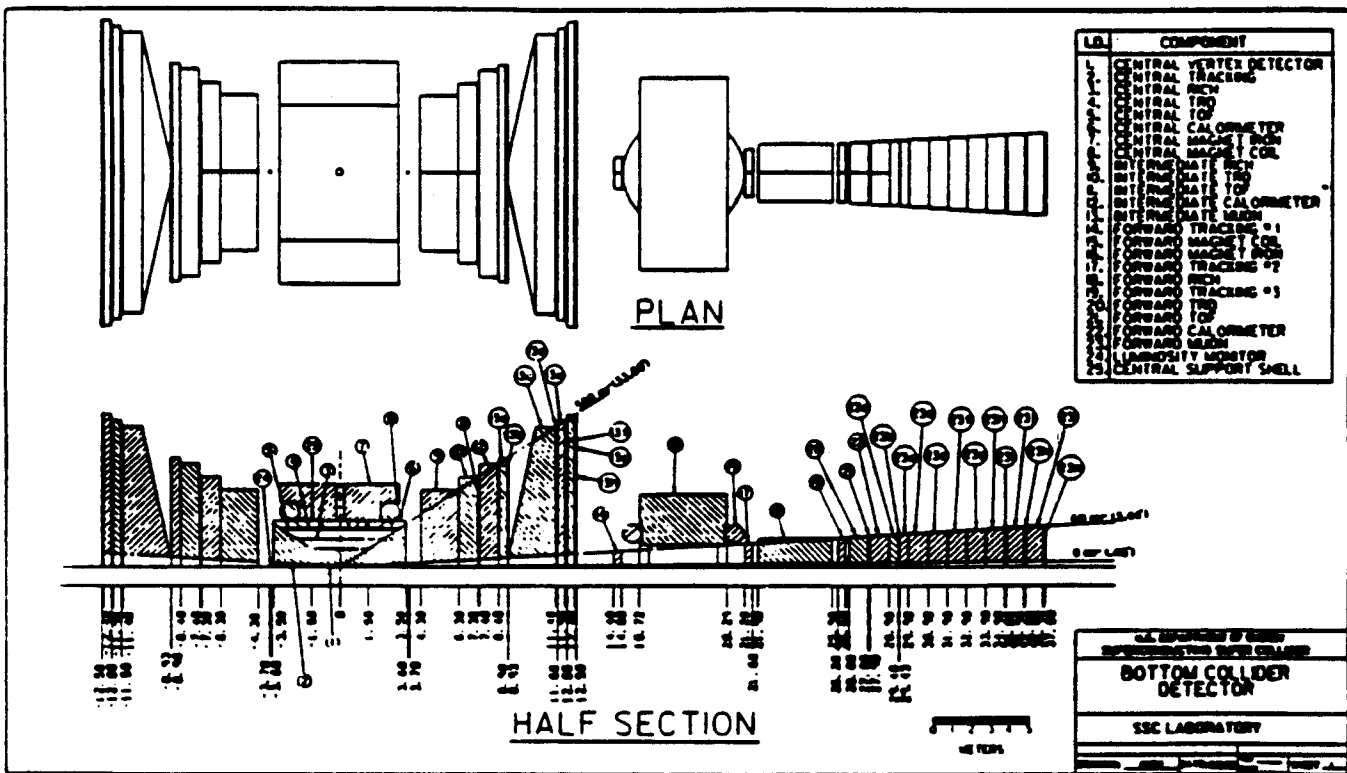


Figure 7: Plan and section views of the BCD. Central Detector: 1: silicon vertex detector, 2: straw-tube tracking system, 3: RICH counter, 4: transition radiation detector, 5: time-of-flight system, 6: electromagnetic calorimeter, 7: magnet yoke, 8: superconducting coil. Intermediate Detector: 9: RICH counter, 10: TRD, 11: time-of-flight, 12 E-M calorimeter, 13: Muon system. Forward Detector: 14, 17, 19: tracking, 15: superconducting coil, 16: magnet yoke, 18: RICH counter, 20: TRD, 21: time-of-flight, 22: E-M calorimeter, 23 muon system, 24: luminosity monitor, 25: central support shell.

- A more important issue associated with the value of  $\theta_{\min}$  is the conversion in the beam pipe of photons from  $\pi^0$  decay and the degradation of vertex resolution due to multiple Coulomb scattering in the beam pipe. While a beam pipe of 400- $\mu\text{m}$ -thick Be is contemplated, its effective number of radiation lengths is  $0.01/\theta$ , which becomes 3 at  $\theta = 1/300$ , which renders the detector problematic at such small angles. In an attempt to reduce the radiation lengths encountered, we consider the use of a flared beam pipe, illustrated in Fig. 8, with cones at  $\eta = 3.5, 4.2, 4.8,$  and  $5.4$ . However, the merits of the cones at  $\eta = 4.8$  and  $5.4$  are doubtful: for an interaction 10 cm in  $z$  from the nominal interaction point the cone at  $\eta = 4.8$  subtends an angular range  $d\theta \approx 0.0015$  centered on angle 0.001, or  $d\theta/\theta \approx 1.5$ . There might be as many as 10 photons in this interval (using  $dN_{\gamma}/d\eta \approx dN_{\pi^{\pm}}/d\eta \approx 6$ ), for which the apparent thickness of the flared beam pipe is 10 radiation lengths. Thus a flared beam pipe is worse than a simple cylindrical one for a finite-length interaction region. We feel that interactions in the beam pipe



will limit the extent of the Forward region to  $\eta_{\max}$  of 5-5.5.

- In the present Expression of Interest we take the Forward detector to begin immediately beyond the Intermediate detector, at a value of  $D = 13$  m. This sets  $\theta_{\min} = 1/130$  corresponding to  $\eta_{\max} = 5.5$ . The merits of a possible flares in the beam pipe at  $\eta = 3.5$  and 4.2 remain to be studied in detail. Simple estimates indicate that it would lead to a slightly smaller average radiation length encountered per track than a cylindrical pipe.

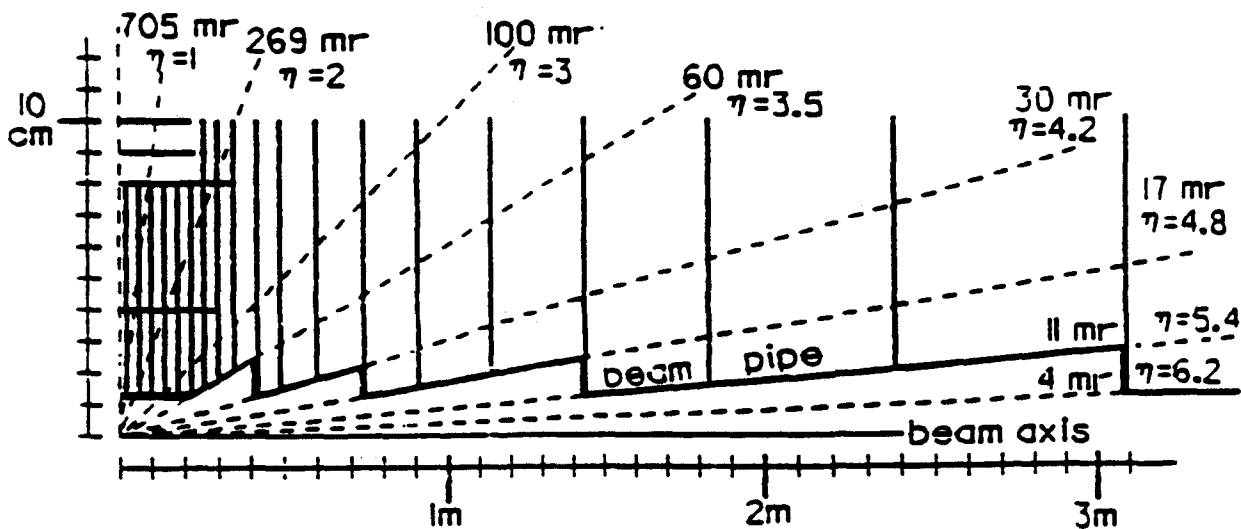


Figure 8: A possible configuration of the silicon vertex detector and beam pipe, showing flares in the latter at several values of  $\eta$ . The beam pipe has a minimum radius of 1.25 cm and is made of 400- $\mu\text{m}$ -thick Be. Near the interaction point the vertex detector consists of both 'barrels' of detectors parallel to the beams, and 'disks' of detectors perpendicular to the beams. At forward angles only disk detectors are used. All disks come within 2.1 cm of the beams, as limited by the flares.

### 3.1 Detector Subsystems

We introduce briefly the various subsystem of the BCD, indicating their function, technology, and approximate channel count. Related summaries of detector parameters are given in Table 23.

1. **Dipole Magnets.** The kinematics of  $B$ -meson production at the SSC are not well matched to the use of a solenoidal magnet. The  $B$  decay products are distributed approximately as  $dN/d\theta \sim 1/\theta$ , which suggests use of a magnetic field that is transverse to the beam direction. Momentum analysis for particles in the Central and Intermediate regions can be provided by a single dipole magnet with a 7-Tesla-m field integral centered on the interaction point. We propose to use a magnet with circular pole tips to simplify construction, and to provide circular field symmetry to aid in momentum reconstruction. The magnet gap is 5 m high, the pole tips are 4 m in radius, and the total weight of the magnet is 2000 tons. The large gap accommodates the tracking and particle identification systems in the Central detector. We are investigating the feasibility of using the MFTF superconducting coils built by General Dynamics.

The field of the Central dipole magnet deflects the proton beams, and must be compensated. This compensation could be conveniently provided by a second analysis dipole magnet in the Forward detector. This magnet has a 2.7-m high gap, and pole tips 4 m in radius; these are similar to the specifications of the Chicago Cyclotron magnet shimmed to a larger gap.

2. **Silicon Vertex Detector.** This device is the critical detector element of the BCD as it identifies the tracks belonging to  $B$  decays via reconstruction of a secondary vertex. The vertex detector must provide three-dimensional coordinate measurements of accuracy  $\sim 5 \mu\text{m}$ , which then yields an accuracy on the distance between primary and secondary vertices of  $\sim 20 \mu\text{m}$ . This value is to be compared to the decay length of  $B$  mesons,  $c\tau = 360 \mu\text{m}$ .

We propose to build the vertex detector using silicon  $p$ - $i$ - $n$  diode arrays with local VLSI readout. In an option based on ministrips, the size of the detector element varies from  $25 \mu\text{m} \times 5 \text{mm}$  at a radius of 1.25 cm to  $50 \mu\text{m} \times 5 \text{cm}$  at a radius of 10 cm. These sizes are chosen to provide the required spatial resolution and to limit the confusion of hits from different tracks to less than 0.5% per detector layer. Another option is square pixel elements. The technologies to build these devices will be an extension of those now used to make ac-coupled, double-sided  $p$ - $i$ - $n$  diode arrays and associated readout chips. This extension includes the development of fast, radiation-hard readout chips.

The silicon detectors will be arrayed as sketched in Fig. 8 with both 'barrel' and 'disk' detectors near the interaction point, but only disk detectors at forward angles. The average number of strips on a detector that are struck by a charged particle is  $\sim 5$  in the  $4\pi$  collider geometry. The goal of only 1% strip occupancy in a system with an average of 10 strip planes per track (counting both sides of the detectors) leads to a total of  $\sim 10^6$  strips. These are located on  $\sim 1000$  silicon wafers that are read out via  $\sim 10,000$  custom VLSI chips with 128 channels each.

The silicon detectors come within 1.25 cm of the beams to minimize the extrapolation to the vertices, but which exposes the detectors to considerable radiation. The vertex detector extends to a maximum radius of 10 cm, and has total length of 6 m along the beam. The vertex detector has a projected power consumption of 1.5 kWatts, which can be cooled by gas flow.

The vertex detector also provides substantial track-pattern recognition and excellent momentum measurement for tracks at small angles ( $\eta \gtrsim 3$ ). However, to provide accurate momentum measurement and good pattern recognition at large angles an additional tracking system is required.

3. **Straw-Tube Tracking System.** The goal of the tracking system is to provide a resolution of  $25 \text{ MeV}/c^2$  at the  $B$ -meson mass. This requires a momentum resolution of about 0.7% for the  $B$ -decay products that have  $P_t$  in the range 0.3-2.5  $\text{GeV}/c$ , and laboratory momentum up to 300  $\text{GeV}/c$  at forward angles. The tracking system must also permit extrapolation of tracks into the silicon vertex detector with sufficient spatial accuracy to match the track segments properly.

We propose to use gaseous drift chambers in the form of straw-tube detectors for the tracking system. These offer relatively good accuracy ( $\sim 50 \mu\text{m}$  with a 'cool' gas; a slower drift velocity is not a problem at a luminosity of  $10^{32} \text{ cm}^{-2}\text{sec}^{-1}$ ), moderately low mass ( $\sim 0.1$  radiation length), and good reliability (due to the physical isolation of each sense wire). The straw tubes will be arrayed in 'superlayers' of 8-10 layers thick, which leads to the use of 'minivectors' defined by the hits in a superlayer as intermediate quantities in track pattern recognition. The straws will be arrayed vertically, and at angles of  $\pm 15^\circ$  to the vertical to provide small-angle-stereo measurements. The maximum straw-tube length will be 2 m. The straw tubes extend to within 10 cm from the beams, a limit set to avoid aging of the chambers due to radiation.

Tracking for particles in the Central and Intermediate detectors will be performed in a combined tracking system 6 m long and  $1.8 \times 1.8 \text{ m}^2$  in cross section. Each track will traverse about 64 straw tubes (8 superlayers), so the goal of 1% occupancy would require some 600k straw tubes. However, if the straw-tube diameter is 5 mm, only about 200k straws can be usefully arrayed in the Central and Intermediate tracking volume. In the Forward detector there are three additional stations of three superlayers each, which add 50,000 straw tubes to the system total.

4. **Time-of-Flight System.** We propose to identify  $\pi^\pm$  and  $K^\pm$  with transverse momenta between 0.3 and 3  $\text{GeV}/c$ . The lower limit arises as softer particles suffer too much multiple scattering to be reliably associated with secondary vertices, while the upper limit is chosen to contain 80% of all  $B$ -decay products (see Fig. 4). Hadron identification will be accomplished by a combination of a time-of-flight system at lower momenta, and RICH counters (item 5) at higher momenta. In addition to providing  $\pi$ - $K$  (and heavier charged particle) separation, the time-of-flight system will be useful in identifying multiple interactions within a single bunch crossing, and could be used in a multiplicity trigger.

The available flight paths are 2-2.4 m in the Central detector, 7.3 m in the Intermediate detector, and 28 m in the Forward detector. We propose to measure the flight times to 90-ps accuracy; which would effect  $\pi$ - $K$  separation for momenta up to 2, 4, and 8  $\text{GeV}/c$  in the Central, Intermediate, and Forward detectors, respectively. These are very aggressive specifications. To meet them we propose to have three time-of-flight scintillators, each 3-cm thick, traversed by each particle, and the scintillators in the Central region will be read out at both ends. The goal of 1% occupancy leads to

2500 azimuthal cells in each of the Central and two Intermediate detectors, and 2500 azimuthal cells in the Forward detector. The total number of channels is 37,500, given the multiple sampling of 3 or 6 per cell in angle.

5. **Ring Imaging Čerenkov Counters.** Hadrons with momenta too large to be analyzed in the time-of-flight system will be identified in RICH counters. To cover the part of the transverse-momentum range 0.3-3 GeV/c not identified in the time-of flight system, the RICH counters must operate in the momentum range 2-6 GeV/c in the Central detector, 4-60 GeV/c in the Intermediate detector, and 20-250 GeV/c in the Forward detector. The separation of pions and Kaons in these ranges is to be at least three standard deviations, and the Čerenkov rings should have 25 photoelectrons each to insure reliable pattern recognition.

These goals can be accomplished in the Central region with a 1-cm-thick liquid radiator,  $C_6F_{14}$ , followed by a 25-cm drift to the photodetector. The latter is a multistep avalanche chamber filled with TMAE gas at only a few-torr pressure. The readout is based on 'smart' cathode pads with wedge and strip electrodes yielding position resolution  $\sim 1/20$  the pad size. In the Intermediate region a 1-m gas radiator,  $C_6F_{12}$ , is used, and in the Forward region a 4-m gas radiator,  $CF_4$ . The photodetector is of the same type in all regions.

Supposing each ring image has 25 photoelectrons, there would be about 2500 hits per event in the RICH counters. We design for  $2 \times 10^5$  detector elements, yielding slightly more than 1% occupancy. There will be about 27,000 pads of size  $3 \times 3 \text{ cm}^2$  in the Central RICH counter, 155,000 pads of size  $2 \times 2 \text{ cm}^2$  in the Intermediate RICH counter, and 27,000 pads of size  $1.5 \times 1.5 \text{ cm}^2$  in the Forward RICH counter.

6. **Transition Radiation Detector.** Electron identification is provided by a combination of a transition radiation detector (TRD) and an electromagnetic calorimeter. The 'fine-sampling' transition radiation detector consists of 25 layers, each with 100 15- $\mu\text{m}$ -thick polyethylene foils spaced over 2 cm, followed by a xenon proportional chamber to detect the x-rays. This should permit an electron efficiency of 90% with only a 1% probability to misidentify pions as electrons. Such a TRD would be 75-cm thick, small enough to fit in the Central detector. The TRD is located in front of the time-of-flight system.

The goal of 1% occupancy suggests that there be 10,000 cells in solid angle for electron identification. However, the TRD may be operated with a threshold such that each layer has only 10% efficiency for pions. Then we may permit 4% or even 9% geometrical occupancy of the TRD cells and remain at less than 1% detected occupancy. If we design for 4% geometric occupancy there will be 2500 cells in solid angle, each with 25 radial samples, for a total of 62,500 detector elements.

7. **Electromagnetic Calorimeter.** Electron identification is also accomplished with an electromagnetic calorimeter. As the BCD has an analysis magnet, the calorimeter need not provide a precision energy measurement, but must emphasize  $e-\pi$  separation via characterization of the transverse and longitudinal profiles of the shower. We desire

electron identification down to 1-GeV/c transverse momentum, and that substantial pion rejection be available at the trigger level.

Our present design consists of a preconverter, two longitudinal sections, and a hadron catcher. We expect to take full advantage of the current R&D efforts in calorimetry. The calorimeter and the hadron catcher will be arranged in towers with  $\Delta\eta \times \Delta\phi = 0.08 \times 0.08$  so as to keep the occupancy and the  $\pi^\pm$ - $\pi^0$  overlap probability below 1%. This segmentation leads to 7000, 14000, and 6000 channels in the Central, Intermediate, and Forward detectors respectively. The preconverter will be integrated with the time-of-flight system. The preconverter will provide a shower-centroid measurement of approximately 1-mm accuracy. The combined rejection against pions in the TRD and E-M calorimeter should be better than  $10^5 : 1$ .

8. **Muon Detector.** Identification of muons allows the BCD to double its sensitivity to  $J/\psi$ 's resulting from  $B$  decay, and to double the efficiency for tagging and triggering on semileptonic  $B$  decays. Because the muons from  $B$  decay are at low transverse momentum it will not be practical to identify them in the Central detector. The Intermediate and Forward detectors will be equipped with iron absorbers and tracking chambers for muon identification.

The absorber for the Intermediate detector begins at 9 m from the interaction region and varies in thickness from 3 to 4 m, while the Forward absorber begins at 28 m and is 8 m thick. Due to pion decay before the absorber, muon identification will only be effective for transverse momenta above 1-1.5 GeV/c. Each tracking chamber will provide three measurements:  $x$  from the anode wires,  $y$  from cathode strips, and for triggering,  $(x,y)$  from coarse cathode pads. The chambers are built from extruded plastic channels, and are mounted in pairs to obtain full coverage. There are three pairs of chambers interspersed among the iron absorbers. The total channel count is 50,000 anode wires with TDC's, and 70,000 strips and pads with discriminators only.

9. **Luminosity Monitor.** Four planes of 0.5-mm-square scintillating fibers located at  $\pm 2$  and  $\pm 4$  m from the intersection point will monitor the luminosity, and provide a fast measure of the longitudinal position of the interaction vertex. The latter function is accomplished by matching hits in the two planes of fibers, which are oriented to measure tracks in the nonbend plane. There will be about 4000 fibers in all.
10. **Prompt Trigger.** A prompt and efficient trigger for  $B$  production at a hadron collider is difficult because events with  $B$ 's are only slightly different than 'minimum bias' events. About 1 event in 200 at the SSC will contain a  $B$ . The goal of the prompt trigger is to reduce the rate of events off the detector to about 1/50 of the primary event rate. Three types of triggers are under consideration: i) single electrons or muons above a  $P_t$  cut as low as 1 GeV/c; ii) a lepton pair consistent with  $J/\psi$  decay; iii) evidence for a secondary vertex in the nonbend plane.

Trigger ii) is the most straightforward, but studies only particular modes. The 'vertex trigger,' iii), will require considerable specialized processing power on the detector, as may be possible with devices such as the '3-D' processors from Hughes Aircraft. The

lepton triggers, i), have significant backgrounds that require software processing to eliminate.

The trigger scenario is the most difficult aspect of the BCD to project without actual experience. The BCD would converge on an effective trigger at the SSC much more quickly if we have the opportunity in the 1990's to explore  $B$  physics in an interim experiment.

11. **Data-Acquisition System.** Because of the large cross section for  $B$  production at the SSC, the data rate off the detector will be very high, perhaps  $5 \times 10^{10}$  bytes/sec at a luminosity of  $10^{32} \text{ cm}^{-2}\text{sec}^{-1}$ . This data rate must be reduced further before archiving, and we propose to implement software triggers in an extensive processor ranch of (at least)  $10^6$  MIPS. Before these processors can perform their algorithms the data must be routed to the relevant processors, i.e., event building must occur.

We envisage a data-acquisition architecture in which, in its simplest form, data is buffered on the detector itself until a prompt trigger is received (from hardware trigger circuitry). Then data from the selected events flow off the detector into a large switch based on telecommunications technology (roughly the size and functionality of a 10,000-line telephone exchange). The switch organizes the data blocks from many sources on the detector into contiguous events that are then routed to an available processor on the ranch.

Greater sophistication is possible. Groups of processors could be dedicated to particular aspects of the software trigger that do not require the full event data. The data not needed for these trigger decisions could remain on the detector (in appropriately larger buffers) until the software trigger is satisfied. In another variation, the network that unites the processors on the ranch may itself have sufficient capability to perform the event-building function considered above in a special-purpose switch. While the data-handling challenge of the BCD is great, this is an area in which progress in industry will be very significant in the next decade, and we are extremely optimistic that the needed solutions will emerge.

## 4 Detector Description

### 4.1 Silicon Vertex Detector

#### 4.1.1 Overview

The vertex detector system provides precise measurement of charged tracks to allow for the identification and measurement of secondary vertices from  $B$ -particle decay. In addition, this system provides substantial track pattern recognition as a stand-alone system as well as in conjunction with the straw tube tracker. Finally, the vertex system can provide a fast (level 1) trigger based on a secondary vertex signature.

A primary requirement in this experiment is to identify bottom and charm decay vertices that are distinct from the primary interaction point and to measure the distance between

these vertices,  $S$ , which is given by

$$S = \gamma\beta c\tau$$

where  $\tau$  is the rest-frame lifetime of the bottom or charm particle. A design 'rule of thumb' is that the detector plane closest to the decay point must have a resolution much smaller than  $c\tau$ , about 300  $\mu\text{m}$ . This condition is easily met by silicon strip and pixel detectors that have detection elements with the smaller dimension in the range 25 to 50  $\mu\text{m}$ . Such detectors provide spatial resolution of 5  $\mu\text{m}$ .

Since the decaying particles may travel in any direction within the  $4\pi$  solid angle, the silicon tracking must be capable of 3-dimensional measurement.

Three-dimensional tracking requires 3 independent views. This is a standard technique in high-energy spectrometers and requires low occupancy. Tracking can start in the nonbend view. At high rapidity, the silicon tracking provides many planes and is closely analogous to fixed-target experiments.

#### 4.1.2 Geometrical Layout

The particles from  $B$ -decay emerge over a large range of polar angles as shown in Fig. 9. To accommodate this range detectors must be placed both parallel and perpendicular to the beam line. The geometrical layout of silicon detector planes is shown in Figure 10. The overall hexagonal structure is a practical approximation to the ideal of concentric cylindrical shells to measure tracks at large polar angles. The length along the beam line of the shell structure is 28 cm. This length was chosen to cover the longitudinal extent of the luminous region of collisions which has a  $\sigma$  of 7 cm. The innermost shell is located just outside the 2.54-cm-diameter beam pipe for a variety of reasons described in the next section. In order to measure small-angle tracks produced anywhere in the luminous region, the hexagonal shells, or 'barrels,' are filled with hexagonal-shaped disks normal to the beams. The overall barrel and disk structure is built from smaller modules which are 5 cm in length along the beams. Each central module contains three concentric barrel layers and two disks. To provide a good tracking capability at low rapidity, we may increase the number of barrel planes from 3 to 5 layers to allow for three (stereo) views. On either side of the central stations are forward stations which only have disks. These stations are spaced nonuniformly along the beam such that a track in any rapidity region passes through at least three disks.

#### 4.1.3 Beam-to-Detector Distance

The measurement accuracy of the vertex detector is degraded by multiple Coulomb scattering in the detector itself. This effect is illustrated by considering the effect of the first silicon layer, which induces a r.m.s. error ( $\sigma$ ) on the impact parameter of a track due to multiple scattering given by

$$\sigma = \frac{0.015R_t}{P_t} \sqrt{\frac{X}{X_0}},$$

where  $R_t$  is the radial distance from the beam line to the detector,  $P_t$  is the track momentum [GeV/ $c$ ] and  $X/X_0$  is the fractional radiation length of the detector material. The error is minimized when  $R_t$  is minimum. However, there are a number of practical limitations to  $R_t$  for the first plane.

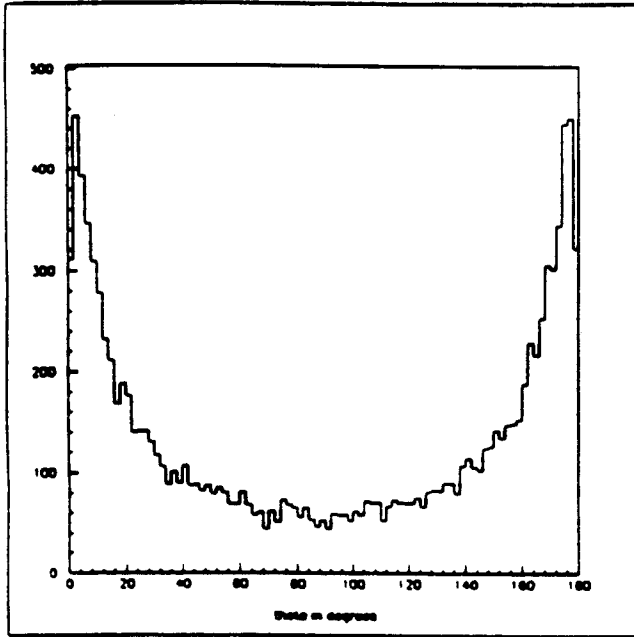


Figure 9: Distribution in polar angle for particles from  $B$ -decay.

The transverse size of the accelerator bunches is largest at injection (2 TeV), when a stay-clear diameter of 2.54 cm is necessary. At the operating energy of 20 TeV, the  $1\text{-}\sigma$  bunch radius will be  $20\ \mu\text{m}$ . This changing bunch radius could be accommodated, in principle, by a retractable vertex detector. However, there are other practical considerations. Radiation damage, which is discussed in detail below, limits the innermost detector radius to about 1.25 cm. A beam pipe at this radius will solve a number of practical problems. The beam pipe will shield the silicon detectors from the electromagnetic pulse from the bunches and maintain the accelerator vacuum. A beryllium pipe with a wall thickness of  $400\ \mu\text{m}$  will be stable at 1 atmosphere and will provide good RF shielding.

The impact-parameter resolution can now be estimated by the formula above. For a radius of 1.5 cm and for  $P_t = 1\ \text{GeV}/c$  (a typical value for a  $B$ -decay product),  $\sigma = 12\ \mu\text{m}$ . The spatial resolution of a two-track vertex from  $B$ -decay depends on the impact-parameter resolution of the two tracks and the opening angle of the decay. A detailed Monte Carlo simulation (employing ISAJET and GEANT) shows that for the decay  $B^0 \rightarrow \pi^+\pi^-$ , the most probable error on the vertex is  $25\ \mu\text{m}$  while the mean error is  $40\ \mu\text{m}$ . For detector planes with a resolution of  $5\ \mu\text{m}$ , the vertex error is dominated by multiple scattering. This scattering becomes more severe with increasing rapidity because the tracks cross the beam pipe at a grazing angle. The path length in the beam pipe wall is  $400\ \mu\text{m}/\sin\theta$ . The impact resolution, taking this into account, is shown in Table 12 for  $|\eta| < 5$ ,  $P_t = 1\ \text{GeV}/c$  and  $R_t = 1.5\ \text{cm}$ .

Above  $|\eta| = 3$  the vertex resolution is dominated by the multiple scattering in the beam pipe rather than that in the innermost silicon detector. The worsened resolution may be avoided to some extent by use of a conical (or 'flared') beampipe as shown in Fig. 8. This



BCD SILICON VERTEX DETECTOR

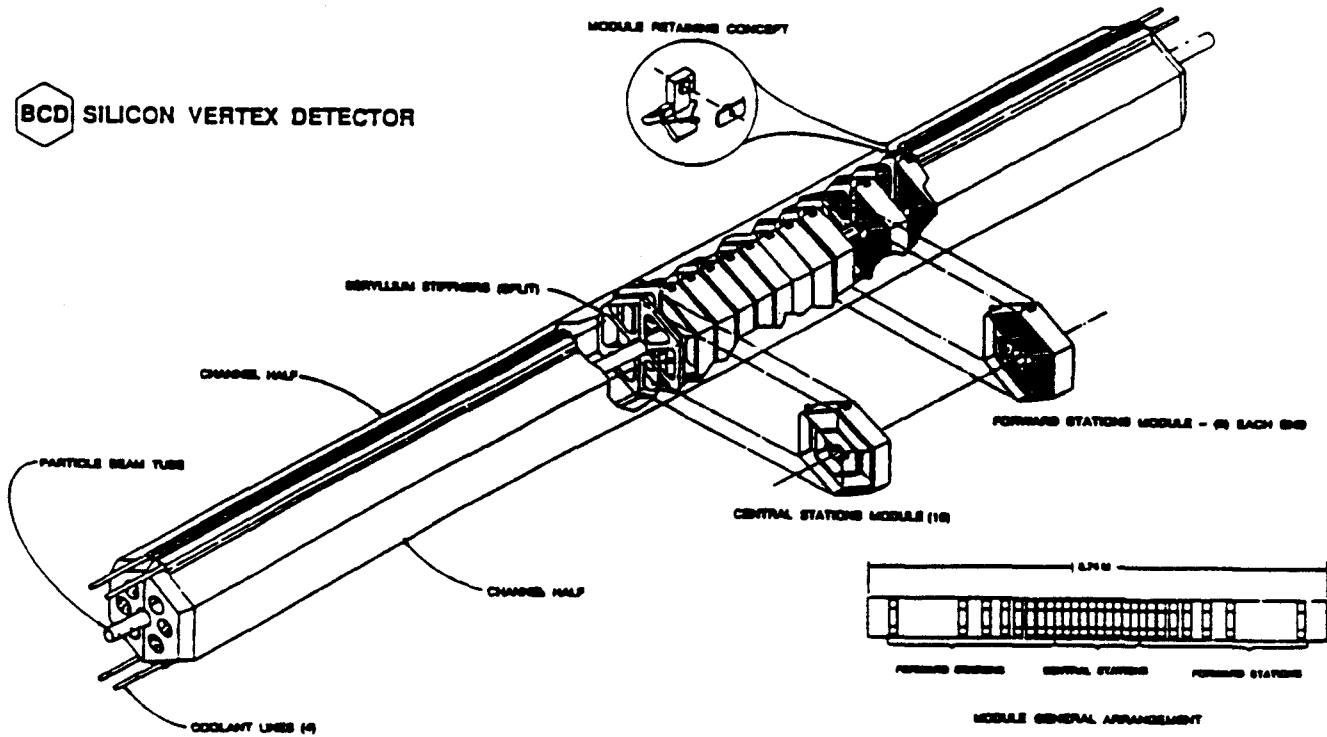


Figure 10: Arrangement of silicon wafers for micro-vertex detection of  $B$ -decays. Wafers are oriented both perpendicular and parallel to the beam. The outer barrel radius is about 10 cm.

Table 12: Contribution to impact-parameter resolution of a 1-GeV/ $c$  track from multiple Coulomb scattering in a cylindrical beam pipe. A conical beam pipe may help improve the resolution at large  $|\eta|$ .

$\eta$	$\theta$ (deg.)	$X/X_0$	$\sigma$ ( $\mu\text{m}$ )
0	90.	.0011	5
1	40.4	.0017	6
2	15.4	.0041	9
3	5.7	.0111	15
4	2.1	.031	25
5	0.77	.084	41

arrangement will be studied in the future with Monte Carlo simulations.

#### 4.1.4 Detector Segmentation

The detector planes in both the forward and central stations are silicon *p-i-n* diode arrays with both the anode and cathode segmented, so-called 'double-sided' detectors.<sup>3</sup> In the barrel layers the segments are strips oriented either along the beams or in the orthogonal direction. In the disks, strips are oriented at three azimuthal angles, 0, 120, and 240°, to provide stereo tracking views. The addition of two more barrel layers is under consideration to provide better pattern recognition for large angle tracks.

The detectors in the central stations will encounter particles at all angles of incidence to the detector plane. However, the detectors need be sensitive only to angles of incidence up to about 60° from the normal.

To achieve the desired coordinate resolution of 5  $\mu\text{m}$  the strip width is chosen to be 50  $\mu\text{m}$ . The pulse height information from all the strips in a cluster will be used to determine the mean position. In the forward stations where nearly all the particles are normal to the detector plane we will use the standard scheme employing a strip pitch of 25  $\mu\text{m}$  but with the readout pitch still 50  $\mu\text{m}$ . Capacitive charge division between the strips spreads out the signal over more than one readout strip.

The strip length is determined by considerations of occupancy. The track density [ $\text{cm}^{-2}$ ] in a single event is, on average, given by  $1.2/R_t^2$  where  $R_t$  is the radial distance [cm] to the detector plane. A Monte Carlo simulation was used to study the probability that different tracks in the event deposit ionization charge in the same strip. As an example, the confusion probability *vs.* strip length is shown in Fig. 11 for the  $\phi$ -measuring strips in the inner barrel. Strip lengths were chosen so that this probability is less than 0.005. These lengths are given in Table 13. The areas of the *p-i-n* detector elements vary from 50  $\mu\text{m}$  by 0.25 cm in the inner barrel to 50  $\mu\text{m}$  by 3 cm in the outer barrel.

Table 13: Length of *p-i-n* detection elements in different parts of the vertex detector. All elements are rectangular with the other dimension 50  $\mu\text{m}$ .

Layer	Inner	Middle	Outer
Barrel- <i>z</i>	.25	.50	1.5
Barrel- $\phi$	.50	1.0	3.0
Disk	1.15	NA	2.2

The scheme of segmentation described above gives a total strip count of 3.5 million, of which 1.6 million are in the barrel layers. Two additional outer barrel layers would add 0.7

<sup>3</sup>Members of the BCD Collaboration are also involved in R&D projects directed towards possible pixel vertex detectors. <sup>[26, 27]</sup>

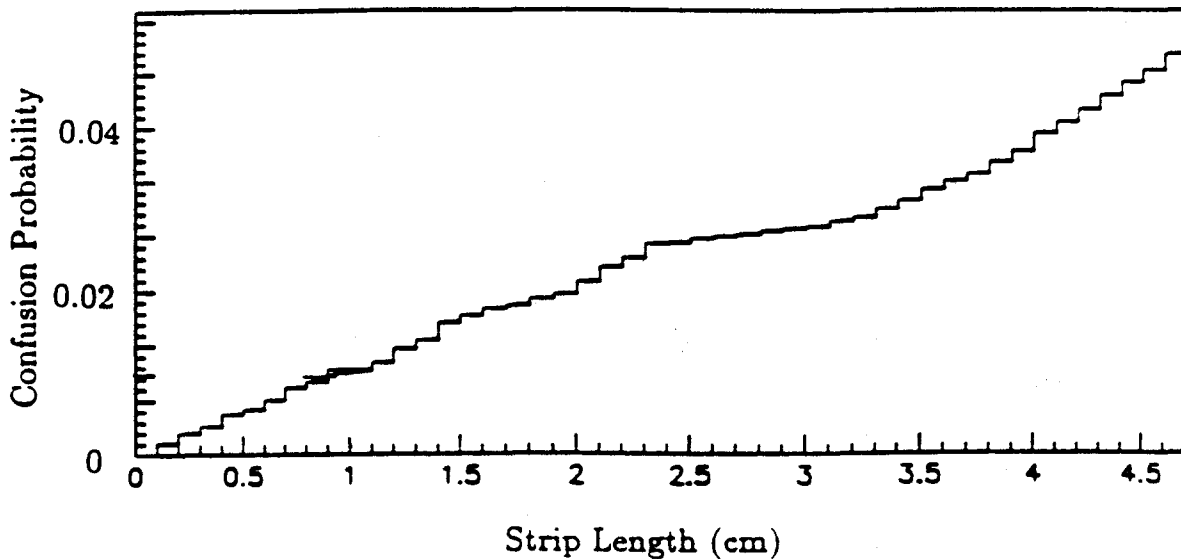


Figure 11: Monte Carlo simulation of confusion probability *vs.* strip length for the inner barrel. The strips are oriented parallel to the beam line.

million strips.

The density of tracks through the detectors is best illustrated by a simulated 40-TeV  $B\text{-}\bar{B}$  event shown in Fig. 12. Note the low track density through the vertex-detector planes. A large number of the tracks that do not originate from the  $B$  decays are outside the rapidity coverage of the vertex detector. These small angle tracks do not pass through the silicon planes and hence do not cause any pattern-recognition problems.

#### 4.1.5 Silicon $p\text{-}i\text{-}n$ Detectors

Silicon  $p\text{-}i\text{-}n$  detectors have become standard apparatus in high-energy-physics experiments. The diode structure is best implemented by ion-implantation on a wafer with typical thickness of 300  $\mu\text{m}$ . The detection-element area can be made any size that will fit on a 10-cm-diameter, high-resistivity ( $\sim 5000$  ohm-cm) wafer. The smallest dimension is limited by the line width of the lithographic process, usually about 1  $\mu\text{m}$ . Commercial manufacturers that have produced devices for high-energy-physics experiments are Canberra (Belgium), the Center for Industrial Research<sup>[28]</sup> (Norway), Enertec/Schumberger (France), Hamamatsu (Japan), Messerschmidt Bolkow Bohm<sup>[29]</sup> (Germany) and Micron Semiconductor (UK). There are no commercial U.S. manufacturers, a situation that should be remedied and is discussed in the R&D section.

$p\text{-}i\text{-}n$  diodes have been made with both  $p$  and  $n$  sides segmented to provide strip-coordinate readout in two independent directions. Since the same charge deposition will be sensed on either side of the wafer, the two coordinates can be linked by matching the pulse heights. Because the hit confusion probability is less than 0.005, most of the time there will be only one possible pair of strips on opposite sides of the wafer through which

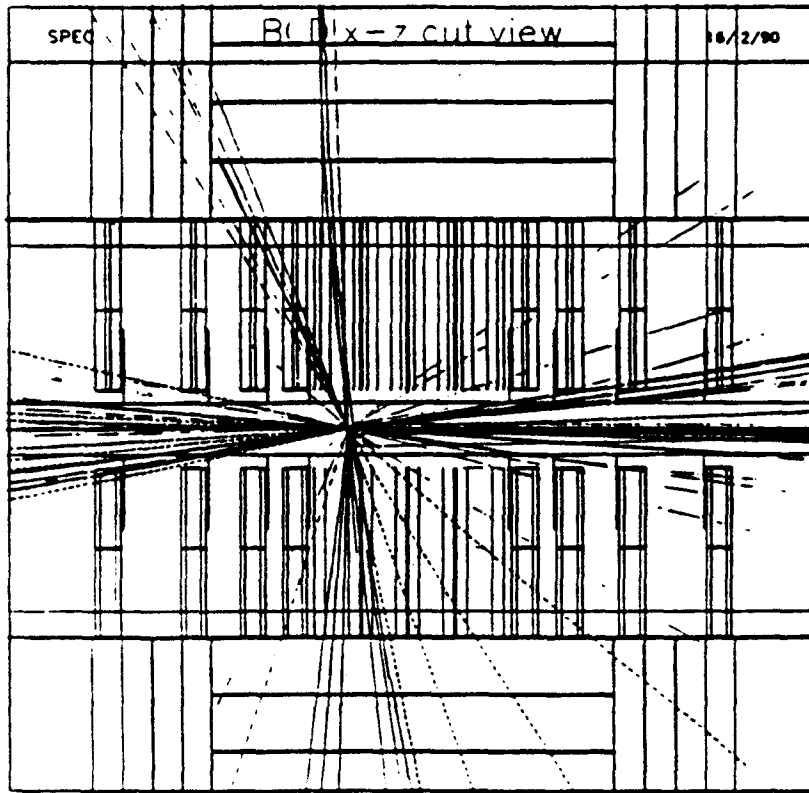


Figure 12: Monte Carlo simulation of a 40-TeV  $B$  event in the vertex detector. The scale along the beam is compressed three times relative to the transverse scale.

the same particle could have passed. Thus, the detector wafers nearly always give linked two-dimensional coordinate information.

To prevent the diode leakage current from flowing into the preamplifiers and saturating the dynamic range, capacitors can be integrated into the diode structure. This technique is especially important to minimize the effects of radiation-induced leakage currents.

When a minimum-ionizing particle traverses the silicon at normal incidence a signal of 24000 electron-hole pairs is produced in a 300- $\mu\text{m}$ -thick wafer. However, tracks at large angles of incidence may traverse not much more than 50  $\mu\text{m}$  of silicon as determined by the strip pitch. Thus, the readout electronics must have a noise figure much less than 4000 electrons.

The use of thinner wafers has been considered to reduce multiple scattering and pair conversion. Technically it is possible to thin free-standing wafers to as little as 150  $\mu\text{m}$ , although breakage in handling is a concern. Wafers with external support from the readout chip may be thinned to any desired thickness. However, since the signal-to-noise ratio is proportional to wafer thickness while the multiple-scattering contribution goes only with the square-root, it is unlikely that thinned detectors will result in an overall improvement in detector resolution.

#### 4.1.6 Readout Electronics

A number of VLSI readout chips for  $p$ - $i$ - $n$  diode arrays have been used in high-energy-physics experiments. These include the CAMEX<sup>[31, 32]</sup> (Aleph/LEP), Microplex<sup>[33, 34]</sup> (MARKII/SLC), MX<sup>[35]</sup> (Delphi/LEP), and SVX<sup>[36]</sup> (CDF/FNAL). These chips have demonstrated key features that will be required by this experiment as well: noise < 1000 electrons, power < 3 mW/channel, sparsification and multiplexed readout. A high density of readout channels has been implemented on both commercial CCD photodetectors<sup>[37]</sup> and infrared detectors<sup>[38]</sup> which have 256<sup>2</sup> elements per cm<sup>2</sup>.

This experiment will require readout chips with some features beyond what has been so far achieved: preamp shaping time < 50 ns, noise less than 800 electrons, on-chip analog-to-digital conversion of detector pulse heights, digital buffering to smooth the readout flow, suppression of large clusters due to tracks at angles of incidence greater than 60°, and radiation hardness to 10 Mrad. Research is underway to address some of these problems and additional research is proposed here in a later section.

A number of techniques are being evaluated to connect the  $p$ - $i$ - $n$  diode array to the readout chip. These include wire bonding, tab bonding and indium bump bonding. Another approach is to integrate the detector and readout on the same substrate, thereby eliminating the need for a mechanical interconnection. Research in this area is active at LBL<sup>[39]</sup> and Stanford.<sup>[40]</sup>

#### 4.1.7 Radiation Damage

Radiation damage may result from both charged and neutral particles. Damage from charged particles is primarily due to minimum-ionizing particles that penetrate the bulk. These particles originate directly from the 40-TeV interactions. Low-energy charged particles, even though they are heavily ionizing, damage only the surface, which does not cause as large an increase in leakage current as bulk damage. This is true for AC- as well as DC-coupled detectors.<sup>[41]</sup>

The charged-particle flux is primarily due to direct production from the 40-TeV interactions. This flux is given by,

$$\phi = \frac{1.2 \times 10^7}{R_t^2},$$

where the flux  $\phi$  is in particles/cm<sup>2</sup>/s,  $R_t$  is in cm, and for an accelerator luminosity of 10<sup>32</sup> cm<sup>-2</sup>sec<sup>-1</sup>. Expressed as an accumulated radiation dose over a 10<sup>7</sup> second year,

$$\Phi = \frac{3 \text{ Mrad}}{R_t^2}.$$

The neutron flux is produced in showers in the calorimeter and magnet. This flux is uniform throughout the detector cavity and is expected to be 2.4 × 10<sup>11</sup> particles/cm<sup>2</sup> integrated over 10<sup>7</sup> sec. The spectrum of neutron energy,<sup>[42]</sup>  $E dN/dE$ , is Gaussian in  $\ln E$  with a peak at 1 MeV and  $\sigma$  of 8 MeV. Thus, most of the energy is carried by 1-MeV neutrons. As with charged particles, neutrons which penetrate the bulk do the most damage.

The radiation damage to  $p$ - $i$ - $n$  diodes can be characterized by the increase in leakage current density,  $\Delta J$  [Amperes/cm<sup>2</sup>], due to a time-integrated radiation flux  $\Phi$  [particles/cm<sup>2</sup>].

It has been found experimentally that  $\Delta J$  is proportional to  $\Phi$ :

$$\Delta J = \alpha \Phi$$

where the constant of proportionality,  $\alpha$  [A/cm], is called the current-damage constant. For minimum-ionizing particles, a typical value measured for  $\alpha$  is  $3 \times 10^{-17}$  A/cm. The proportional relation above has been verified for  $\Phi$  up to  $4 \times 10^{14}$  MIPS/cm<sup>2</sup> (10 Mrad). The leakage current constant for neutrons<sup>[43]</sup> increases with energy in the range 1 MeV to 14 MeV. At the most probable energy of 1 MeV,  $\alpha = 7 \times 10^{-17}$  A/cm measured for an integrated flux of  $10^{14}$  cm<sup>-2</sup>. Damage constants are a strong function of temperature and are usually quoted at 20°C. The leakage current decreases by a factor of 10 as the temperature decreases to 0°C. Thus, operation of the detectors below room temperature is an attractive option.

We can now estimate the induced leakage current in the *p-i-n* diode detector elements closest to the beams, those at a radius of 1.5 cm. After  $10^7$  seconds of accelerator operation at a luminosity of  $10^{32}$  cm<sup>-2</sup>sec<sup>-1</sup>, the integrated flux of charged particles will be  $0.5 \times 10^{14}$  cm<sup>-2</sup>. This is much larger than the integrated neutron flux of only  $2.4 \times 10^{11}$  cm<sup>-2</sup>. Thus, the radiation damage is dominated by the charged flux. For a 300- $\mu$ m-thick substrate and a detector element size of 50  $\mu$ m by 5 mm the increase in leakage current is 120 nA. For a preamp shaping time of 30 ns, this leakage is equivalent to a noise of 150 electrons r.m.s., much smaller than the typical preamp noise of 600 electrons. Thus, *even at room temperature, the radiation induced leakage current is not a limiting problem.* Indeed, operation at higher luminosity at below room temperature can be considered. The limitations from radiation damage are more likely to be due to the electronics.

Much less is known about the radiation tolerance of readout chips. The existing devices have not been fabricated in a radiation-hard process and show severe performance degradation after irradiations in the range 10 to 100 krad, for different types of chips. Fabrication technologies have been developed for the military that allow digital electronic circuits to operate after 10 Mrad. These processes generally rely on two principles. The first is the use of thin oxides in MOS circuits or no oxides as with bipolar transistors. Oxides are bad because they trap charge ionized by the radiation. Oxide layers as thin as 125 Å have been fabricated. This is to be compared with the typical thickness of 400 Å in conventional fabrications. The second rad-hard principle is the isolation of the thin layer containing the circuit elements from the underlying substrate where ionizing radiation creates unwanted free charges. Technologies based on this principle are silicon-on-sapphire (SOS), silicon-on-insulator (SOI), and dielectric isolation (DI).

While rad-hard digital circuitry is an established technology, little is known on the performance of radiation-hardened, low-noise analog circuits. Studies have been made to characterize the threshold shift of an FET<sup>[44]</sup> and the reduction in  $\beta$  of bipolar transistors<sup>[45, 46]</sup> due to radiation damage. Recently, a number of analog circuits for high energy physics applications have been submitted for fabrication in a radiation hard process at UTMC. Additional work needed is discussed in the section on R&D.

#### 4.1.8 Mechanical and Thermal Stability

The relative alignment of the silicon detectors must be maintained to better than the resolution of 5  $\mu$ m. It is not necessary to place the detectors absolutely to 5  $\mu$ m since alignment

constants can be found from data. However, the relative position of the detectors must not change after installation. The areas of concern for maintaining the alignment include thermal expansion, and vibration due to the forced air cooling. Tests at Fermilab<sup>[47]</sup> on a model vertex structure show that the required stability can be maintained for heat loads up to at least 0.1 Watts/cm<sup>2</sup> using forced-air cooling. We anticipate that forced-air cooling will work for heat loads up to 1 W/cm<sup>2</sup>. It is desirable to have the option of operating the *p-i-n* diodes below room temperature to limit leakage current, which halves for each 8°C drop in temperature. This option will allow for operation at higher radiation levels.

An engineering study of a robotic assembly procedure for the BCD vertex detector has also been performed.<sup>[48]</sup>

#### 4.1.9 Data Transmission

Minimum-bias events will produce an average data rate of 420 Gigabits per second, based on Monte Carlo simulations. This rate can be continuously streamed out over 420 optical fibers using commercially available Gallium Arsenide multiplexers<sup>[49]</sup> and semiconductor laser diodes. The power dissipation is 2 Watts per fiber including both the multiplexer and laser diode. While the currently available technology is limited to 2 Gbits/sec, laser diodes have already been operated at 10 Gbits/sec<sup>[50, 51]</sup> although the multiplexers have not yet been developed for this rate. In a few years we expect that 10 Gbits/sec will be commercially available and hence the vertex readout will work at luminosities approaching 10<sup>33</sup> cm<sup>-2</sup>sec<sup>-1</sup>.

#### 4.1.10 Data Processing

The silicon data will be processed a few meters away from the vertex detector itself. Even here, space and power consumption must be limited. Processors are now available that exploit wafer-scale integration and wafer-to-wafer interconnection to achieve impressive speed at low power. The Hughes 3D computer<sup>[52]</sup> employs wafers with an array of 128 × 128 processors giving a combined performance of 390 Mflops for 32-bit data words. Up to 15 wafers can be vertically interconnected in a volume less than 330 cm<sup>3</sup> and with a power dissipation less than 100 watts.

This processing power could be used to manipulate the silicon data in both simple and complex ways. The simplest function is to buffer the data until an external trigger arrives based on other parts of the experiment. The silicon data itself can be used in simple or complex ways. The *z*-coordinate of an interaction can be found quickly by averaging the coordinates of chips which have any hits (Fast OR). Events can be rejected that don't have a sensible topology of hit chips. Full use of the silicon information can be used to form a trigger based on the existence of a secondary vertex. This trigger will require a track-finding algorithm that takes advantage of the straight line tracks in the non-bend view. The vertexing algorithm can take advantage of the small transverse extent of the beams. Silicon tracking and fast vertex algorithms are under development.

#### 4.1.11 Simulations of Vertex-Detector Performance

We have performed several simulations of the performance of the vertex detector using ISAJET and GEANT. The first phase of computer studies<sup>[53]</sup> examined the efficiency of

various silicon vertex detector configurations for identifying the  $B$ -decay vertex, assuming perfect pattern recognition. We found that about 45% of  $B$  decays to all-charged final states could be reconstructed. These studies included the effects of multiple scattering in the beam pipe and silicon detectors as well as the spatial resolution of the silicon detectors.

The next series of studies addressed the question of whether tracks can be properly associated with the vertices from which they emanate. The events were generated using ISAJET and the detector simulated using GEANT. The primary vertex had to be found first, and the pool of tracks failing to be associated with the primary were searched for secondary-vertex candidates to see how often real non- $B$  or false secondary vertices simulated a rare  $B$  decay. The decay  $B \rightarrow \pi^+\pi^-$  was studied because it is the most difficult in terms of combinatoric background, and because it is potentially interesting for having a large CP-violating decay asymmetry.

A number of conclusions have emerged from this investigation (also see Figure 13).

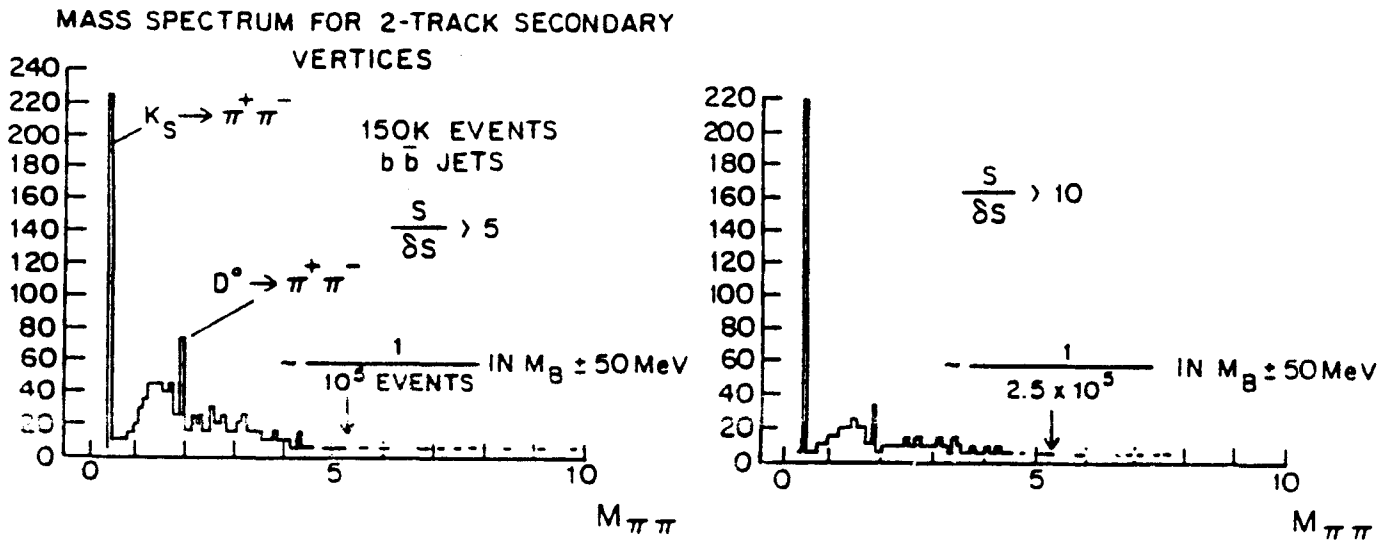


Figure 13: Effective mass of non- $B$  2-prong secondary vertices.

- The vertex resolution has a most probable value of  $25 \mu\text{m}$  in space, with a mean of  $40 \mu\text{m}$ ; a tail of poor resolution deserves further study. With a  $4\pi$  detector geometry, the vertex resolution in  $z$  (the beam direction) is only slightly different from that in  $x$  or  $y$ .
- Only tracks with transverse momentum greater than about  $300 \text{ MeV}/c$  will be useful in vertex finding (as known from fixed-target experiments).
- Secondary vertices more than  $100 \mu\text{m}$  distant from the primary vertex will be reconstructed with good efficiency.



- The greatest source of fake  $B$  decays is events containing  $B$ 's that are misanalyzed: a track from a  $B$  decay is mistakenly grouped with a track poorly fit to the primary vertex, yielding a high apparent mass for the fake secondary vertex.
- In the present study, about 1  $B$  decay in  $10^6$  yields a false  $\pi^+\pi^-$  secondary vertex with mass within a 100-MeV window about the  $B$  mass. The latter is a  $\pm 2\sigma$  cut based on the estimated momentum resolution of the tracking system.
- The efficiency for finding  $B \rightarrow \pi^+\pi^-$  decays with the present vertex algorithms is about 20%. The average separation between the primary and secondary vertices is 18 times the vertex spatial resolution.
- Without explicitly simulating other decay modes, we infer that they will all have better signal-to-noise, due to particle identification, or to the reduced probability of falsely associating more than two tracks to a secondary vertex.
- Simulation of events with two primary vertices (distributed in space according to the expected size of the collision region) shows that if the tracking pattern recognition remains of high quality, the vertex algorithms will continue to separate the vertices to the above accuracy.

The silicon vertex simulation has now been expanded to include various physics processes besides multiple scattering. It includes the exact path length calculation in the silicon active region, energy-loss fluctuation in the silicon, charge correlation between one side of the wafer and the other one, charge diffusion between neighbouring strips, detection inefficiency, sparse readout based on charge division, and electronic noise at the preamplification level.

## 4.2 Straw-Tube Tracking System

The charged-particle tracking that was begun in the silicon vertex detector is extended in the straw-tube tracking system. Here the tracks are sampled over sufficient distance in (or around) a magnetic field to yield a good momentum measurement. We base our design of the straw-tube system on the work of an Ohio State group,<sup>[54]</sup> and have begun an R&D program to explore the issues of large-scale application for the BCD.<sup>[55, 56]</sup>

### 4.2.1 Mechanical Design

The Central tracking system occupies a volume  $180 \times 180 \text{ cm}^2$  in cross section and 6 m along the beams, as shown in Fig. 7. This volume includes the silicon vertex detector also, which occupies a cylinder of 10-cm radius about the beams. The Central tracking system is long enough to perform tracking for the Intermediate detector, which has no separate tracking system. In the Forward detector an additional tracking system is needed, which consists of three stations of tracking chambers surrounding the Forward analysis magnet.

Straw tubes are a low-mass variation on the basic cylindrical proportional counter, and are operated as drift chambers to obtain excellent spatial resolution. The straw tubes will be about 5 mm in diameter, up to 2 m long, and aligned vertically along the magnetic field, or at

$\pm 200$  mrad to the vertical to obtain small-angle stereo measurements. Each straw is a two-ply laminate of an inner carbon-loaded polycarbonate film about  $14\text{-}\mu\text{m}$  thick surrounded by a layer of  $12.5\text{-}\mu\text{m}$ -thick Mylar. The polycarbonate film is aluminized on its inner surface to form the cathode. The anode wire is  $20\text{-}\mu\text{m}$ -diameter gold-plated tungsten. Such a tube has about 0.0004 effective radiation lengths. A likely chamber gas is  $\text{CF}_4$ /Isobutane which has a fast, saturated drift velocity of about  $100\text{ }\mu\text{m}/\text{ns}$ , low longitudinal diffusion, a primary-ionization density of about 40 clusters/cm, and yields chamber lifetimes well in excess of 1 C/cm. With care in construction and alignment, the straw-tube chambers should achieve a spatial resolution of  $50\text{-}60\text{ }\mu\text{m}$  per tube.

The need for measurement of two coordinates complicates the mechanical design of the straw-tube system. Alternatives such as current-division or cathode-pad readout, or use of scintillating fibers to obtain the second coordinate are not (at present) as appealing as the use of small-angle stereo measurements. The latter method presents problems at the boundaries of the chamber volume: a tube at angle  $200$  mrad has a  $36\text{-cm}$  offset over a length of  $180\text{ cm}$ . We wish to read out the straws only at the top and bottom of the detector to avoid accumulation of mass inside the tracking volume. The consequence is some loss of acceptance for the tilted coordinates at the chamber edges.

A layout for the Central tracking system which avoids some of these difficulties is shown in Fig. 14. The chambers close the interaction point are on circular arcs, which avoids the edge effects if the circles are complete. A drawback is that the tilted tubes lie on hyperboloids of revolution, which cannot be made out of cylindrical tubes without cracks between adjacent tubes (or tube-modules) that grow larger away from the midplane. In the more forward part of the Central detector the available volume flares outwards. Here the tilted planes can extend into the flare, permitting full coverage of the  $180 \times 180\text{ cm}^2$  cross section of the tracking volume. An alternative scheme based entirely on rectangular arrangements of the straw-tubes is shown in Fig. 17.

The 'superlayers' of detector elements shown in Fig. 14 will be built out of modules 8 straws thick and  $8\text{-}64$  straws wide. The straws in a module will be glued together to provide greater structural rigidity. The arrangement of straws within a module will be wedge-shaped to minimize the problem of cracks between adjacent modules.

At the ends of each module are structures that serve to maintain the tension and alignment of the anode wires, direct the flow of gas in and out of the straw tubes, and carry the electrical signal of the detectors to the preamplifiers, which are also to be mounted on these endcaps. A design to satisfy all these functions is quite intricate and will lead to a structure of at least 2% of a radiation length. Fig. 15 shows a preliminary design for the endcaps.

#### 4.2.2 Electronics

The straw tracking chamber will require high-accuracy ( $< 0.5\text{ ns}$ ), low-deadtime, low-noise ( $< 2000$  electrons), low-power ( $< 20\text{ mW}$ ), radiation-tolerant electronics coupled directly into the high-rate data-acquisition system. The electronics front-end system is based directly upon the design developed by the SSC Front-End Electronic Subsystem effort<sup>[57]</sup> and uses a bipolar preamplifier, shaping amplifier ( $t_{\text{measure}} \sim 5\text{-}10\text{ ns}$ ), and discriminator followed by a CMOS time-to-voltage converter (TVC), analog-storage array, and readout ADC.<sup>[58]</sup> This system is designed to handle individual wire rates of more than  $5\text{ MHz}$  at the input and up

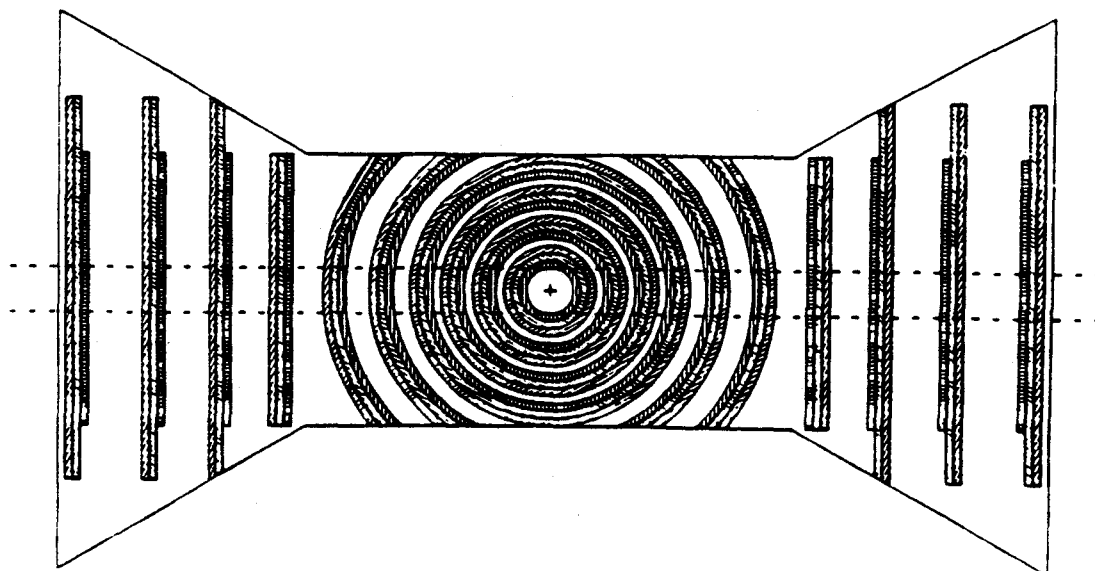


Figure 14: A possible layout of the Central straw-tube tracker, shown in plan view. The available volume is 6-m long and  $180 \times 180 \text{ cm}^2$  in cross section, with flares at  $33^\circ$  to the beams. The cylindrical arrangement of the chambers in the center avoids edge effects in the small-angle stereo layers. In the forward region the tilted planes will extend into the flare to maintain full coverage over the 180-cm width. The silicon vertex detector occupies a cylinder of radius 15 cm about the beams inside the tracking volume.

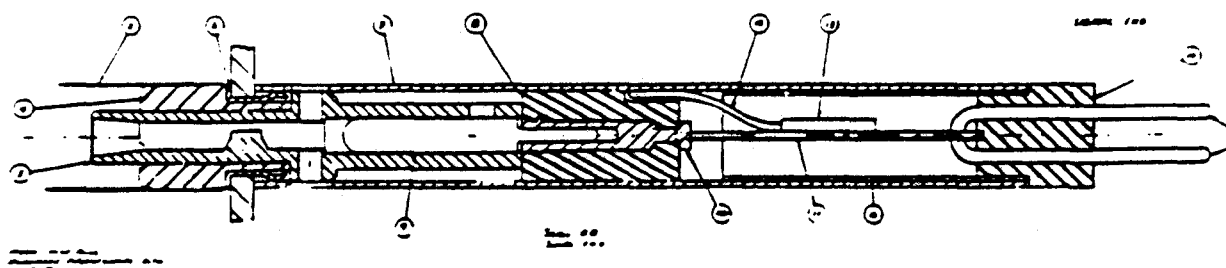


Figure 15: Possible scenario for a straw-tube end plug: 2: the straw tube; 4: aluminum insert; 5: Utem feedthrough; 6: collar spring; 7: metallic sleeve; 8: plastic socket; 9: taper pin; 10: pin socket; 11: G-10 board with anode lead on bottom; 12: cathode lead; 13: blocking capacitor; 14: plastic collar; 16: Mylar sleeve. The anode- and cathode-signal pins at the right end plug into the front-end electronics board. The vertical plate at the left is made of Macor.

to 500 kHz readout at the ADC. This readout rate corresponds to about 10% occupancy at a luminosity of about  $10^{32} \text{ cm}^{-2}\text{sec}^{-1}$  without any trigger rejection.

### 4.2.3 Momentum Resolution

We estimate the momentum resolution that will be obtained in the tracking system with the following expression;<sup>[59]</sup>

$$\left(\frac{\sigma_{P_{\perp}}}{P_{\perp}}\right)^2 = \frac{720}{n+5} \left(\frac{\sigma_{s_{\perp}} P_{\perp}}{3 \times 10^{-4} B L^2}\right)^2 + 1.43 \left(\frac{0.015}{3 \times 10^{-4} \beta B L}\right)^2 \sum_{i=1}^n t_i (1 + (1/9) \log_{10} t_i),$$

where  $P_{\perp}$  is the momentum component perpendicular to the magnetic field (not the beam),  $\sigma_{s_{\perp}}$  is the measurement error in cm,  $B$  is the magnetic field strength in kG,  $L$  is the path length in cm over which the measurement is made,  $n$  is the number of measurements, and  $t_i$  is the thickness in radiation lengths of the material associated with measurement  $i$ . This expression is strictly valid for the case of uniform sampling along  $L$ , which is entirely within field  $B$ . The dependence of the momentum resolution on spatial resolution and momentum has the familiar form

$$\left(\frac{\sigma_{P_{\perp}}}{P_{\perp}}\right)^2 = (A\sigma_{s_{\perp}} P_{\perp})^2 + B^2.$$

We have modelled the detector performance supposing  $n = 64$  in the Central tracker, and  $n = 96$  in the Forward tracker. Field  $B$  is 10 kG in the Central tracker over its 6-m length, while we use an effective field of 4.6 kG in the Forward tracker where the field occupies only part of its 13-m length. Each straw contributes  $t_i = 0.0004$  radiation length. Fig. 16 shows the expected resolution for particles with transverse momentum (to the beams) of 2.5 GeV/c and momentum vector perpendicular to the magnetic field. The spatial resolution in a single straw was taken to be  $\sigma_{s_{\perp}} = 50 \mu\text{m}$ .

Also shown is the momentum resolution obtained in the silicon vertex detector alone, for particles with  $2.75 < \eta < 4.25$ . In this interval the momentum measurement in the silicon detector is superior to that from the straw tracking system. The silicon detector is taken to have  $\sigma_{s_{\perp}} = 5 \mu\text{m}$ , and to extend 6 m along the beams (i.e., the full length of the Central tracker).

We see that at  $P_{\perp}$  and with  $\sigma_{s_{\perp}} = 50 \mu\text{m}$  for the straws, the resolution is dominated by multiple scattering in all parts of the detector. However, if the spatial resolution deteriorates to  $100 \mu\text{m}$ , or if we consider  $P_{\perp} = 5 \text{ GeV}/c$ , the measurement error adds about 25% to  $\sigma_{P_{\perp}}/P_{\perp}$ . The momentum resolution is better than 1% at all transverse momentum less than 2.5 GeV/c, which will yield  $\sim 0.5\%$  mass resolution in the reconstruction of  $B$  decays.

### 4.2.4 Straw Tracking Simulation Study

#### Scope

The appropriate momentum scale for detecting  $B$  events, produced primarily through gluon-gluon fusion, is quite low—on the order of the  $B$  mass. The subsequent decay of the  $B$ 's will result in tracks with average  $P_{\perp}$  of approximately 1 GeV/c. Thus, the tracking has to be quite good, even to very low  $P_{\perp}$ . Studies have shown that significant loss of events occurs if

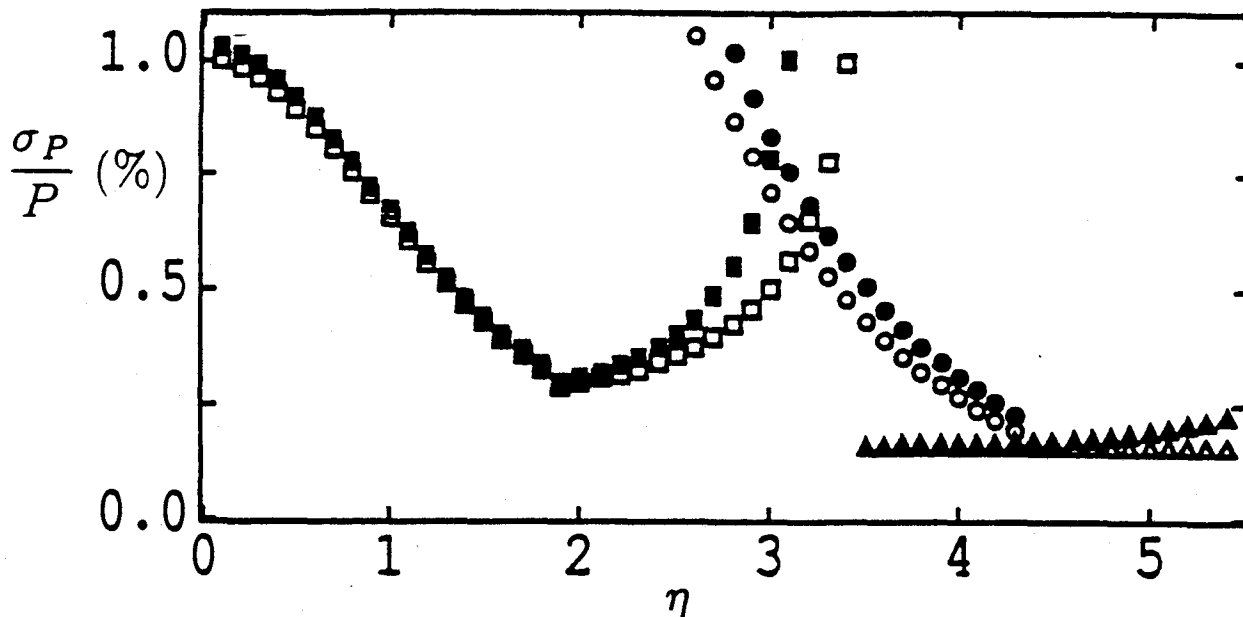


Figure 16: The momentum resolution vs. pseudorapidity  $\eta$  of the tracking system for particles with transverse momentum (to the beams) of 2.5 GeV/c and momentum vector perpendicular to the magnetic field. The spatial resolution of the straw-tube chambers is taken to be 50  $\mu\text{m}$ , and that of the silicon vertex detector is 5  $\mu\text{m}$ . The contribution of multiple scattering to the resolution is also shown, and is seen to be dominant for the given conditions.

the lower momentum cutoff for reconstructing  $B$  decay products is much above 300 MeV/c. This is certainly a challenge in a collider environment. In addition, the dipole field and spatially distributed vertices (in the beam direction) make this a more difficult problem than that commonly encountered in collider detectors using a solenoidal field, in which the tracks in the azimuthal view are circles coming from a single, well-defined beam-interaction point. Because of these challenges, the BCD has chosen to carry out its simulation to a level much more detailed than previous experiments at the proposal stage. Good tracking plays an integral part in one's ability to vertexize  $B$ -decay candidates. So far, for these studies, the initial fit roads have been taken from the given generated momentum, smeared by the expected resolution of the straw tracking system. Straw pattern recognition and tracking will soon be combined with pattern recognition in the silicon to get a more realistic estimate of  $B$ -vertexing efficiency, in that actual found tracks will be used as the starting point.

#### Overview of the Straw-Tube Simulation Strategy

The straw tracking planes are formed as superlayers of 8 individual planes of straws, all straws in a given superlayer having the same spatial orientation ( $x$ ,  $y$ ,  $u$ , or  $v$ ). Superlayers of each type can then be grouped together to aid in pattern recognition. Figure 17 shows the current geometry modelled for the straw tracking system, as viewed in the direction of the magnetic field. The beams enter from left and right. All planes in the beam direction have an  $u$ - $x$ - $v$ - $y$  multiplet. Some of the transverse planes have only an  $x$ -superlayer. Further optimization of this geometry is one of the goals of the straw simulation study.

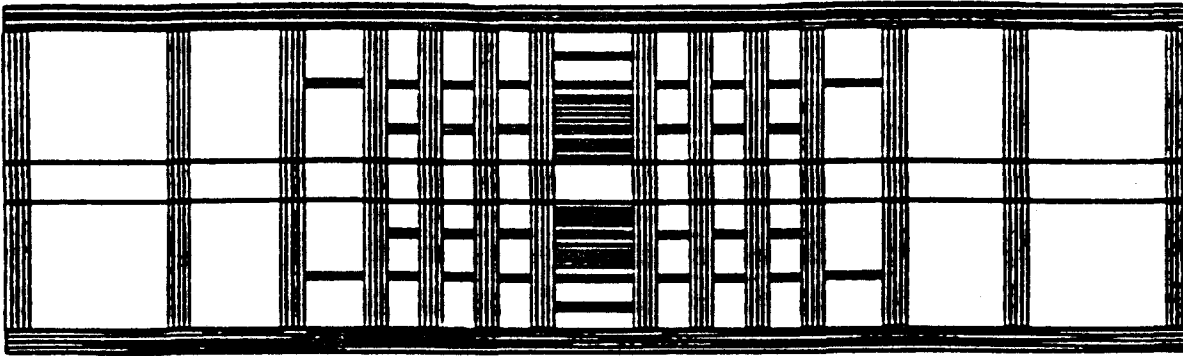


Figure 17: A view of the straw tracking system used in the computer simulation, looking along the direction of the magnetic field. This configuration is an alternative to that shown in Fig. 15.

Because of the complexity and time required to track through individual straw cells, we have chosen to separate the problem into two parts, as described in more detail below. Briefly, part one is a detailed, cell-level simulation that is intended to measure the pattern-recognition capability within a superlayer, combining hit straws (cells) into track segments called 'minivectors'. Part two is a full detector simulation which links these minivectors together, smeared by the appropriate resolution found in part one, to form tracks.

### Cell-Level Simulation

This detailed simulation models a single superlayer, consisting of an  $8 \times 40$  hexagonally close-packed array of individual straw tubes. In GEANT, these tubes are parameterized as 4-mm-diameter, 30- $\mu\text{m}$ -thick mylar cylinders, 2 meters in length. A 20- $\mu\text{m}$ -diameter tungsten wire is used for the anode. Various gases are used in the tubes. Tracks with random momentum vectors are then generated and tracked through the tubes, with their entrance and exit positions in the gas volumes being recorded. We have chosen to parameterize the physics of the straw tubes and their timing electronics via a simple Monte Carlo model, based on a similar model for drift chambers from SLAC.<sup>[90]</sup>

The model is as follows:

1. Along the track path within the gas, distributed via a Poisson distribution, are  $n$  ionization events/cm,  $n$  being different for each gas chosen. (The mean value of  $n$  is 25.5 for 1 atmosphere argon-ethane, for example.)
2. The electrons drift radially (excluding Lorentz angle effects) toward the wire in an electric field sufficiently high to saturate the drift velocity. They also diffuse radially according to a gaussian with a  $\sigma$  that is a constant times the square root of the initial radial distance from the wire. This diffusion constant is not in general accurately known for all gases.
3. At the wire, each electron is independently amplified by a factor  $A$ , which is distributed

according to

$$P(x) = (3x/2)e^{-3x/2} \quad \text{where} \quad x = A_i/(A).$$

4. The tube acts as a transmission line driven by a current source giving a voltage pulse which is, to within a constant:

$$V(T) = A_i/(T_0 + T) \quad \text{where} \quad T_0 = 1 \text{ nsec.}$$

5. The amplified signal is characterized by a rise time  $T_r$ . This is approximated by assuming the amplifier response to a step-function input is a ramp of duration  $T_r$  followed by a plateau.
6. The final signal that is fed to a discriminator is just the sum of the individual pulses delayed relative to each other by the electron arrival times at the anode. The dispersion in discriminator firing times (and thus the spatial resolution) can then be studied as a function of initial impact parameter, radial diffusion for a given gas, amplifier rise time and discriminator threshold. Preliminary results from this model show that resolutions of 50  $\mu\text{m}$  or better can be achieved. These Monte Carlo predictions will be compared to actual data to be taken this fall in a test beam at Fermilab.

In addition to predictions of the spatial resolution achievable in individual straw tubes, track-finding algorithms are now being developed to link hit cells together into minivectors within a superlayer. Two algorithms are currently being investigated. The first is a simple histogram search in angle from a given hit in an outer layer of the superlayer. The second approach is to construct the minivectors from locally related hits using a tree algorithm. This approach has worked well in analyzing jet events in the TASSO detector at PETRA.<sup>[61]</sup> Values for minivector spatial and angular resolutions as a function of particle momentum and angle of incidence to the straw superlayer planes should be available soon.

### Full Detector Simulation

The goal for this part of the simulation is to find all minivectors associated with a given track, determine the track's momentum and finally to use these determined track parameters in the vertex-determining algorithms. Pairs of hits, representing found minivectors, are recorded at the entrance and exit of each superlayer, smeared by an assumed spatial resolution of 50  $\mu\text{m}$ . At this stage of the study, no confusion from incorrectly identified minivectors is assumed. Minivectors in the outer layer of straw planes are then combined with an assumed primary-vertex position to give a starting search road. The primary-vertex position used is the true position smeared by 0.1 cm in the beam direction, a resolution that can be achieved from a simple fit to the silicon-plane data.

For simplicity, an almost completely hermetic outer layer of straw planes has been assumed. Forward and backward planes have a square beam hole of 10.6-cm half-size. Top, bottom and side chambers cover the full extent of the detector. Since less than 10% of the tracks exit via top or bottom planes, in reality these planes will probably not be built, but are included here for simplicity. In actuality, one would proceed to find tracks associated with the most outer layer of straw planes, eliminate minivectors from these tracks on more inner planes, and iterate inward toward the center of the detector. Again, for simplicity, a constant magnetic field has been assumed.

To start a fit, all pairs of  $u$ - $v$  minivectors in an outer-layer plane are searched for a match to a minivector in an  $x$ -layer plane. These triplets are matched to a  $y$ -layer minivector. Losses at this stage of pattern recognition are small. For those tracks which are within the rapidity coverage of the straw tracking system, approximately 12% have momenta too low to arrive at an outer layer; typically these tracks have momenta well below 300 MeV/ $c$ , and are not of interest. For those tracks that do reach the outer straw layers, 95% are found and correctly matched. For the outer straw layers, the  $u$ - $v$  planes have been configured as small-angle ( $15^\circ$ ) stereo planes with tubes running approximately perpendicular to the magnetic-field direction. This gives a match to the  $y$  coordinate (the magnetic-field direction) that is largely momentum independent, important in the outer planes that are used to determine the initial search road. For the inner straw layers, the small-angle  $u$ - $v$  stereo planes have been configured with tubes running approximately parallel to the magnetic field direction, for increased resolution.

A simple unweighted circle fitter is then used to predict an initial bend-plane momentum. The nonbend-plane momentum is calculated from the dip angle. For the assumed minivector spatial resolution ( $50 \mu\text{m}$ ) and primary-vertex  $z$ -position resolution ( $0.1 \text{ cm}$ ), the error on momentum for this initial fit is approximately 7%. Inner-layer planes are then searched with momentum-dependent roads for minivectors associated with each track. For planes in which more than one minivector is found within the search road, the minivector closest to the fit is retained. If a set of  $x$ - $u$ - $v$ - $y$  minivectors have been found, all minivectors must be within the roads for any of them to be accepted. After all planes have been searched, if additional minivectors have been found, the momentum fits are updated using the  $x$ -plane minivectors only, and the search procedure is iterated. The momentum error for these updated fits has been reduced to 4% for momenta greater than 300 MeV/ $c$ . An improved fitting routine that uses minivectors from all plane types is now being written which will substantially improve this error.

Figures 18-19 show a typical event in the straw tracking system. This event was generated by ISAJET, using the  $b\bar{b}$  two-jet process. Crosses on the figures represent the entrance and exit hits at the straw planes. Figure 18 displays all of the minivectors in the event, while Fig. 19 shows the found minivectors. For all tracks above 300 MeV/ $c$  that have outer-layer matches, 87% of the minivectors are found. For those tracks originating from the primary vertex, 91% of the minivectors are found. About 3% of the minivectors found for all tracks are unassociated with the track. At this stage in the simulation, these numbers are encouraging.

As the final step in our simulation we reconstructed the invariant mass of the  $B$  from tracks due to the decay  $B_s^0 \rightarrow \pi^+ \pi^-$ . The mass resolution is about  $30 \text{ MeV}/c^2$ , as shown in Fig. 20, which indicates that the reconstruction program is working about as well as can be expected given the multiple scattering in the chambers.

### Further Development

Several improvements are being implemented in the tracking pattern-recognition study:

1. Pattern recognition at the minivector level.
2. A more sophisticated fitting program.
3. Hit contention at the track level.





Figure 18: A typical SSC event from the  $b\bar{b}$  two-jet process, showing all minivectors in the straw tracking system.

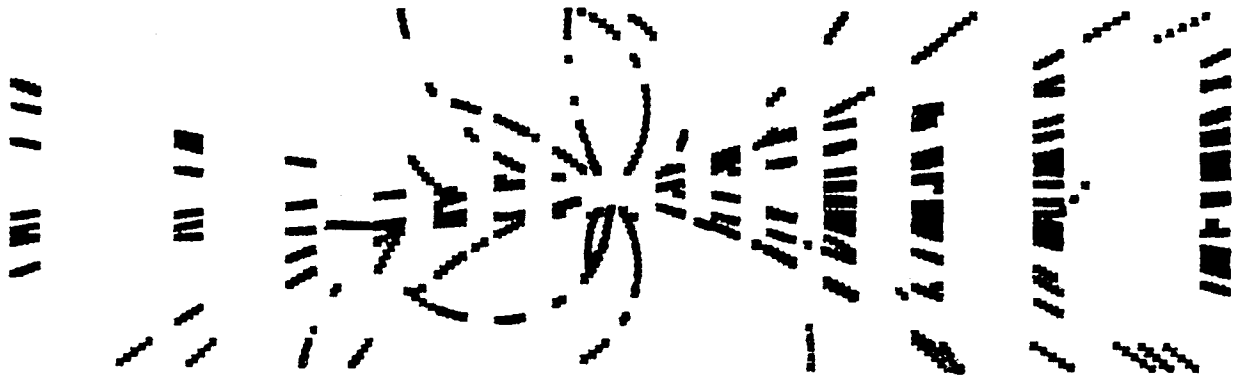


Figure 19: The same event, showing the found minivectors.

4. After the initial search, two fits can be attempted: one including the primary vertex, and one without it. The best fit of these two could then provide a new search road. This may improve hit finding on tracks which originate close to, but not at the primary vertex.
5. Found minivectors can be eliminated, and the remaining minivectors examined for tracks that do not originate close to the primary vertex.

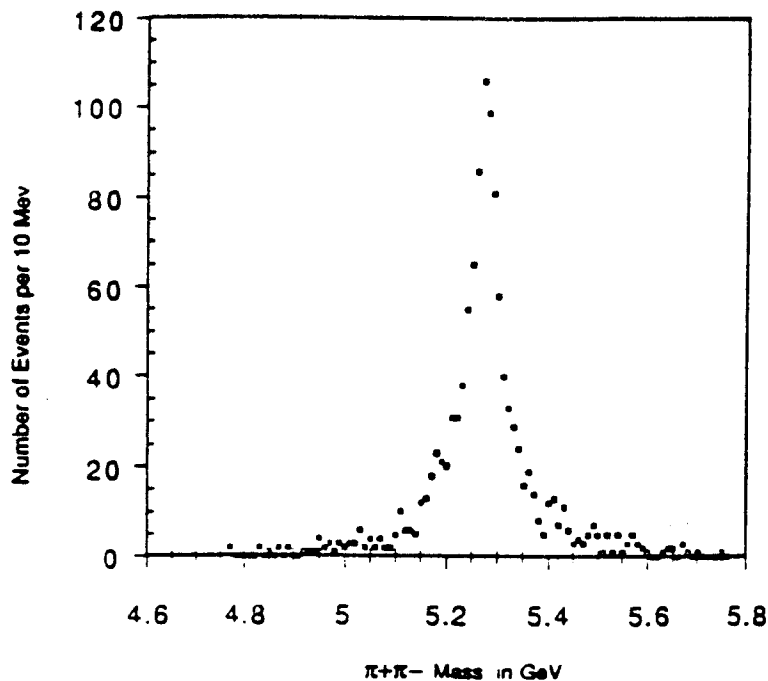


Figure 20: Simulated invariant mass reconstruction of the decay  $B^0 \rightarrow \pi^+ \pi^-$ . Multiple scattering and chamber resolution are simulated, and pattern-finding algorithms assemble the straw hits into tracks. The mass resolution achieved here is about  $30 \text{ MeV}/c^2$ .

## 4.3 Time-of-Flight System

### 4.3.1 Introduction to Hadron Identification

Some 90% of all nonleptonic decays of  $B$  mesons lead to final-state Kaons, so their identification is vital in a broad program of  $B$  physics. Because the  $B$ -decay products have relatively low momentum, a high-performance time-of-flight system in combination with a single ring-imaging Čerenkov counter can identify charged pions and Kaons at all angles.

The spectra of momenta of  $B$ -decay pions are shown in Fig. 21 for the Central, Intermediate, and Forward detector regions. Both average spectra for the 10 modes of Table 5, and spectra from  $B \rightarrow K\pi$  are shown. Table 14 summarizes that fraction of pions within various momentum intervals relevant to the detector parameters to be discussed below. The momentum spectra for final state kaons are, of course, only slightly harder.

If the time-of-flight system is to provide particle identification up to the lowest momenta at which the RICH counters operate, the time resolution must be significantly better than that commonly achieved. An R&D program will be undertaken in the next year to verify that the needed extrapolation in performance is possible. If the results equal or exceed our expectations, the BCD should review the option that solely a time-of-flight system in the Central detector would be sufficient there for hadron identification.

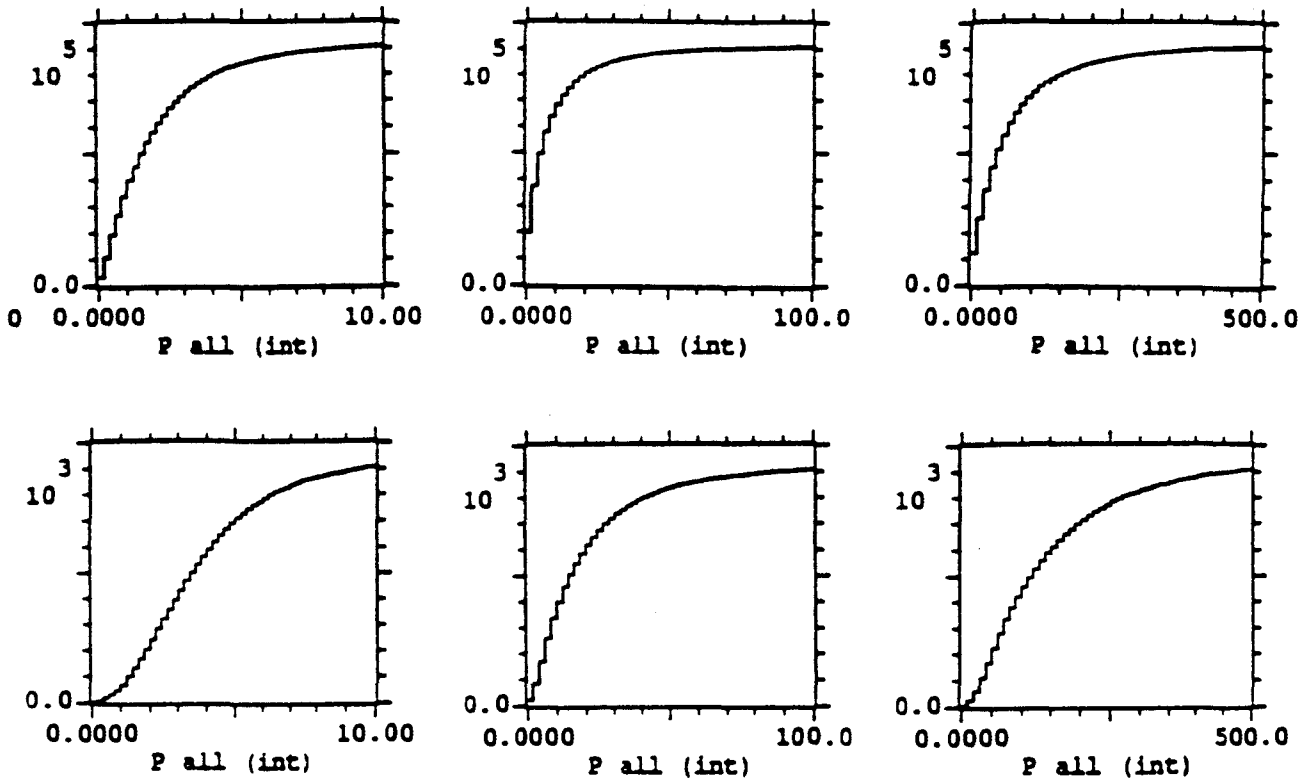


Figure 21: The integral momentum spectra of  $B$ -decay products in the Central, Intermediate, and Forward detectors, according to an ISAJET simulation. The upper three plots average over the ten decay modes listed in Table 5. The lower three plots are for the mode  $B^0 \rightarrow K^+\pi^-$ , which has the stiffest momentum spectrum of any nonleptonic  $B$  decay.

Table 14: The fractional momentum coverage for a single RICH counter in each of the three detector regions.  $P_{\min}$  is set by the upper limit covered by the time-of-flight system. The table entries are extracted from Fig. 21. 'All' refers to the average of all ten decay modes in Table 5, and ' $K\pi$ ' refers to the mode  $B \rightarrow K\pi$ .

Detector Region	$P_{\min}$ GeV/c	$P_{\max}$ GeV/c	% < $P_{\min}$ (All)	% < $P_{\max}$ (All)	% < $P_{\min}$ ( $K\pi$ )	% < $P_{\max}$ ( $K\pi$ )
Central	2	6	65	98	25	95
Intermediate	4	60	40	98	14	95
Forward	7.5	240	5	96	1	80

### 4.3.2 The Time-of-Flight System

For  $\pi$ - $K$  separation, the time-of-flight difference over a path length  $L$  is

$$\Delta t[\text{ps}] = \frac{L}{c} \left( \sqrt{1 + M_K^2/P^2} - \sqrt{1 + M_\pi^2/P^2} \right) \sim \frac{L}{c} \frac{M_K^2 - M_\pi^2}{2P^2} \sim \frac{3.75L[\text{cm}]}{P[\text{GeV}/c]^2}.$$

We suppose that  $\pi$ - $K$  separation is achieved if the resolution,  $\sigma_t$ , of the time-of-flight system is 1/2 of the time difference  $\Delta t$ . Table 15 summarizes the maximum momenta at which  $\pi$ - $K$  separation is possible by this criterion, for two values of  $\sigma_t$ . The time-of-flight counters would be located at 200 cm from the beams in the Central region, so the flight path  $L$  is taken as  $(200 \text{ cm})/\cos 33.7^\circ$ , noting that the highest-momentum particles occur at the smallest angle.

Table 15: The momentum coverage for  $\pi$ - $K$  identification in the time-of-flight system, for two values of the timing resolution  $\sigma_t$  according to the criterion that  $\Delta t = 2\sigma_t$ .

Region	$L$ (cm)	$P_{\text{max}}$ (GeV/c)	
		$[\sigma_t = 50 \text{ ps}]$	$[\sigma_t = 87 \text{ ps}]$
Central	240	3	2.3
Intermediate	730	5.2	4
Forward	2780	10.4	7.7

The needed timing resolution is primarily determined by the requirement that the time-of-flight system complement the capabilities of the RICH counter in the Intermediate region. There the minimum momentum at which  $\pi$ - $K$  separation can be achieved in a gas RICH counter is about 4 GeV/c. This suggests that a resolution of at most 90 ps is needed. Improvement of this to 50 ps would yield a better match between a time-of-flight system and the RICH counter in the Forward region, and such a resolution would provide  $\pi$ - $K$  separation for 85% of all particles in the Central region.

A time resolution of 150 ps can be achieved in a single 3-4-cm-thick scintillator viewed by a single phototube.<sup>[62]</sup> Better resolution would be achieved with greater light collection, but if the scintillator is made thicker then the time spread due to the scintillation at different points along the charged particle's path limits the performance. Better time resolution can only be obtained by combining several samples in 3-4-cm-thick scintillator with appropriate delays to correct for the charged-particle transit time. These samples could be combined into a single phototube using isochronous light guides, or read out via multiple phototubes. The latter option, while more expensive, provides some protection against noise in that an inconsistent time signal among the set could be discarded.

The conjecture is that the time resolution in a set of  $n$  scintillators each 3-4 cm thick would vary as

$$\sigma_t = \frac{150 [\text{ps}]}{\sqrt{n}}.$$

In this case we could achieve  $\sigma_t = 87$  ps with  $n = 3$  samples, and  $\sigma_t = 50$  ps with  $n = 9$ . The validity of this scaling will be verified in the coming months.

Here we base our design on three 3.33-cm-thick samples, each read out with a separate phototube. The total thickness of scintillator traversed by a particle is 10 cm, or 25% of a radiation length. We will investigate the option of using nine samples read out by three phototubes, which presents 75% of a radiation length to the particles. The time-of-flight system should also be regarded as part of the preconvertor for the electromagnetic calorimeter, which it directly precedes.

The time-of-flight counters will be arranged in a barrel in the Central detector, with the scintillators split at  $z = 0$  and read out only on one end via fiber-optic light pipes to avoid the magnetic field. These scintillators will be 3.6 m long. In the Intermediate and Forward regions the time-of-flight scintillators will be arranged as radial spokes, read out along the outer circumference. The Intermediate scintillators are 4.5 m long, and those in the Forward region are 1.7 m long.

We desire only a 1% occupancy in these scintillators, which leads to 1250 azimuthal cells in the Central region, and 2500 in each of the Intermediate and Forward regions. The area of the ends of the scintillators through which the light is collected is at most 4 cm<sup>2</sup>, so ganging three layers into a single phototube (via an isochronous light pipe) would be possible.

The scintillators themselves could be either solid bars, or scintillating-fiber bundles. Recent studies of the latter option<sup>[63]</sup> suggest that somewhat superior timing performance can be obtained with fiber bundles. So-called solid-state photomultipliers may become available in the next few years, and could find excellent application in the time-of-flight system.

The high performance of the time-of-flight system will also be useful in assigning tracks to the proper rf bucket, and could be used to implement multiplicity triggers. The time-of-flight system will play a role as part of the preconvertor, as previously mentioned.

## 4.4 Ring Imaging Čerenkov Counters

The viability of the Ring-Imaging Čerenkov (RICH) technique, which was proposed by Ypsilantis and Sequinot,<sup>[64]</sup> has been established by a number of groups<sup>[65, 66, 67]</sup> that have successfully built and operated devices in high-energy physics experiments. The central problem to be faced in designing a RICH counter for use at the SSC is obtaining stable operation in the anticipated high-rate, high-multiplicity environment. The RICH detector must be sensitive to the single-photoelectron pulses from Čerenkov light, but insensitive to the ionization trails of throughgoing charged particles. Furthermore, it must be possible to extract signals using a narrow timing gate so as to minimize confusion from overlapping events.

### 4.4.1 The Čerenkov Radiator

A RICH counter determines the  $\gamma$  of a charged particle by measurement of the Čerenkov angle, given by

$$\sin^2 \theta_C = \frac{1}{\beta^2} \left( \frac{1}{\gamma_t^2} - \frac{1}{\gamma^2} \right),$$

where  $\gamma_t = n/\sqrt{n^2 - 1}$  is the Čerenkov threshold in a medium with index of refraction  $n$ .

The ultimate limit to RICH counter performance is the dispersion in the Čerenkov angle due to variation of index  $n$  over the range of photon energies collected (chromatic aberration):

$$\Delta\theta_C = \frac{\Delta n}{n\sqrt{n^2-1}} \approx \gamma_t \Delta n.$$

For many gas radiators of interest,  $\Delta\theta_C \lesssim 5 \times 10^{-3} \theta_C$ . For the one liquid of interest as a RICH radiator,  $C_6F_{14}$ ,  $\Delta\theta_C \approx 0.01$ .<sup>[67]</sup> For the gas radiators, the spatial resolution of the photodetector determines the detector performance, rather than the chromatic aberration.

If the position of each photoelectron is measured to accuracy  $\sigma_r$ , and  $N$  photoelectrons are observed, then the number of standard deviations  $S$  between the Čerenkov rings for pions and Kaons of momentum  $P$  is

$$S = \frac{r_\pi - r_K}{\sigma_r / \sqrt{N}}.$$

For a counter whose light is focused by a mirror of focal length  $L$  (usually just the length of the counter itself), the radius of the Čerenkov ring of a particle of mass  $M$  is

$$r = L \tan \theta_C \approx \frac{L}{\gamma_t} - \frac{L\gamma_t}{2\gamma^2}.$$

Noting that  $1/\gamma = M/P$ , we have

$$r_\pi - r_K = L\gamma_t \frac{M_K^2 - M_\pi^2}{2P^2}.$$

The number of photoelectrons  $N$  is given by the expression

$$N = \epsilon \frac{\alpha}{\hbar c} \sin^2 \theta_C L dE \approx 370 [\text{cm}^{-1} \text{eV}^{-1}] \frac{\epsilon L dE}{\gamma_t^2},$$

where  $\epsilon$  is the efficiency for collecting the light and converting it to electrons, and  $dE$  is the range of photon energies collected. In a gas RICH detector  $\epsilon \sim 0.3$  has been achieved<sup>[67]</sup> ( $\epsilon \sim 0.15$  in a liquid RICH), and with  $dE \sim 1$  eV we then have

$$N \approx \frac{N_0 L}{\gamma_t^2},$$

where  $N_0 \sim 100/\text{cm}$ . Using this last relation for  $N$ , the momentum at which pions and Kaons can be separated to  $S$  standard deviations is

$$P[\text{GeV}/c] \approx M_K \frac{N_0^{1/4} L^{3/4}}{\sqrt{2S\sigma_r}} \approx 2(L[\text{cm}])^{3/4},$$

for  $N_0 = 100/\text{cm}$ ,  $S = 3$  standard deviations, and  $\sigma_r = 1$  mm. Thus if we wish to build a RICH counter of a fixed length  $L$ , the same  $\pi$ - $K$  separation can, in principle, be obtained with any gas! It seems wise to have a large number  $N$  of photoelectrons, so we should pick the gas with the minimum  $\gamma_t$  such that pions produce detectable signals over the entire relevant momentum range.

A similar expression can be derived for a liquid radiator followed by a drift space without focussing optics (so-called proximity focussing):

$$P \approx M_K \sqrt{\frac{\sqrt{N}}{2S\sqrt{n^2 - 1}\sigma_{\theta_c}}} \approx 9 \text{ GeV}/c.$$

The numerical value holds for  $N = 25$  photoelectrons,  $S = 3$ ,  $n = 1.27$ , and  $\sigma_{\theta_c} = \Delta\theta_c/\sqrt{12} = 0.003$  as for  $C_6F_{14}$ . The uncertainty in the Čerenkov angle due to chromatic aberration,  $\sigma_{\theta_c}$ , is assumed to be the limiting parameter. However, the proximity-focussing technique also introduces an uncertainty in the Čerenkov angle which varies inversely with the drift distance, and equals that due to chromatic aberration for a drift distance of 25 cm. Then for  $L = 25$  cm the maximum useful momentum for  $\pi$ - $K$  separation would be 6 GeV/ $c$ .

Table 16: Parameters of the RICH counters.  $L$  is the length of the radiator required to collect  $N = N_0 L/\gamma_t^2 = 25$  photoelectrons in a 1-eV range about 6.5 eV, supposing  $N_0 = 100/\text{cm}$  for the gas radiators, and  $N_0 = 50/\text{cm}$  for the liquid radiator  $C_6F_{14}$ .  $P_{\min} = \sqrt{2}\gamma_t M_\pi$  is the momentum at which the Čerenkov signal is 1/2 maximum, i.e., 12.5 photoelectrons. The radius of the Čerenkov ring is  $r_{\text{ring}}$ ,  $d$  is the edge size of the photodetector cathode pads, 'Area' is the instrumented surface area, and 'Pad Count' is the total number of detector pads in each region.

Detector Region	Radiator	$\gamma_t$	$L$ (cm)	$P_{\min}$ (GeV/ $c$ )	$r_{\text{ring}}$ (cm)	$d$ (cm)	Area ( $\text{m}^2$ )	Pad Count
Central	$C_6F_{14}$	1.6	1	0.3	38 <sup>†</sup>	3	24	27,000
Intermediate	$C_5F_{12}/CF_4$	20	100	4	5	2	62	155,000
Forward	$CF_4/Ne$	50	600	10	12	1.5	6	27,000

<sup>†</sup> While the Čerenkov angle for  $C_6F_{14}$  is 38°, the effective Čerenkov angle outside the radiator is 52° according to Snell's law.

The momentum ranges relevant for  $\pi$ - $K$  identification in  $B$  decays at the SSC are illustrated in Fig. 21 and Table 14. The values of  $P_{\min}$  are set by the maximum momenta covered by the time-of-flight system. We see that a momentum range of one decade in each region is sufficient, and hence a single radiator can be used for each region.

There is little need for  $P_{\max} > 6$  GeV/ $c$  in the Central region for typical  $B$  physics, so a liquid  $C_6F_{14}$  radiator is a good match. The one candidate solid radiator, NaF, has larger chromatic aberration, and the maximum momentum for  $\pi$ - $K$  separation would be only 3-4 GeV/ $c$ . In the Intermediate region a 1-m-long  $C_5F_{12}$  gas radiator will provide  $\pi$ - $K$  separation up to 60 GeV/ $c$ , and in the Forward region a 6-m long  $CF_4$  radiator would provide separation up to 240 GeV/ $c$ , both assuming a spatial resolution,  $\sigma_r$ , of 1 mm. The

gas radiators might actually produce more photoelectrons than we find convenient. If so these gases could be mixed with gases of higher  $\gamma_t$ , such as  $CF_4$ , or Ne, respectively, in such proportions as to reduce  $N$  to a desired value. In Table 16, which summarizes various properties of the proposed radiators, we suppose this has been done so as to achieve  $N = 25$ , which requires the nominal values of  $\gamma_t$  stated there.

If the spatial resolution can be made better than 1 mm the length of the Forward RICH counter could be reduced while maintaining  $N = 25$ . The length of the Intermediate RICH might then also be reduced, but this would aggravate the problem of diminished resolution due to multiple hits, discussed below.

#### 4.4.2 The Photodetector

The RICH counters in the Central, Intermediate, and Forward regions will all use the same technology to detect ultraviolet Čerenkov photons. The proposed photodetector is a multistep avalanche chamber (MSAC), shown in Fig. 22, which is operated at low pressure. The photodetector must be separated from the radiator and optics by a uv-transparent quartz window. The uv photons will be converted to electrons in a narrow gap of hot ( $80^\circ C$ ) photosensitive TMAE gas. The photoelectrons then drift into two amplification stages that are separated by a gate to allow high-rate operation.<sup>[68, 69]</sup> Readout will be accomplished via 'smart pads' with analog readout.

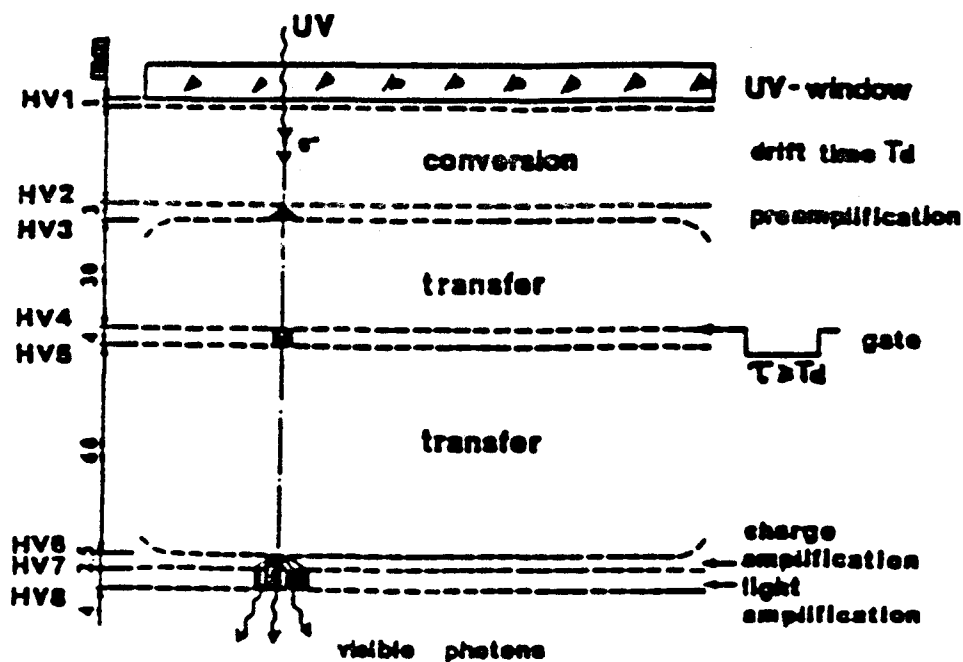


Figure 22: The photodetector of the RICH counters, consisting of a multistep avalanche chamber operated with low-pressure TMAE gas at  $80^\circ C$ .

Since the time scale for emission of Čerenkov light is intrinsically very short, the detector speed is limited by the photoelectron-transport process. In most devices built thus far,



a jitter in the photoelectron detection time occurs because the absorption length of the photosensitive gas is large enough that the photoelectrons produced at varying distances from the amplification region arrive there at significantly varying times. For example, the absorption length of TMAE at 30°C is about 15 mm, resulting in a 200-300 ns variation in pulse arrival time, depending on the carrier gas. Since this is several SSC-bunch-crossing times, a better technique must be developed.

Operation of the MSAC at low pressure and elevated temperature offers much improved timing resolution.<sup>[68, 69]</sup> At 80°C the vapor pressure of TMAE is sufficiently large that its photon-absorption length drops to  $\sim 1$  mm, reducing the spread in photoelectron transit times to about 20 ns. Even so, the total chamber pressure can be kept low enough (a few torr) that direct ionization can be reduced to less than one cluster per charged particle, rendering the chamber insensitive to throughgoing hadrons. Furthermore, at low pressure one can achieve a high gain at low voltages with minimal photon feedback from the amplification process. The latter feature eliminates the need for elaborate screens to isolate secondary photons from the main gas volume. One disadvantage of low-pressure operation is that one must support the quartz window against a 1-atmosphere differential pressure.

The parallel-plate geometry can easily accommodate a gating electrode, allowing one to select only those pulses of interest to be passed to the second stage of amplification. Such operation simplifies the electronic readout of the chamber and reduces the average current drawn by the final stage, thereby reducing aging effects. Finally, by placing a drift region between the first stage of amplification and the gating electrode, one obtains an economical trigger delay of several hundred ns.

#### 4.4.3 Readout

The two-dimensional Čerenkov-ring images must be read out with spatial resolution  $\sim 1$  mm in a high-rate, high-multiplicity environment. The approach employed in some existing designs<sup>[66]</sup> at  $e^+e^-$  colliders extracts one of the two position coordinates via timing over a long drift path. Although this technique affords precision position measurements and allows a single wire plane to cover a large photodetector area, the several-microsecond-long drift time makes it inappropriate for high-rate applications. Instead, we propose to implement a two-dimensional pixel readout based on cathode pads.

One can achieve the desired 1-mm position resolution in a straightforward way by dividing the cathode plane into  $\sqrt{12}$ -mm square pads, each instrumented with a simple amplifier-discriminator combination. However, the resulting number of channels ( $\sim 10^7$ ) is impractically large.

We plan to use a "wedge and strip" (W&S) approach.<sup>[68, 70, 71]</sup> This employs the repetitive three-electrode pattern shown in Fig. 23 to extract position coordinates via the relations

$$x = \frac{2S}{S + W + Z} \quad \text{and} \quad y = \frac{2W}{S + W + Z},$$

where  $S$ ,  $W$ , and  $Z$  are the charges collected on the three electrodes. A spatial resolution of  $\sim 1/20$  of the overall linear dimensions of the W&S pad has been achieved,<sup>[68]</sup> so large pads can be employed.

In another version of the 'smart pad' concept, the cathode plane is subdivided into a grid of many resistively interconnected padlets.<sup>[72]</sup> Figure 24 illustrates this a one-dimensional

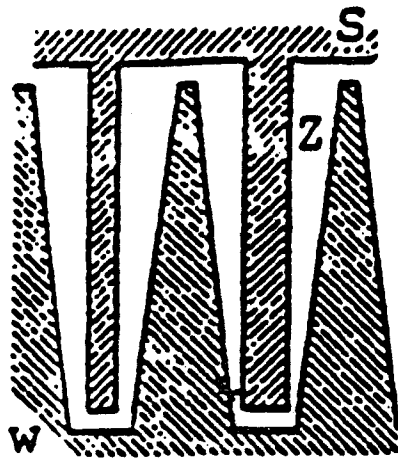


Figure 23: The wedge and strip readout scheme. Each cathode pad is subdivided into three electrodes, *S*, *W*, and *Z*, whose charges are separately digitized to provide *x-y* resolution much finer than the pad size.

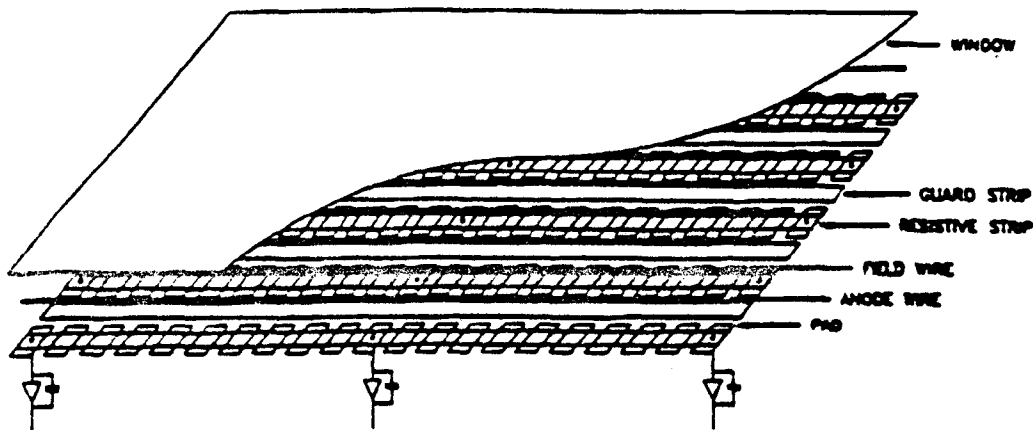


Figure 24: A scheme for cathode-pad readout in which adjacent pads are coupled via a resistance chosen to increase the charge sharing. Only every *n*th pad is read out.

readout based on this scheme. Induced charge on the cathode from an avalanche at some *x-y* location will be shared among four to nine instrumented padlets and the actual *x-y* location of the hit would be decoded from the relative size of the stored signal in each amplifier. Resolution along the anode wire direction is limited by relative amplifier gain, noise floor, digitization accuracy, and signal size and should be better than 1 mm even for 2 to 3 cm between amplifiers. Resolution perpendicular to the anode wire is, of course, limited to the quantization imposed by the wire spacing - about  $(2 \text{ mm})/\sqrt{12}$  for a reasonable

mechanical design. This quantization effect could be improved upon by including a time as well as a charge measurement in each instrumented pad.

The size and total number of pads should be determined by two considerations: the overlap of hits from different charged particles, and the overlap of hits from the same charged particle. With 100 charged tracks per event, each of which yields 25 photoelectrons in the RICH counters, there will be 2500 total signal hits per event. The criterion of 1% occupancy would then suggest the need for 250,000 pads. We propose to allocate a total of 210,000 pads among the three detector regions according to their width in pseudorapidity, as summarized in Table 16. From the total surface area of each RICH detector we then determine the average pad size in each detector, also given in the Table.

From the values of the radii of the Čerenkov rings and of the pad sizes, the number of pads intersecting a ring are 80, 16, and 50 in the Central, Intermediate, and Forward RICH counters, respectively. The low value of pads per ring in the Intermediate detector may be a problem. For two hits on the same pad the centroid lies not on the common circle to which they belong, but rather to the chord connecting them. In the worst case of a pair of points at either end of the W&S pad the effect introduces an error in the radius (for the pair) given by

$$\Delta r_{\text{ring}} \approx \frac{d^2}{8r_{\text{ring}}} = 1.0 \text{ mm},$$

for  $d = 2 \text{ cm}$  and  $r_{\text{ring}} = 5 \text{ cm}$  as in the Intermediate detector. Some 25% of the pads on a ring in the Intermediate detector would have two hits, which shifts the measurement of  $r_{\text{ring}}$  by an average of 0.5 mm on those pads.

## Pad Electronics

The pad electronics are architecturally similar to the straw system, but given the less stringent rise-time requirements can be implemented entirely in CMOS with a measurement time of about 30-50 ns. The recorded quantity in this case is charge, allowing spatial interpolation to about 1/20th of a pad spacing. In addition because of the simplification of the bookkeeping circuitry, it should also be possible to increase the number of channels per die from four in the straw-tube case to 16 or more in the pad case. Of course, each pad requires three readout channels in the W&S scheme.

## 4.5 Transition Radiation Detectors

### 4.5.1 Overview of Electron Identification

The identification of low-transverse-momentum electrons from semileptonic  $B$  decays is essential in the study of mixing and  $CP$  violation. It is well known that low-transverse-momentum electrons in a hadron collider environment will be difficult to identify because of the high multiplicity of soft charged and neutral tracks. This section discusses the sources of prompt and fake electrons in the BCD and presents a brief overview of how electron identification might take place with the present detector design.

### Sources and Relative Rates of Electrons

Prompt electrons derive from bottom and charm semileptonic decay, cascade decay of bottom through charm,  $e^+e^-$  decays of vector mesons, and Dalitz decays of pseudoscalar

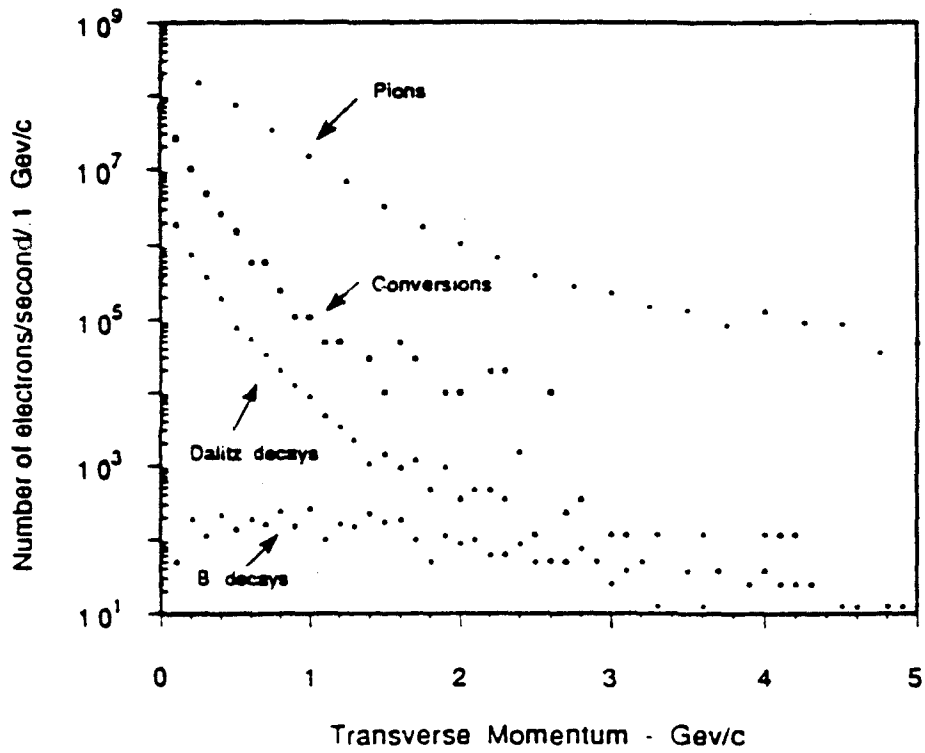
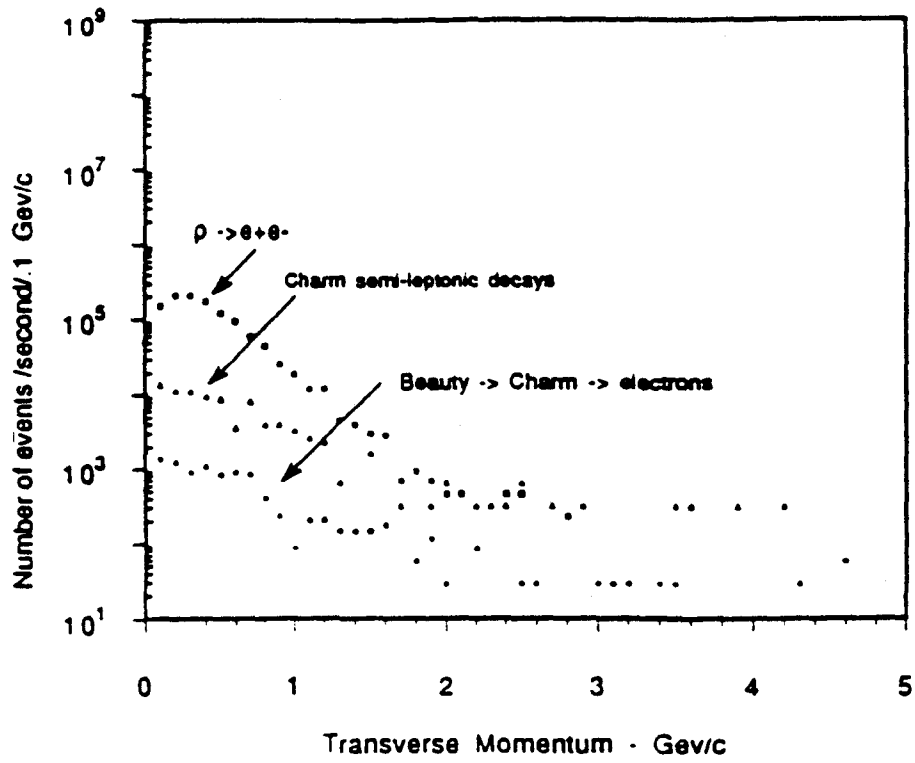


Figure 25: The  $P_t$  spectra of electrons in  $p$ - $p$  collisions at  $\sqrt{s} = 40$  TeV and a luminosity of  $10^{32} \text{ cm}^{-2}\text{sec}^{-1}$ .

mesons. Non-prompt electrons derive from  $\gamma$  conversions in the material before the transition radiation detector. A summary of the spectra of electrons from various sources, within the acceptance of the transition radiation detector, is shown as a function of  $P_t$  in Fig. 25. These spectra are from an ISAJET/GEANT simulation which includes the material in the beam pipe, silicon vertex detector, and straw tubes, with no effort to include material from cables *etc.* It can be seen that the spectra of all sources of electrons from other than  $B$  decays have a  $P_T$  of less than 0.5 GeV/c. The mean  $P_t$  of the prompt electrons from  $B$  decay is about 1.5 GeV/c. A cut on the spectrum at 1.5 GeV/c will remove roughly 60% of the signal while reducing the background dramatically.

Fake electrons will derive from misidentified  $\pi^\pm$ 's, including  $\pi^\pm$ - $\pi^0$  overlaps. A measure of the potential severity of the fake-electron problem is given by the rate for  $\pi^\pm$ , also shown in Fig. 25. The rates for 0-, 1.5-, and 3.0-GeV/c  $P_t$  cuts are given in Table 17. The largest rates are fake electrons due to misidentified hadrons. This background is not too difficult to reduce to an acceptable level. The rate of  $\pi^0$ 's, though large, is easily removed by matching a charged track to the shower. The fake-electron rate from overlaps is also potentially serious, but can in principle be eliminated by sufficient segmentation and good position matching between the charged track and the electromagnetic shower. The following subsections discuss conversions and fake electrons in more detail.

Table 17: Rates per event of electrons from various sources for different  $P_t$  cuts (Columns 2, 3, and 4). Electron rates per second at a  $\mathcal{L}$  of  $10^{32} \text{ cm}^{-2}\text{sec}^{-1}$  for a  $P_t$  cut of 1.5 GeV/c (Column 5). These numbers include acceptance for the Central and Intermediate TRDs. There is no cut on momentum. The total charged particle rate is included for comparison.

Process	$P_t > 0 \text{ GeV}/c$	$P_t > 1.5 \text{ GeV}/c$	$P_t > 3.0 \text{ GeV}/c$	$e^\pm (10^7 \text{ int./sec})$ $P_t > 1.5 \text{ GeV}/c$
Conversions	11.8	$16 \times 10^{-3}$	$1 \times 10^{-3}$	160,000
Dalitz Decays	0.74	$1 \times 10^{-3}$	$1 \times 10^{-4}$	10,000
$\rho \rightarrow e^+e^-$	0.12	$7 \times 10^{-4}$	$1.5 \times 10^{-5}$	7,000
$D \rightarrow X e \nu$	0.01	$8 \times 10^{-4}$	$2 \times 10^{-4}$	8,000
$B \rightarrow D e \nu$	$1.6 \times 10^{-3}$	$7.2 \times 10^{-4}$	$2 \times 10^{-4}$	14,000
$B \rightarrow D \rightarrow X e \nu$	0.001	$1 \times 10^{-4}$	$3 \times 10^{-5}$	100
$\pi^\pm, K^\pm$ (total)	115	2.3	$3 \times 10^{-3}$	$23 \times 10^6$
$\gamma$ 's from $\pi^0$	115	2.3	$3 \times 10^{-3}$	$23 \times 10^6$

### Electrons from $\gamma$ -Conversions in Matter

The largest rate of electrons, shown in Table 17, comes from conversions, which are relatively more abundant in the endcaps (88%) than in the Central detector(12%). The beam pipe accounts for less than 30% of all conversions. The strategies for eliminating conversions depend on the location of the conversion. There are three regions in which conversions take place, inside the beam pipe, in the beam pipe, and in the rest of the detector.

Internal conversions or Dalitz decays can be removed easily by requiring that the electron have zero impact parameter with respect to the primary interaction, since all electrons from  $B$  decay derive from a secondary vertex.

Conversions outside the beam pipe are easily removed by requiring hits in the innermost tracking detectors,

Conversions occurring in the beam pipe can be identified by several well-known methods. The most common method is to search for the partner either by reconstructing a mass or a vertex. In addition to the usual methods, it may be possible to exploit the 3-D tracking of BCD in the dipole field and reject conversions by identifying the zero opening angle in the non-bend plane. Conversions in the pipe may also be detected by a  $dE/dx$  measurement in the first silicon plane that has pulse height information available.

### Misidentified Hadrons

The rate of charged tracks into the detector is 115 tracks per event times  $10^7$  interactions per second or  $1.15 \times 10^9$  per second integrated over all  $P_t$ . Above a  $P_t$  of 1.5 GeV/c this rate reduces to 23 MHz. In order to reduce this source of background to the electron sample, we use several systems: the transition radiation detectors, the electromagnetic calorimeter, and the preconverter. A rejection of order  $10^5$  or greater should be achievable.

### Overlaps of $\pi^\pm$ and $\gamma$ 's from $\pi^0$ 's

A fake electron is generated if a charged track overlaps an electromagnetic shower in the ECAL. Initial rejection is obtained by spatially resolving the charged track from the  $\pi^0$  shower in the preconverter and electron calorimeter. With a tower size of  $|\Delta\eta| = 0.2$  and  $|\Delta\phi| = 0.2$  the overlap probability was shown in simulation to be less than 1%. These overlaps are dangerous only if the  $E/P$  cut is also satisfied. Assuming the electron calorimeter has energy resolution for photons of  $\sigma_E = 0.15\sqrt{E}$  the statistical significance of the  $E/P$  cut in standard deviations is

$$S.D. = \frac{|E - P|}{0.15\sqrt{E}}$$

A cut requiring a  $2\sigma$  separation of  $E$  of the  $\pi^0$  from the  $P$  of the  $\pi^\pm$  yields a rejection factor of 15. The TRD provides an additional independent rejection of 100 on the charged pion.

Electron identification will be accomplished in a combination of a transition radiation detector and an electromagnetic detector, discussed in greater detail below.

### 4.5.2 Transition Radiation Detector

The primary function of the transition radiation detector (TRD) is to assist in electron identification. Backgrounds to the electron signal arise from charged-pion showers in the electromagnetic calorimeter and from overlapping pions and photons. To attain an acceptable level of rejection of these sources, the TRD must be 90% efficient for electrons with energy above 1 GeV and allow no more than 1% contamination by pions or other heavy particles.

The most robust and straightforward technique to implement in a TRD is fine-sampling cluster-counting.<sup>[73]</sup> Such a device consists of many modules each with a radiator and photon detector, arrayed so that a charged particle passes through several modules. Each detector

cell reports only the presence or absence of an energy deposit above a threshold, where this threshold is chosen to discriminate between transition radiation and conventional charged-particle energy loss.

It is straightforward to build a device with plastic-film radiators having an efficiency  $\epsilon_R = 0.4$  per module for radiating particles, and efficiency  $\epsilon_N = 0.1$  for nonradiating particles.<sup>[74]</sup> These parameters will be used for the design presented here. There is some promise, however, that this performance may be considerably improved upon, and research in this direction is being carried on by members of this collaboration.<sup>[75]</sup>

If we have a detector that makes  $n$  samples each with efficiency  $\epsilon$ , then the probability of observing  $m$  or more hits is

$$\sum_{i=1, m}^n C_{i, m}^n \epsilon^i (1 - \epsilon)^{n-i}.$$

We used this to calculate the minimum value of  $m$  for several  $n$  that will provide 90% overall efficiency if each sample has efficiency  $\epsilon_R$  for radiating particles. The results are shown in Table 19. Also calculated was the maximum value of  $\epsilon_N$  such that the probability of observing  $m$  or more hits from nonradiating particles would be only 1%. From this we see that a TRD with  $\epsilon_R = 0.4$  and  $\epsilon_N = 0.1$  must provide about 25 samples on each track to yield > 90% overall radiating-particle efficiency with < 1% contamination per nonradiating particle. In this case the sampling requirement would be 7 or more hits per track.

Table 18: Overall efficiency and rejection of a TRD with  $n$  samples each of efficiency  $\epsilon_R$  for radiating particles. An overall efficiency of 90% for radiating particles is obtained by a requirement of  $M_{\min}$  or more hits. If the overall efficiency for nonradiating particles is to be only 1% then the maximum permissible efficiency per sample is  $\epsilon_N$ .

$n$	$m_{\min}$	$\epsilon_{N, \max}$
5	1	0.000
10	2	0.015
15	4	0.059
20	5	0.068
25	7	0.101
30	9	0.126
35	10	0.127
40	12	0.146
45	14	0.162
50	16	0.176

First principles may be applied to determine the mechanical characteristics of this detector. In order to produce TR quanta of useful energies (a few keV or more), the radiator material must have a plasma frequency  $\omega_p$  of order  $\omega_{\text{TR}}/\gamma \sim 8$  eV. Polyethylene, with  $\omega_p = 19$

eV, is a good choice. In order to avoid destructive interference within each layer of radiator, the radiator thickness must be somewhat greater than the "formation length (the distance over which the radiating particles falls one wave behind a radiated x-ray)," [78] given by

$$Z_{\text{formation}} \sim \frac{2\gamma^2 c}{\pi\omega},$$

or about 16  $\mu\text{m}$  for polyethylene (with  $\gamma \sim 10^3$ ). Similarly, the gas (or vacuum) gap between radiator sheets should be several times  $Z_{\text{formation}}$ . Since the number of TR quanta produced is about  $\alpha$  per interface, 200 foils are needed for each module of the detector in order to produce about one quantum per stack. This immediately tells us that the stack size must be of order

$$200 \cdot (15 \mu\text{m} + 150 \mu\text{m}) = 33 \text{ mm},$$

where we have used radiators of thickness 15  $\mu\text{m}$  separated by 150  $\mu\text{m}$ . A noble gas with high atomic number is advantageous for use in the x-ray detector of each module. We consider the use of xenon. It has an absorption length of about 1 cm for 10-keV photons, so this is taken as the thickness of the x-ray detector. Since the detectors for BCD will cover a large area and the signals produced are small, it is practical to place the first stage of electronics for readout directly on the detector. Our model allows 0.7-cm thickness for the electronics and associated cables in each detector module, and assumes a readout based on conventional gas-avalanche technology with a pad-chamber construction.

The modules arising from these design choices would be about 50-mm thick, and would be composed of materials with properties summarized in Table 19. A supermodule composed of 25 of these would be about 125-cm thick. It is anticipated that the ongoing research in optimization of materials for the TRD would allow the needed performance to be achieved in a device of thickness 50 cm or less, and this is the size of the device proposed for the Central region of the BCD. Figure 26 shows a schematic cross section of the TRD as described here. Figure 27 represents the overall configuration for the Central detector region, indicating its division into four pieces for assembly.

Table 19: Physical properties of the proposed TRD.

Layer	Thickness (mm)	Effective $A$	Effective $Z$	Average $\rho$ (g/cm <sup>2</sup> )	Effective $L_{\text{rad}}$ (cm)
Radiator	33	13.7	6.89	0.1	520
Detector	10	3.7	2.2	0.3	130
Readout	7	16.9	8.4	0.4	40

The TRD-pad electronics are architecturally similar to that for the straw system, but without the need for a very fast rise time since the TRD is a threshold device. The TRD front-end electronics can thus be implemented entirely in CMOS with a measurement time of about 30-50 ns. While we have discussed the performance of the TRD assuming it is



operated as a threshold device, it is a realistic option for the electronics to record the signal charge.

Simulations using GEANT show that the TRD must be segmented into cells of size roughly  $\Delta\eta \times \Delta\phi \sim 0.1 \times 0.06$  to keep the occupancy below about 1% per cell. With 25 layers per module this results in about 250,000 channels of TRD readout.

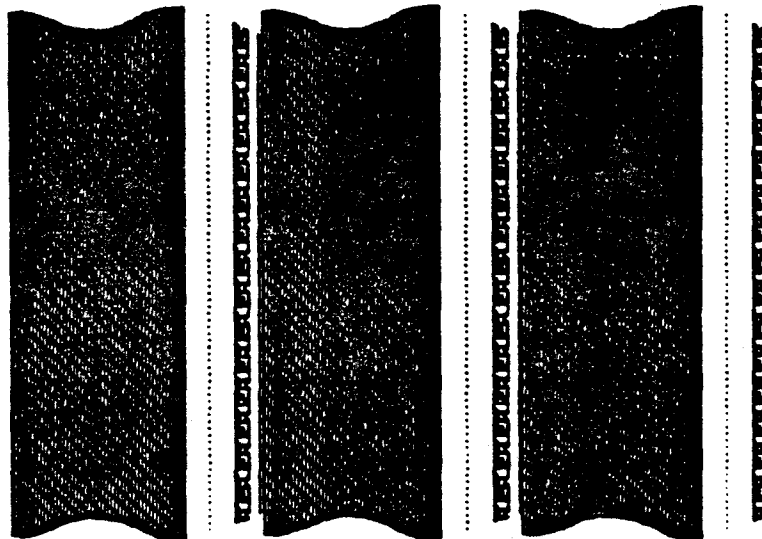


Figure 26: Schematic view of three modules of the TRD. Particles would traverse the section from left to right, passing through the radiator, the photon detector, and the readout layers.

## 4.6 Electromagnetic Calorimeter

The purpose of the electromagnetic calorimeter is to aid in the identification of low  $P_t$  electrons. The tagging of the electrons from  $B$  decay is important and a calorimeter with a high efficiency for identifying electromagnetic showers is needed.

The rate of charged pions interacting in the calorimeter is high, and therefore emphasis is placed on good  $\pi - e$  rejection. This can be obtained by segmenting the calorimeter in both the transverse and longitudinal dimensions. Good position information at the entrance to the calorimeter and at shower maximum will aid in rejecting charged  $\pi$ 's overlapping with photons.

The BCD does not intend to reconstruct those decay modes of the  $B$  that involve neutral pions. This and the above criteria suggest that precise energy measurements of the electromagnetic shower will not be necessary.

The calorimeter plays an important role in the prompt electron trigger because of the need to reject the interacting pions as well as identifying electrons from  $B$  decay. A fast detection medium is well suited to the needs of the BCD.

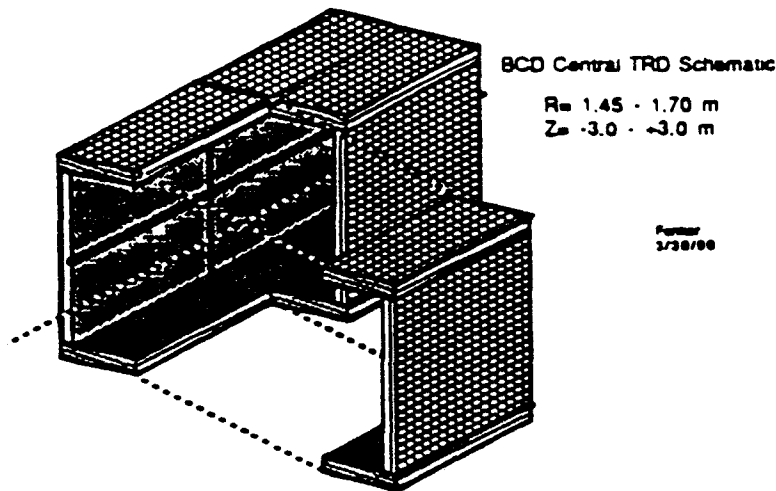


Figure 27: Schematic of the Central TRD showing its assembly from four sectors.

The conceptual design of the electromagnetic calorimeter consists of a preconverter, two longitudinal sections and a hadron catcher. The preconverter consists of charged particle track information before and after 1.5 radiation lengths of lead. We are studying the integration of the TOF system which consists of scintillating fibers with the preconverter. The calorimeter is about 25 radiation lengths deep in order to contain the shower. It is divided longitudinally at shower maximum, which is roughly 5-7 radiation lengths deep. A pad chamber is being investigated as a position sensing device at shower maximum. The muon steel located behind the calorimeter is instrumented after two interaction lengths to provide rejection against interacting charged pions.

The simplest technology capable of providing the above specifications and that can be fast enough to contribute to a prompt trigger is a sampling lead-scintillator calorimeter. This choice of technology can easily achieve an energy resolution of  $15\%/\sqrt{E}$ , which is adequate for our purposes. The lead/scintillator will be arranged in towers and could be constructed of either bulk scintillator or scintillating fibers.<sup>[76, 78, 77]</sup> Calorimeters of this type can provide charged-pion rejection on the order 400:1, which is adequate for the BCD.

A conventional readout of the calorimeter via photomultiplier tubes is adequate for the BCD in the Intermediate and Forward regions. Because of the magnetic field in the Central region, the light must be brought outside the field. One method to accomplish this employs fiber-optic cables, operating as light guides, to bring the scintillation light to a field-free region.

Overlap studies between charged  $\pi$ 's and photons using the BCD GEANT3 Monte Carlo indicate that a tower size of  $\Delta\eta \times \Delta\phi = 0.08 \times 0.08$  will have less than 1% overlap of gammas with charged tracks. This segmentation leads to 7000, 14000, and 6000 channels in the Central, Intermediate, and Forward detectors respectively.

In keeping with our philosophy of standardized front-end electronics, the readout archi-

# BCD Electromagnetic Calorimeter Electronics

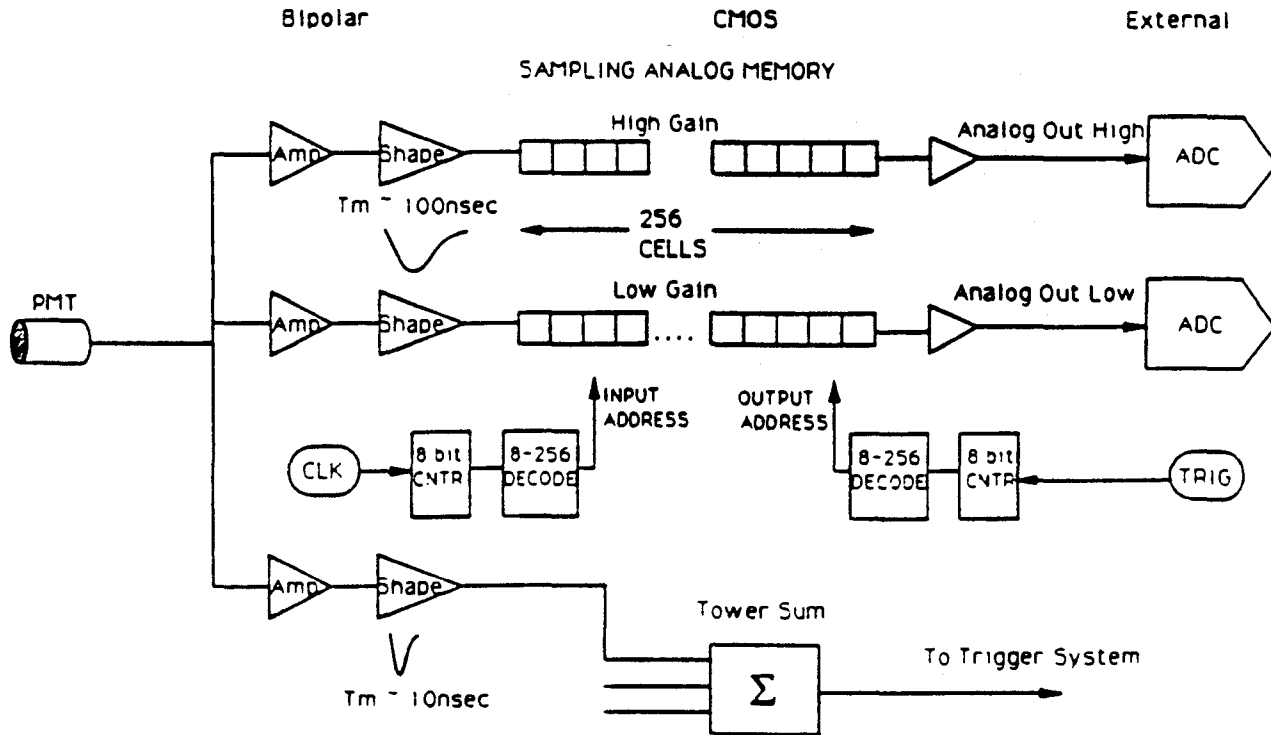


Figure 28: Electronics for the Electromagnetic Calorimeter.

ecture is very similar to that of the straws and the silicon. A block diagram is shown in Fig. 28.

## 4.7 Muon Detector

The detection of muons is an important part of the study of bottom production and decays at the SSC. Muons can provide a clean trigger for the experiment and can also provide a tag of the  $B$  meson when combined with information from the  $D$  decay. High mass dimuons can signal  $J/\psi$  meson decay and semi-muonic decay of both  $B$  hadrons, which are a rich tag of  $B$  mesons at the SSC. For the design of the muon system for the BCD detector, production of muons from various bottom decays has been simulated using PYTHIA 5.3 / JETSET 7.2.

### 4.7.1 Overview

The muon system is designed to detect and identify prompt muons from  $B$  decay. Such muons are produced at low  $P_t$ , typically 1-2 GeV/c. Muons are identified by their ability to penetrate the steel absorber. The function of the muon system is to perform muon identification and measure the muon position and time of occurrence with enough resolution to be able to link unambiguously the muon candidate to the corresponding track from the central and/or forward tracking system at the appropriate bunch crossing and ultimately

to link to the silicon vertex system to establish whether the muon comes from a secondary decay vertex or not.

The muon system is not designed to measure muon momentum by itself. The muon momentum is measured by the central and forward tracking system from the bending the linked track has sustained in the dipole magnet(s). The muon system simply identifies which of the reconstructed tracks from the central and forward tracking system are muons by linking muon track segments to reconstructed tracks before the steel. Tracking chambers are installed behind the absorber to track the exit muons. The projected position of the multiple scattered muon track candidate has to agree with the muon chamber measurements. A spatial resolution comparable to the multiple Coulomb scattering of the highest energy muons (200 GeV/c) is needed for the muon chambers. This translates to a requirement of about 650  $\mu\text{m}$ , which falls comfortably within the capability of drift chambers. However, in order to better tie the muon chamber hits to a specific bunch crossing, 250–350  $\mu\text{m}$  resolution is needed.

In addition the muon system is also to provide a prompt first level trigger for single muons and dimuons.

#### 4.7.2 Detector Layout

The muon steel and detector layout can be seen in Figure 7. Muon detection is fully instrumented in two of the three possible regions. The central region (which extends from 588 mrad to  $90^\circ$ ) is either not instrumented or else only crudely instrumented. There are several reasons for this. First, muons near  $90^\circ$  having a low  $P_t$  of 1–2 GeV/c also have comparably low momentum and so a large number will be stopped by the steel of the magnet poles and lost. Second, this is also the region with the poorest momentum resolution because of the orientation of the dipole magnetic field. The intermediate region is fully instrumented on both sides of the interaction point and covers 100 mrad to 588 mrad. The forward region is fully instrumented in a single arm only and covers 13 mrad to 100 mrad. If a second forward arm is desired, then all quantities relevant for one forward arm can be doubled. The intermediate and forward muon systems will now be described more fully.

**Muon Steel Layout** The properties of steel used here are that one meter of steel equals 3.0 nuclear interaction lengths for high energy pions (based on  $\lambda_I = A/(N_A \times \sigma_I)$  where  $\sigma_I = 20 \text{ nb} \times A^{0.72} = 360 \text{ nb}$  for Fe), 57 radiation lengths, and will have 1.2 GeV of minimum ionization  $dE/dx$  energy loss. The mean momentum of  $B$  decay muons in the forward muon system is 50 GeV/c and ranges from 10–200 GeV/c. The corresponding values for  $B$  decay muons in the intermediate muon system are a mean of 12 GeV/c and a range from 5–50 GeV/c.

For the intermediate detector, the total steel thickness increases with pseudorapidity from 3 m of steel to 4 m of steel for  $1.2 < |\eta| < 3$ . After the first 42 cm of steel is placed a hadron catcher to be used with the electromagnetic calorimeter to aid in pion rejection. Three chamber sets, each set comprising two chamber planes, are used to detect the muons. The first two sets are separated by 0.5 m of steel. In addition the last 0.5 m may possibly be magnetized toroidally to aid in rejecting hadron showers and punchthrough.

For the forward detector ( $3 < \eta < 5$ ), the total steel thickness is 8 m. Again three chamber sets are used to detect muons each of which is separated by 1 m of steel. In addition the last 1.0 m may possibly be magnetized toroidally to aid in rejecting hadron showers and punchthrough.

**Chamber Description** Two alternative types of chambers are being considered for use in the muon tracking system: i) Use of extruded PVC "Iarocci" tube chambers run in drift mode with the wires read out by TDC's and with a pad and strip structure for the induced signal; or ii) a Resistive Plate Counter (RPC) system (such as the one currently being built by the INFN, the University of Lecce, and the University of Pavia for Fermilab experiment E771) which use pad and strip readout of induced signals. The two alternatives will be discussed briefly below.

**PVC Streamer Tube Scenario** PVC streamer tubes developed by Iarocci *et al.*<sup>[79]</sup> can provide inexpensive large area coverage for the muon system. Extruded PVC profiles are coated with a carbon suspension with a surface resistance in the range of 0.2 to 2.0 M $\Omega$  per square. Anode wires are strung and supported every 0.5 m. Typical chambers are made with eight 1 cm  $\times$  1 cm cells as shown in Figure 29. These chambers are traditionally operated in the limited streamer mode. However, they can also be operated in the proportional mode with a smaller wire diameter. In either case a spatial resolution is expected in the range of 250-350  $\mu$ m. If run in the limited streamer mode, then sizable wire and induced signals can be generated which will simplify the readout electronics. The readout electronics for the straw tube system is capable of handling the smaller signal size should the chamber need to be run in the proportional mode. The rate capability of these chambers running in the streamer mode exceeds 50 Hz/cm<sup>2</sup> and therefore poses no dead-time problem for muon detection. The overall geometric acceptance, taking into account the 1 mm wall between the 1 cm cells is 88% per plane. By staggering two planes by half a cell, the geometric loss is reduced to < 1%. The staggered geometry also removes the left-right ambiguity.

The muon tracking system consists of 3 detector stations, two of which are embedded in steel. Each tracking station comprises 2 staggered planes of streamer tubes. Boards with 1 cm wide strips will be glued to one side of the chamber and boards with a pad structure will be attached to the other side to detect the induced signal. The strips run perpendicular to the wires to provide position measurement for the orthogonal coordinate.

The wire signals are amplified and fed into a pipelined TDC for drift time measurements in the bend plane ( $x$ ) coordinate. The maximum drift time for a 1 cm cell is about 200 ns. The strips provide discriminated and latched digital measurements of the non-bend plane ( $y$ ) coordinate of the muon trajectory with a resolution of about 3 mm. The discriminated and latched digital signals from the pads will be used for the prompt muon trigger and to eliminate ghosts from the wire and strip analysis.

In the intermediate system the three measurement layers are separated by 0.5 m of steel (with the last 0.5 m of steel set up as a possible toriodal magnet). In the forward system the three measurement layers are separated by 1.0 m of steel (again with the last 1.0 m of steel set up as a possible toriodal magnet). The steel is square and the chambers are divided

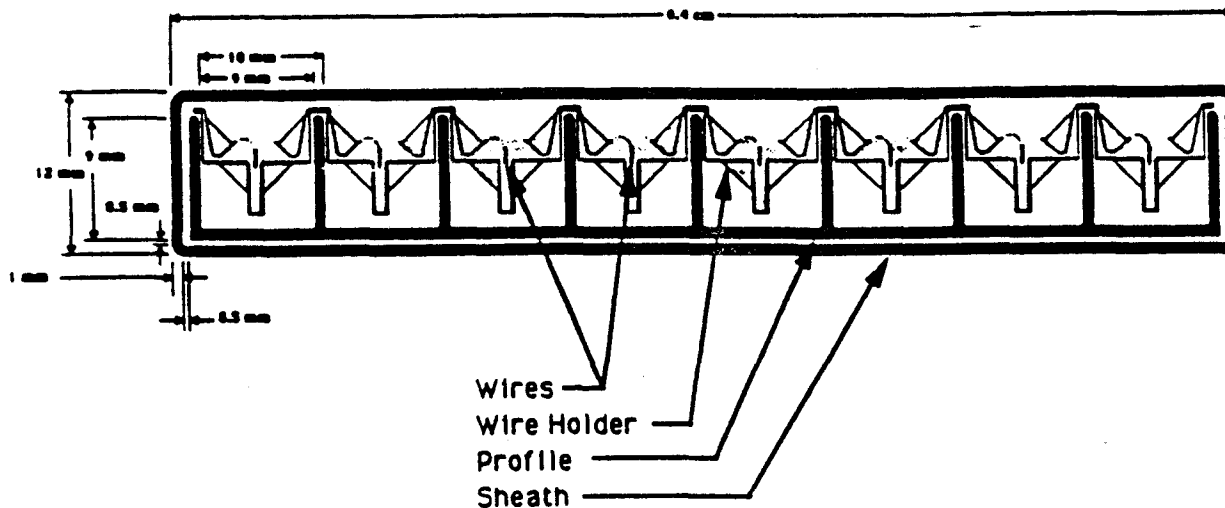


Figure 29: Cutaway of an eight-cell PVC Streamer Tube module.

into quadrants. The size of the chamber area to be covered in the intermediate detector measurement layers is 16.7, 16.0, and 15.3 meters full transverse size. The wires are strung vertically in each quadrant. This leads to 19,200 wires for a 1 cm cell width, 9,600 strips and 15,000 pads (20 cm × 20 cm) per intermediate arm. The forward arm contains 8,700 wires, 4,350 strips, and 15,000 pads (10cm × 10 cm). A double layer of pad (and strip) signals is ganged and the ganged sum feeds into a single discriminator. The total number of simple discriminator channels (pads and strips) is 68,550. The total number of TDC channels (wires) is 47,100.

These chambers can be produced *en masse* in highly automated assembly facilities. The Streamer Chamber Assembly and Research Facility (SCARF) at the University of Houston is capable of producing and testing 20–50 chambers per day.<sup>[80]</sup> The total number of chambers needed for the muon tracking system is about 6,000 which can be produced in leisure in less than one year. In order to achieve the required spatial resolution, the painted profiles (see Figure 29) need to be secured rigidly to the sheath which in turn will be attached to the support structure. A rigid structure can be made by gluing the two layers of chambers with strips and spacer in between. The modules will be surveyed into position. The wire positions will be located to better than 100 μm by software. The daily variations due to temperature changes will be monitored and corrected for on an hourly basis.

**Resistive Plate Counter Scenario** The RPC scenario would use a set of resistive plate counters for the muon detectors. RPC's<sup>[81]</sup> are dc-operating gaseous charged particle detectors utilizing a constant and uniform electric field produced by two parallel electrode plates, one or both of which are made of material with high bulk resistivity. There are no wires in this type of chamber, readout is done entirely via induced charge on pads and strips. The two electrodes are run with a large DC potential difference them and the gap between the electrodes is filled with a gas having a high absorption coefficient for ultraviolet light.

When the gas is ionized by a charged particle crossing the counter, a discharge is initiated by the large electric field. However, the discharge is limited to a small localized region of space because of the high resistivity of the electrodes and the large quenching of the gas.

One advantage RPC's have over wire chambers or limited streamer tubes is that it has much better time resolution. The reason for this is due to the uniform electric field of the RPC compared to the radial field of a wire chamber which have large time variations due to the electron drift.

Typical RPC's have been built using electrodes made of a phenolic polymer having a bulk resistivity of  $\rho \approx 10^{11 \pm 1} \Omega\text{-cm}$ . The gap between electrodes is 2 mm and a uniform electric field of  $\approx 4 \text{ kV/mm}$  is used with a gas of 69% argon, 27% butane, and 4% Freon. Pulse durations of  $\tau \approx 10 \text{ ns}$  and time resolutions of  $\Delta t \approx 1 \text{ ns}$  have been measured for such chambers (compared with drift times of several hundred ns for chambers using wires). Although such chambers require the electrodes to be flat to a small tolerance, construction of RPC's has not proven difficult providing proper care and design is taken.

A limitation of RPC's which must be considered is the rate capability. When a discharge occurs, a cell of area  $\approx 0.05 \text{ cm}^2$  around the discharge point remains inactive for a dead time of  $\approx 10 \text{ ms}$ . The effect this can have on reducing chamber efficiency then depends on the track density at various points in the detector and the overall interaction rate. Efficiencies of 97% have been measured for RPC's at low rates. A linear decrease of the RPC efficiency with respect to the particle flux of  $\approx 6\%/(50 \text{ Hz/cm}^2)$  has also been measured. Thus, if one wants a single chamber efficiency of 90% or higher, the local instantaneous particle flux into the RPC should be limited to  $\approx 60 \text{ Hz/cm}^2$  or less. This will not be a serious limitation for muon detection where the chambers are placed behind many meters of steel and see only muon signal and background rates.

Since there are no wires all readout must be via induced signals. Both sides of the gap in the RPC will be read out, one side with pads to be used in the muon trigger and the other with narrow strips to provide a precise position measurement. Two RPCs will be used in each of the three muon chamber sets. Pad signals from the two RPCs will be ganged for the trigger to increase the trigger efficiency. The two strip signals will provide precision  $x$  and  $y$  position measurements. The segmentation size and number of channels will be identical to that discussed earlier for the streamer tube chamber.

### 4.7.3 Radiation Damage Consideration for the Muon Chambers

Current Streamer Tube construction uses PVC plastic. Current Resistive Plate Counters are made from phenolic polymer. Both plastics may exhibit structural radiation damage at high radiation levels. The radiation level these devices will experience in BCD will be lessened since they are shielded by the muon steel. However, estimates of these radiation levels will be made and if they prove too detrimental to the muon chamber's structural integrity, then a search for alternative materials will be made.

### 4.7.4 Backgrounds

**Introduction** To define a muon candidate, we choose to combine a powerful measurement of the momentum in the forward and central tracking systems with a track segment

determined after at least 9 interaction lengths of steel. The bulk of the muon steel is not magnetized (with the possible exception of the last 0.5–1.0 m) since the muons must be linked cleanly with the tracking and microvertex systems to determine whether the muons come from secondary vertices. This link up with the tracking system will also provide the precision measurement of the muon momentum. We may choose to magnetize the last 0.5–1.0 m of muon steel chiefly to help in reducing the background from hadron punchthrough and not for providing any precise muon momentum measurement which we rely on the tracking system to provide.

There are several backgrounds to the muons coming from  $B$  decay which have been studied by using PYTHIA/JETSET:

**Direct Charm** Semi-muonic decay of directly produced charm is in fact the principal source of background muons having a minimum  $P_t$  of 1–2 GeV/c. This background is discussed more fully below in conjunction with the single muon rates. This background is preferentially rejected relative to muons from  $B$ 's by making the above transverse momentum cut.

**Minbias  $\pi$  and  $K$  decay** Decay of pions and kaons in flight from ordinary interactions constitute the second major source of background muons. This background is also discussed more fully below. The muons from these decays have a very soft  $P_t$  spectrum and are cut quite effectively with a modest  $P_t$  requirement.

**Single Hadron Punchthrough** This has been studied using the parameterization for hadron punchthrough developed by A. Bodek.<sup>[82]</sup> For the muon momenta and muon steel thickness for BCD, this rate is a fraction of the  $\pi/K$  decay rate. However, punchthrough is most severe closest to the beam where particle scraping along the edges of the muon steel also occurs. This particular region requires further study and may require reducing the fiducial area of the muon chambers by the small amount.

**Occupancy and Pileup** The segmentation of the muon drift chamber system is chosen to give an average occupancy of about 1%. The estimate of the occupancy is given by

$$O \approx \frac{\pi w}{R_T} \left( 1 + \frac{\Delta t}{\tau} \right)$$

where  $\Delta t$  is the drift time,  $\tau$  is the average time between collisions,  $w$  is the cell width, and  $R_T$  is the transverse distance from the beam. The innermost layers of the intermediate muon system have an maximum occupancy of about 5%.

**Track Overlap and Mislinking Tracks** This background arises when the track segment found in the muon system is connected to the wrong track from the central or forward tracking system and requires further detailed simulation studies.

**Multiple Interactions Per Crossing** This background is directly dependent on the luminosity at which BCD will run. Poisson statistical variations in this quantity can produce some crossings where this may be a severe problem.



**Neutrons** We may want to place concrete at the ends of the intermediate and forward muon chambers in order to absorb neutrons. The size and importance of background needs further study.

#### 4.7.5 Muon Momentum Resolution

The muon momentum resolution is given by that of the charged tracking system since the muons must be linked to this system to determine whether the muons come from  $B$  decay secondary vertices. The momentum resolution of this system is given by:

$$\frac{\Delta P}{P} \approx 1\% \times P$$

for tracks with  $P_t < 4 \text{ GeV}/c$ .

#### 4.7.6 Single Muon Rates

The muon rates are reduced by the length of the muon steel which serves to range out low momentum muons and to impose a passive  $P_t$  cut on the observed muons. Further reduction is achieved with a hardware  $P_t$  cut of 1-2  $\text{GeV}/c$ . The rest of the rate is handled in a microprocessor ranch.

The primary background to the bottom muon signal is from the direct production of charm and from  $\pi$  and  $K$  decay; these backgrounds have also been studied with PYTHIA.

The most relevant features of the BCD geometry for muon signals and background are i) the amount of free decay space (for  $\pi/K$  decay), and ii) the thickness of the muon steel. The values of these quantities for the two regions of the BCD detector fully instrumented by muon detection are:

1. Intermediate ( $1.2 < |\eta| < 3$ ): The length of the decay region is 7.4 m. A shaped iron muon shield is used here whose thickness varies from 3 m at  $\eta = \pm 1.2$  to 4 m at  $\eta = \pm 3$ . The stopping power is roughly parameterized by:  $p_{\text{cutoff}} \approx 0.67|\eta| + 2.8 \text{ GeV}/c$ .
2. Forward ( $3 < \eta < 5$ ): The length of the decay region is 27.1 m. An 8 m iron muon shield is used which has a stopping power of 9.6  $\text{GeV}/c$ .

In Table 20, single muon rates have been simulated for various signal and background channels using PYTHIA. The muon signals examined were:

- Semi-muonic  $B$  decay
- Semi-inclusive  $B$  decay to  $D$  with the  $D$  decaying semi-muonically

The following background muon channels were also studied:

- Direct  $D$  production with the  $D$  decaying semi-muonically
- $\pi$  and  $K$  decay to muons

Table 20: Single Muon Signal and Background Rates (in units of Number of Muons / Interaction)

Mode	In Geometric Aperture	+ Muon Steel $P$ Cutoff	$+P_t > 1 \text{ GeV}/c$	$+P_t > 2 \text{ GeV}/c$
Intermediate Detector—Single Arm				
$B \rightarrow \mu + X$	$1.98 \times 10^{-4}$	$1.54 \times 10^{-4}$	$1.46 \times 10^{-4}$	$9.68 \times 10^{-5}$
$B \rightarrow D + X \rightarrow \mu + X$	$1.98 \times 10^{-4}$	$6.20 \times 10^{-5}$	$5.10 \times 10^{-5}$	$2.10 \times 10^{-5}$
Direct $D \rightarrow \mu + X$	$2.01 \times 10^{-3}$	$6.43 \times 10^{-4}$	$5.09 \times 10^{-4}$	$2.01 \times 10^{-4}$
$\pi/K \rightarrow \mu\nu$	$3.50 \times 10^{-4}$	$5.43 \times 10^{-6}$	$3.55 \times 10^{-6}$	$6.93 \times 10^{-7}$
Forward Detector—Single Arm				
$B \rightarrow \mu + X$	$1.18 \times 10^{-4}$	$9.68 \times 10^{-5}$	$8.36 \times 10^{-5}$	$5.39 \times 10^{-5}$
$B \rightarrow D + X \rightarrow \mu + X$	$1.38 \times 10^{-4}$	$6.10 \times 10^{-5}$	$3.60 \times 10^{-5}$	$1.20 \times 10^{-5}$
Direct $D \rightarrow \mu + X$	$1.64 \times 10^{-3}$	$7.10 \times 10^{-4}$	$3.22 \times 10^{-4}$	$1.21 \times 10^{-4}$
$\pi/K \rightarrow \mu\nu$	$3.63 \times 10^{-4}$	$2.43 \times 10^{-6}$	$3.95 \times 10^{-6}$	$6.13 \times 10^{-7}$

Muon rate due to pion punchthrough was also estimated using the parameterization of A. Bodek<sup>[82]</sup>. A minimum muon-shield thickness of 2 m of iron was required to keep the punchthrough rate to a fraction of the  $\pi/K$  decay rate and this condition is met with our muon shields.

Table 20 presents the single muon rate as a function of a variety of simple cuts. The rate is normalized as the number of muons per interaction and is calculated for the forward hemisphere only ( $\eta > 0$ ). All appropriate branching ratios and decay probabilities are included in these rates. In addition, the values for the bottom and charm production cross sections at  $\sqrt{s} = 40 \text{ TeV}$  that were used were:

$$\sigma_{b\bar{b}} \approx 0.005\sigma_{\text{Tot}}$$

$$\sigma_{c\bar{c}} \approx 10\sigma_{b\bar{b}}$$

Table 20 leads one to conclude that a transverse-momentum trigger or filter cutting on values of  $P_t$  between 1 and 2 GeV/c is necessary to improve the single-muon signal-to-background ratio for finding bottom. Also the primary background to the single-muon rate for bottom is not due to  $\pi/K$  decay, but is due to the direct production of charm which subsequently decays semi-muonically. Note that all the values in the Table 20 can also apply for the semi-electronic decay channels, except for the  $\pi/K$  decay channel. The electron channels will of course have other backgrounds than those described here, primarily ones due to photon conversion and bremsstrahlung.

## 4.8 Luminosity Monitor

The luminosity monitor samples forward tracks in hodoscopes of scintillating fibers that measure position in the nonbend plane. Thus the monitor can also provide a fast estimate of the  $z$  position of the primary event vertex. The fast determination of the vertex  $z$ -position will be used in the prompt-tracking trigger.

The luminosity monitor is constructed of 0.5-mm-square scintillating fibers that are read out with phototubes. There are four stations at  $\pm 200$  and  $\pm 400$  cm from the interaction point. Each station is divided into four quadrants, and each quadrant is a superlayer of fibers eight fibers thick. All eight fibers in a row of a superlayer are read into a single phototube. The coverage in pseudorapidity is  $3.7 \leq \eta \leq 5.7$ , corresponding to  $7 \text{ mrad} < \theta < 50 \text{ mrad}$ . Each quadrant superlayer at  $z = 200$  cm then has 172 rows of fibers, and there are double that number at  $z = 400$  cm. The total number of readout channels is 4128.

A Monte Carlo simulation indicates that the probability of estimating  $z$ -vertex to  $\pm 1$  cm is 75%.

## 5 Triggers and Data Acquisition

### 5.1 Introduction

The rate of  $B\text{-}\bar{B}$  production at a luminosity of  $10^{32} \text{ cm}^{-2}\text{sec}^{-1}$  is 50 kHz, which is 1/2% of the total interaction rate of 10 MHz. The experimental trigger should not be overly restrictive if we wish to collect the large sample of  $B$  decays needed for studies of  $CP$  violation. Because of the low mass scale of the  $B$ 's they occur in events kinematically similar to 'minimum-bias' events. An efficient  $B$  trigger will therefore also accept a fraction of the minimum bias events. Hence the data-acquisition system will need to have very high rate capability by present standards.

Historically, the trigger strategies proposed for  $B$  physics have been a single-lepton trigger, a  $J/\psi$  trigger, and an impact-parameter (secondary vertex) trigger. The lepton triggers are somewhat restrictive. For example, the self-tagged  $B$  decays, such as  $B \rightarrow K^+\pi^-$ , test  $CP$  invariance without the need for an independent tag, and a lepton from the decay of the second  $B$  plays no role in the physics analysis. The  $J/\psi$  trigger explores only one aspect of the richness of the  $B$  system, but could be used at higher luminosity than other triggers. The secondary vertex-trigger is the most general, but is difficult to implement quickly.

We propose an architecture<sup>[83]</sup> in which a single level of prompt triggering provides only a modest reduction in the event rate in 1.5-2  $\mu\text{sec}$ , and a large online computer ranch<sup>[85]</sup> implements software triggers based on correlations of full-resolution data from several sub-systems of the detector. This is shown in Fig. 30, in which the data flow is from the bottom to the top. Both the prompt trigger and the software triggers should provide reduction factors of order 100, so that approximately 1000 events per second out to  $10^7$  are archived.

The event size is expected to be about 0.5 MByte, so the  $10^5$  events/sec passing the prompt trigger lead to a data-flow rate of about 50 GBytes/sec off the detector into the computer ranch. The archival data rate is also quite substantial: 0.5 GByte/sec = 2 Terabytes/hour.

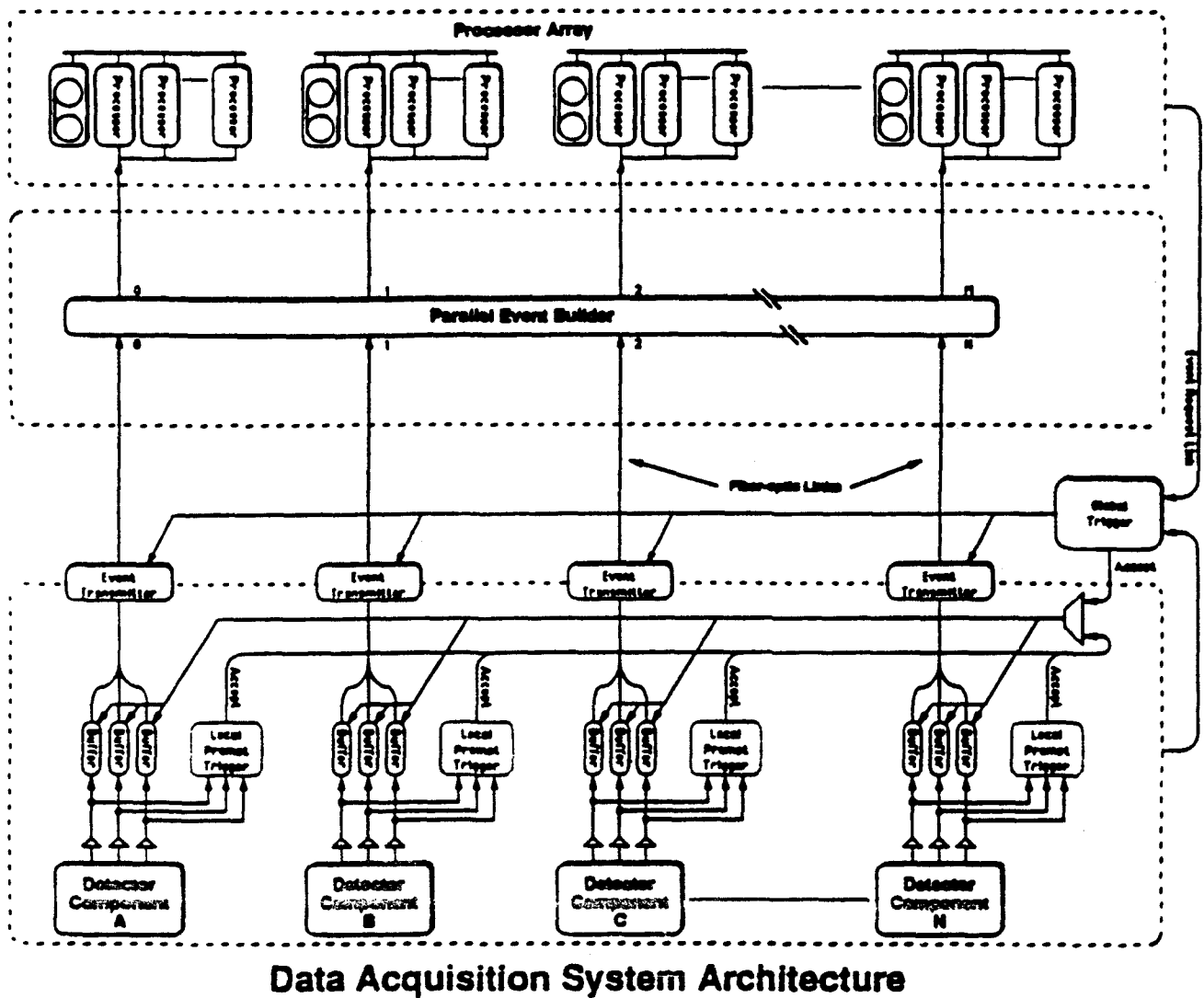


Figure 30: Data-acquisition architecture, I.

## 5.2 Triggers

There are four trigger scenarios that are presently being investigated: single electron, single muon, a high-luminosity  $J/\psi$  trigger, and a secondary-vertex trigger. Of these, only the  $J/\psi$  trigger could provide an overall rejection factor of  $10^4$  at the prompt level. The other three triggers are implemented partly in prompt-trigger hardware and partly in the online computer ranch.

### 5.2.1 Electron Trigger

The primary electron signal is subject to backgrounds from misidentified charged pions,  $\pi^\pm$ - $\pi^0$  overlaps, and photon conversions in the detector. Cuts on energy deposited in the electromagnetic calorimeter (both total energy and distribution among the longitudinal sections) are applied at the prompt level, along with a cut based on the preconverter to indicate

the presence of a charged track. These can provide about a factor of 50 event rejection, but are not effective against energetic-photon conversions. The software trigger will add information on vertexing and tracking to locate the origin of possible photon conversions, and will use the TRD to improve the rejection against charged pions.

### 5.2.2 Prompt Muon Trigger

The pad signals from the three muon-detector stations define a muon-track candidate by forming a projective prompt triple coincidence using hardwired logic on the muon detector. As seen from Table 20, the muon steel alone produces an event rejection of over 100. Additional rejection could be obtained at the prompt level by a coarse  $P_t$  cut. For this, the muon-pad triple coincidence can then be used to define a road through the Forward spectrometer to be searched for track hits. These track hits are fed into programmable logic arrays or microprocessors that determine whether there are any hit combinations consistent with tracks having a  $P_t$  above a given threshold. If any such combination is found, the event is passed on to the processor ranch. However, even in the ranch a muon-only trigger will not provide an overall event rejection of  $10^4$ , so must be supplemented by another trigger, such as the secondary vertex requirement.

The muon system must provide fast outputs for the prompt trigger, which may require additional detector elements with a more rapid response time than the 1-cm-drift tracking chambers.

### 5.2.3 Prompt High Luminosity $J/\psi$ Trigger

This trigger makes an invariant-mass cut on lepton pairs. A hardware processor can provide a event rejection factor of order  $10^4$  at the prompt level. Greater rejection is available using high-resolution analysis in the processor ranch. Hence this trigger could be used at luminosities greater than  $10^{32}$ , but is perhaps the only high luminosity trigger for  $B$  physics. This encourages us to design the experimental electronics for high luminosity.

### 5.2.4 Secondary-Vertex Trigger

At the prompt level, vertex information could be obtained in the nonbend plane via the aid of powerful local processors. However, the full benefit of a vertex trigger is likely available only in the processor farm, where information in the bend plane can be utilized. Hence, the secondary-vertex trigger may be more powerful as a final stage of the single-lepton triggers.

## 5.3 Data-Acquisition Architecture

The data-acquisition architecture is shown in Figs. 30 and 31. Briefly, the data from each detector subsystem is stored locally in analog storage buffers about 100-events deep during the 1.5-2  $\mu$ sec while the prompt trigger is being formed. If an event satisfies the prompt trigger, its data are moved to a second level of storage while the data are digitized and transmitted to the processor ranch. The digitization will take place on the detector (local VLSI ADC's) for most subsystems. In addition, local processing leading to data compaction may take place.

## BCD Trigger and Data Acquisition Architecture

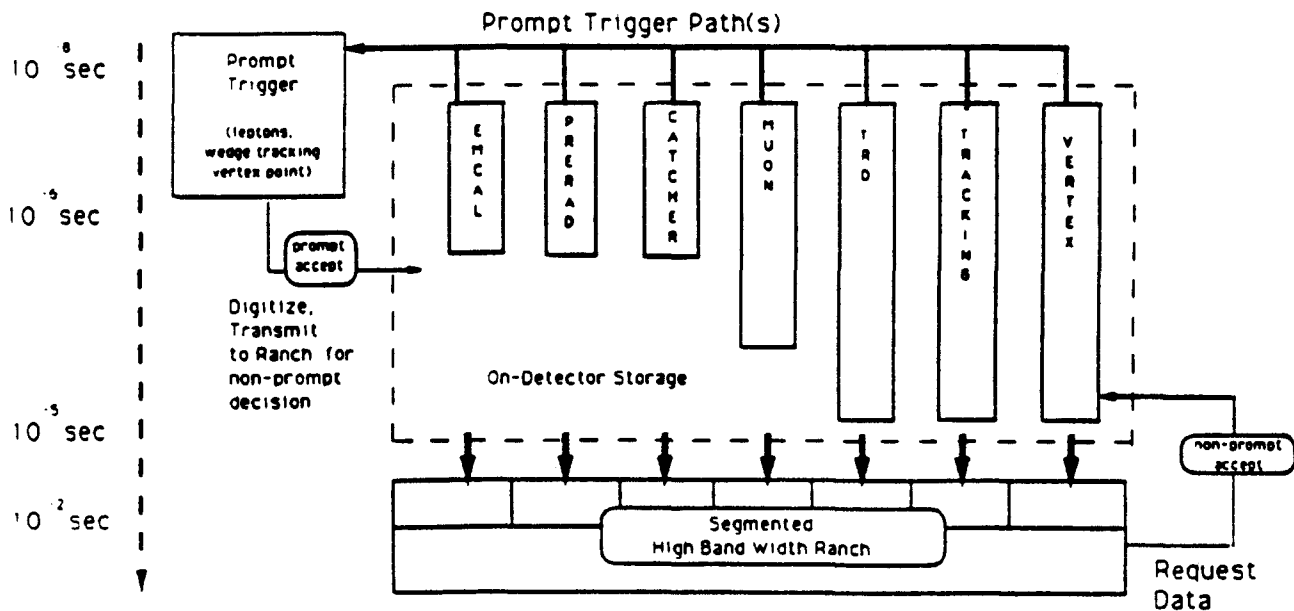


Figure 31: Data-acquisition-system architecture, II.

The data are driven from the detector on  $\sim 1000$  fiber-optic cables to the processor ranch at a rate of up to 500 GBytes/sec. Drivers for such data rates are commercially available today. However, this data rate is several orders of magnitude higher than in existing high-energy-physics experiments.

Before the events can be processed, the  $\sim 1000$  parallel event streams must be organized into the events themselves. This might be accomplished in either of two ways; in a special-purpose event-builder switch based on telecommunications technology,<sup>[84]</sup> or in the switching network of the processor farm itself should this network have sufficient bandwidth.

The special-purpose event builder is based on the 'barrel-switch' concept illustrated in Fig. 32. The event fragments on the input lines at the left are delayed by one clock cycle on each successive line. Then at every clock cycle, the switch rotates its contacts by one line, so that the fragments of one event on  $n$  input lines are all ordered serially on a single output line after  $n$  cycles. In the meanwhile,  $n - 1$  later events are in various stages of building. The switch required for the BCD would have a capability similar to that of a single 10,000-line telephone exchange.

In any case, the processor ranch itself must have a powerful network connecting the processors so that data may be sent in and out of the ranch at high rate. A sketch of such a processor network is shown in Fig. 33. The numerical processors are located at most, but not all, of the nodes of the network. Some nodes are reserved for data input and output. Various topologies of the processor and I/O nodes are possible, and are under study by us.<sup>[86]</sup> The most exciting possibility is that the input nodes could be connected directly to the detector, and the sophisticated routing capability of the network performs the event-building function described above.

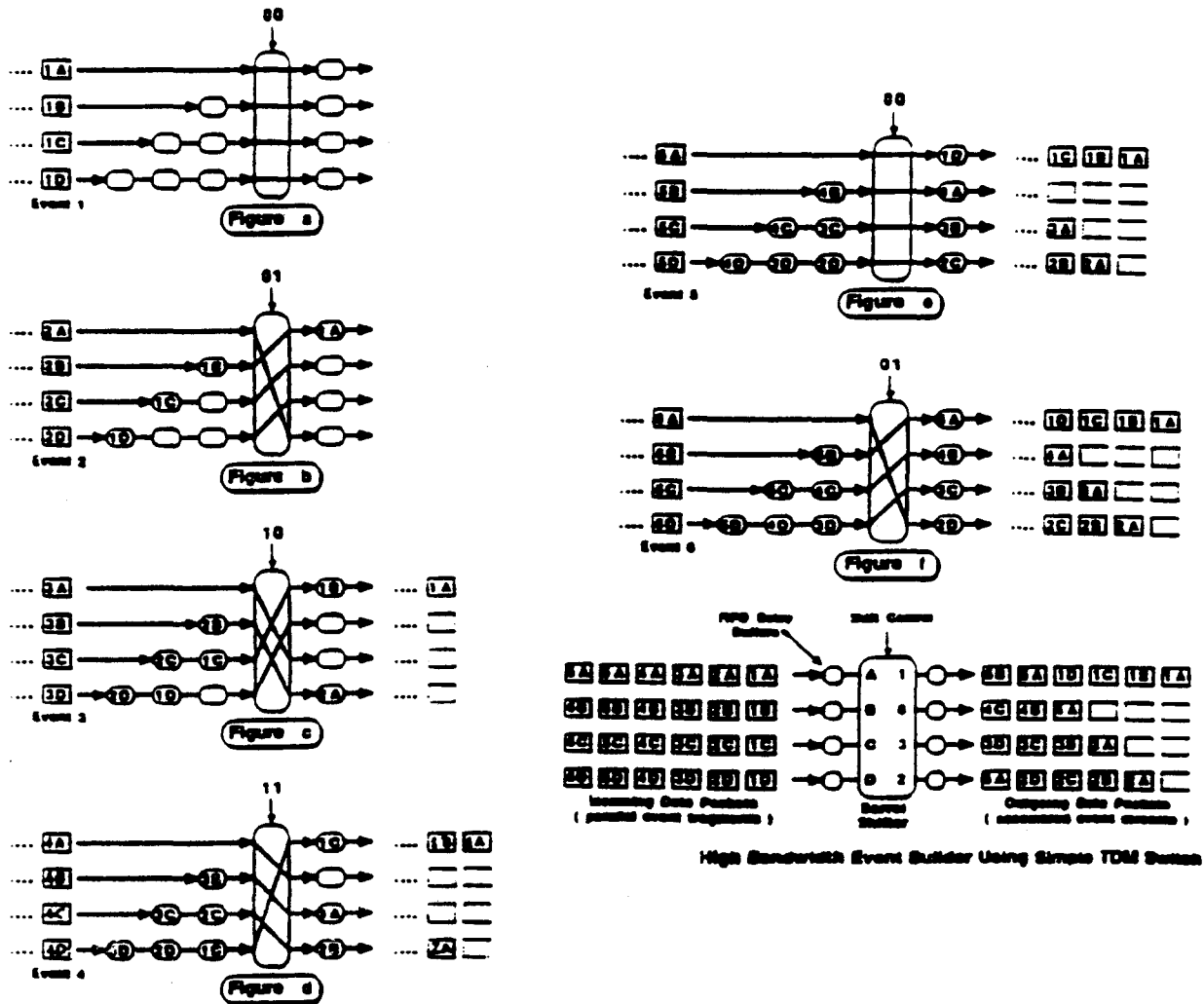


Figure 32: Principle of the barrel-switch event builder. See text for discussion.

### Online Processing Requirements – One TeraOPS

Some  $10^6$  events/sec must be processed by the computer ranch. From the experience of the CDF collaboration, a software trigger will require at least 10 sec of computing time on a 1 MOPS processor. If this number is also relevant for the BCD, we will need  $10^6$  MOPS/sec = 1 TeraOPS of processing power.

### Ranch Architecture

The simplest use of processors on the computer ranch is to have each processor executing an identical program that analyzes a single event.

A more sophisticated architecture may be preferable. Here the processor nodes are dedicated to specific tasks and do not attempt to resolve complete events and make a final trigger decision by themselves. Only part of an event is built for a particular processor, much of the event data remaining on the detector (in large buffers) until a partial software-trigger deci-

## Distributed Event Builder Model

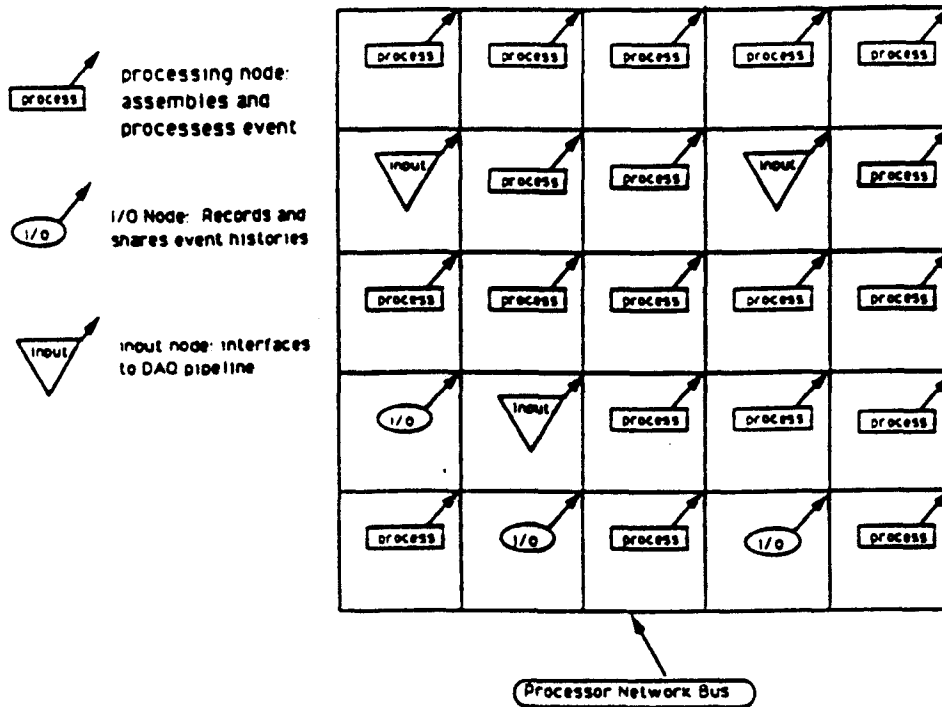


Figure 33: Distributed Event Builder Model

sions calls for more of the event. Blocks of processors may be assigned to the several types of triggers being implemented simultaneously. Some processors may carry their analysis much further than the others to provide detailed online monitoring.

### 5.4 Archival Mass Storage

The BCD anticipates recording at least 100 MBytes/sec to tape. With a compressed event size of 100k Bytes, 1 kHz could be recorded using contemporary technology. It is generally felt that 500 MBytes/sec would be an upper limit on the data archival rate due to sheer volume of data.

The E-Systems Garland Division has proposed a possible data-acquisition archival configuration which would satisfy these requirements. This configuration uses 19-mm helical-scan digital-video cartridges with a capacity of up to 190 GBytes/cassette and data transfer rates of 15-30 MBytes/sec. Fig. 34 presents capacities of robotized archival systems for automated data acquisition. In a year's running at 100 MBytes/sec, it is estimated that 1555 TeraBytes of data would be accumulated, requiring 2295 ft<sup>2</sup> of robotized floor area.



ON-LINE CAPACITY BANDWIDTH	DAYS				RECORDERS
	1	42	90	180	
100 MB/s	8.6 TB 78 SF	362 TB 506 SF	777 TB 1,180 SF	1,565 TB 2,296 SF	8
500 MB/s	43.2 TB 194 SF	1,814 TB 1,464 SF	3,888 TB 2,980 SF	7,776 TB 5,738 SF	22
1 GB/s	86.4 TB 364 SF	3,628 TB 2,903 SF	7,776 TB 5,676 SF	15,552 TB 11,451 SF	47
10 GB/s	864 TB 3,372 SF	36,288 TB 28,715 SF	77,760 TB 58,464 SF	155,520 TB 114,236 SF	364
100 GB/s	8640 TB 33,448 SF	362,880 TB 287,381 SF	777,600 TB 584,672 SF	1,555,200 TB 1,142,081 SF	3411

1 DAY = 86,400 SECONDS  
1 TB = 1 E12 BYTES

Figure 34: Specifications of a possible data-acquisition archival configuration.

## 5.5 Offline Computing Needs

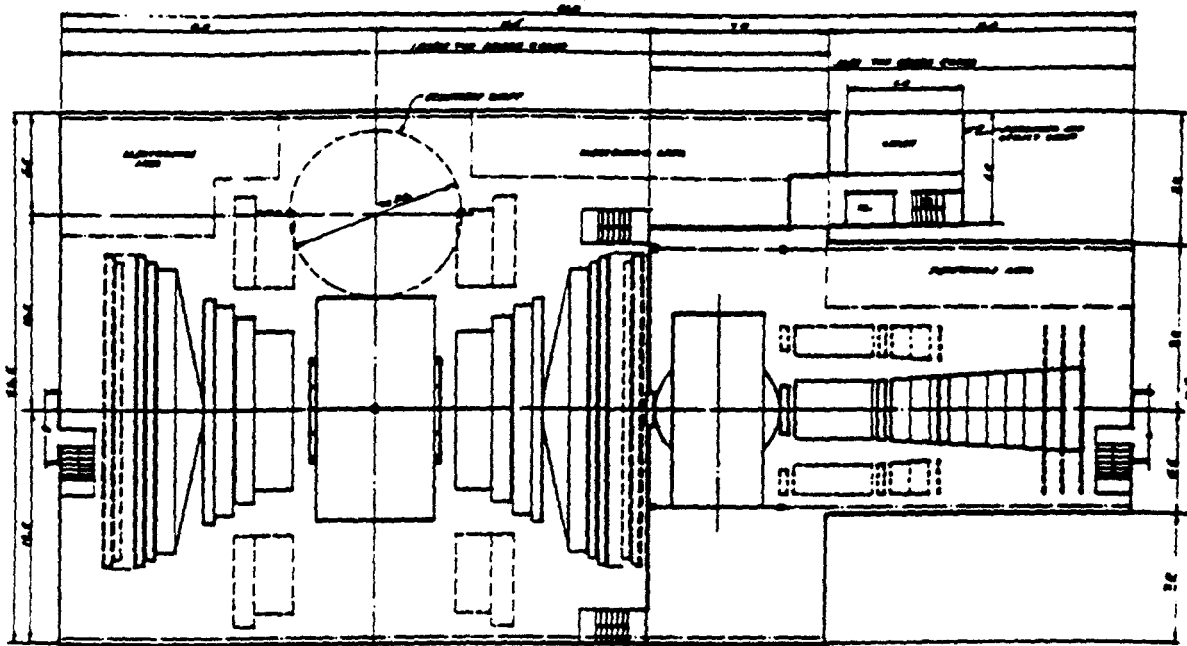
BCD requires sufficient offline computing resources to maintain a data-analysis rate equal to the archival data-acquisition rate on an annual basis. It is assumed that the online computer will be active calibrating detector subsystems, recording data and thus will be largely unavailable for offline analysis. Extrapolating from the CDF experience, the amount of computing needed to run BCD data through production analysis is about 10-50 GFlops to handle a data rate of 100 MBytes/sec to tape.

## 6 Collision Hall

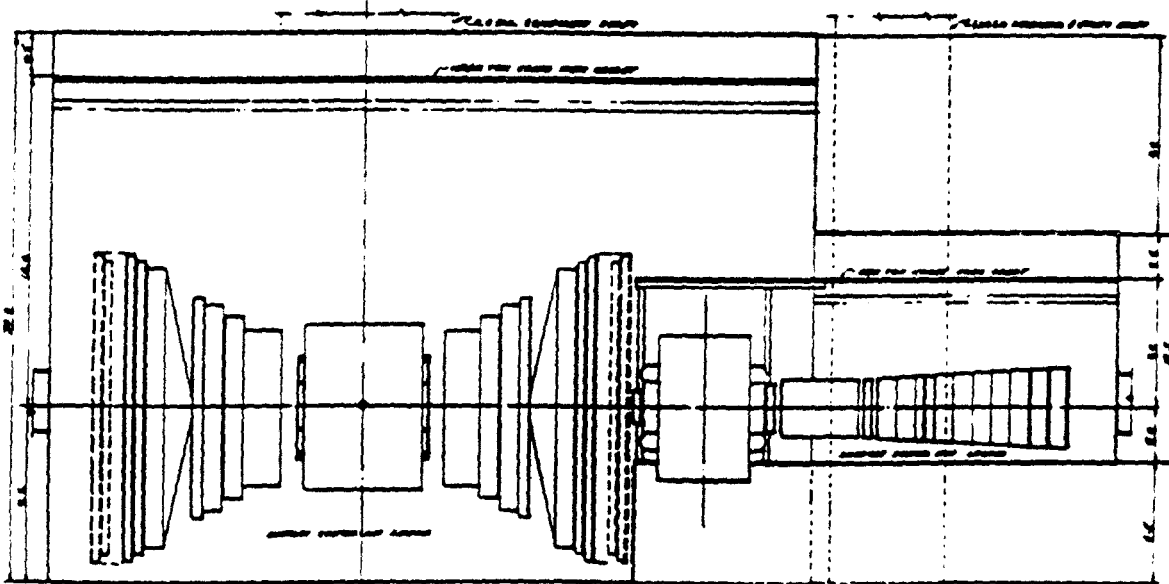
A plan and elevation view of the BCD Experimental Hall is shown in Fig. 35.

The portion of the hall housing the Central and Intermediate detectors is 28.5 m wide, by 40 m long, by 30 m high, and is served by a 150-Ton (136 tonne) bridge crane with a 15-Ton auxiliary hoist. The portion of the hall housing the forward detector is 14.5 m wide, by 16 m long, by 12.5 m high, and is served by a 50-Ton bridge crane with a 5-Ton auxiliary hoist. A 9-m diameter equipment shaft and a 6-m-square personnel & utility shaft connect directly into the hall without the need for horizontal tunnels.

An alternate configuration to that shown is a hall of constant cross section, 25 m wide, by 57 m long, by 30 m high, with a single 150-Ton bridge crane having a 15-Ton auxiliary



PLAN



ELEVATION

BCD EXPERIMENTAL HALL

Figure 35: BCD Experimental Hall.

hoist. The equipment and the personnel & utility shafts would be located to the side and connected to the hall by tunnels. The configuration shown in Fig. 35. has 1,372 m<sup>2</sup> of floor area and a volume of 32,942 m<sup>3</sup>. The alternate configuration would have 1,425 m<sup>2</sup> of floor area and a volume of 42,750 m<sup>3</sup>.

## 7 An Interim Experiment

No existing hadron-collider detector is optimized for *B* physics. The design concepts presented here should be tested on a modest scale before being implemented at the SSC. A good opportunity for this exists at Fermilab, where we intend to propose a 'mini-BCD' experiment for the C0 collision region. A preliminary detector configuration is sketched in Fig. 36, showing a central C-magnet that surrounds a vertexing and tracking system, augmented by two forward arms of particle identification. The tracking extends over  $|\eta| < 3.5$ , and the particle identification over  $1.7 < |\eta| < 3.5$ .

The mini-BCD is a significant physics instrument, as well as a proving ground for technology for the SSC. In addition to measuring numerous nonleptonic *B*-decay modes, the study of *B*<sub>s</sub>-*B*<sub>d</sub> mixing is a major goal of this detector.

PART	LD. °	VOL. m <sup>3</sup>	SP GRAV	total weight
Magnet Iron	1	7.14	7.85	56.09
Central Tracking	2	0.02	0.02	0.04
Central Vertex Detector	3	-	0.02	-
TRD	4	0.58	0.10	0.06
EM CAL	5	0.78	7.23	5.65
Lumen Monitor	6	-	-	-
Magnet Coil	7	0.86	8.91	7.65

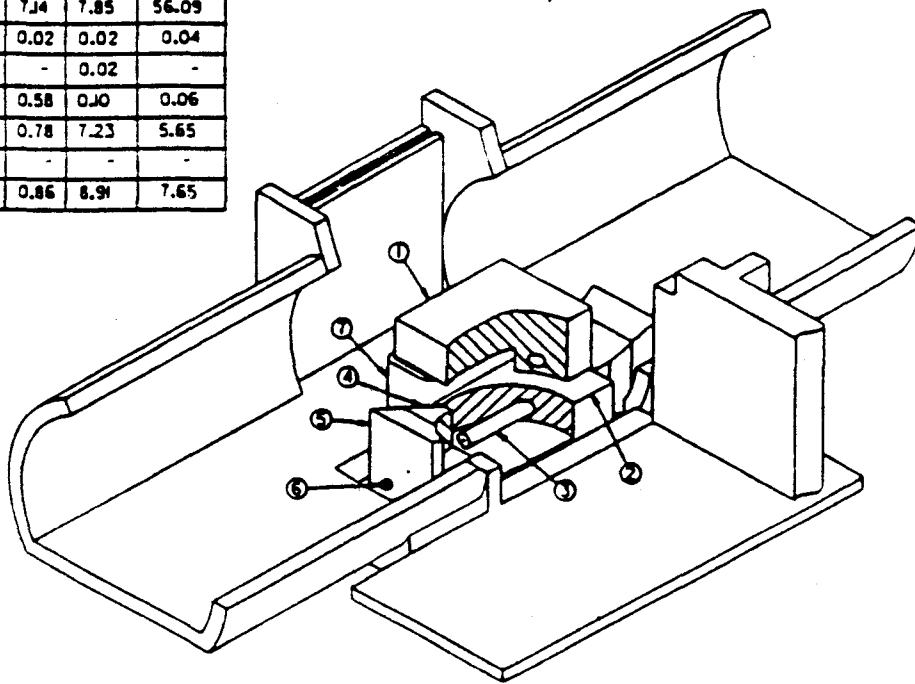


Figure 36: Sketch of a mini-BCD experiment to be proposed at Fermilab.

## 8 Milestones and Schedule

A schedule for major activities leading up to the construction of the BCD is shown in Fig. 37. This schedule depicts the project milestones that must be accomplished for phases of the design, engineering, procurement, fabrication, assembly, integration, and test of the experimental apparatus.

As indicated, the proposal-submittal timeframe correlates with R&D on subsystems, component, and integration. This provides for resolution of problem areas early on where the risk is minimized. The integration of a Mini-BCD at Fermilab with the SSC BCD schedule is shown to emphasize the flow of experience from the interim experiment to the SSC.

Details of subsystem fabrication and detector configuration are sketchy at present. A roughly serial subsystem-installation sequence is shown to highlight the effect of hall characteristics on detector construction. We believe that current schedules for the SSC Project-related facilities and support elements allow sufficient time to construct and install the BCD in the interaction hall in time for SSC turn-on.

## 9 Request for R&D Support

### 9.1 Vertex Detector

A fast, radiation-hard readout for *p-i-n* diodes is essential for the success of the BCD experiment. We request funding for Hughes to fabricate a version of the readout chip that is tailored for BCD. In addition, funding is required for the U C. Berkeley Space Sciences group to continue engineering the design.

Radiation damage is a crucial issue for the silicon detectors and electronics. Prototype readout electronics must be fabricated in radiation hard processes and then tested. We propose to fabricate circuits using the radiation hard process of, for example, Harris Semiconductor or IBM.

In collaboration with the silicon detector SSC subsystem development<sup>[88]</sup> we will contract with a U.S. manufacturer (possibly RETICON division of EG&G ORTEC) to fabricate double-sided AC-coupled detectors. We will test these detectors and the rad-hard electronics in the BCD test beam at Fermilab which has extensive instrumentation installed. Radiation exposures will also be made at Los Alamos (neutrons and protons), ORNL (Co<sup>60</sup> photons) and Rutherford Lab (spallation neutrons).

The people representing the above institutions are: G. Kramer (Hughes), C. Britton (ORNL), P. Skubic (Oklahoma), P. Karchin (Yale) and J. F. Arens and G. Jernigan (U.C. Berkeley, SSL).

### 9.2 Time of Flight

The performance of the TOF system will impact greatly the design of the RICH system for BCD. Without sufficient time resolution, the RICH system must be built with two radiators in the Central and Intermediate regions. One radiator will be used if 50-70-ps resolution with TOF can be achieved. The following issues must be answered in the near term.

BCD Preliminary Schedule

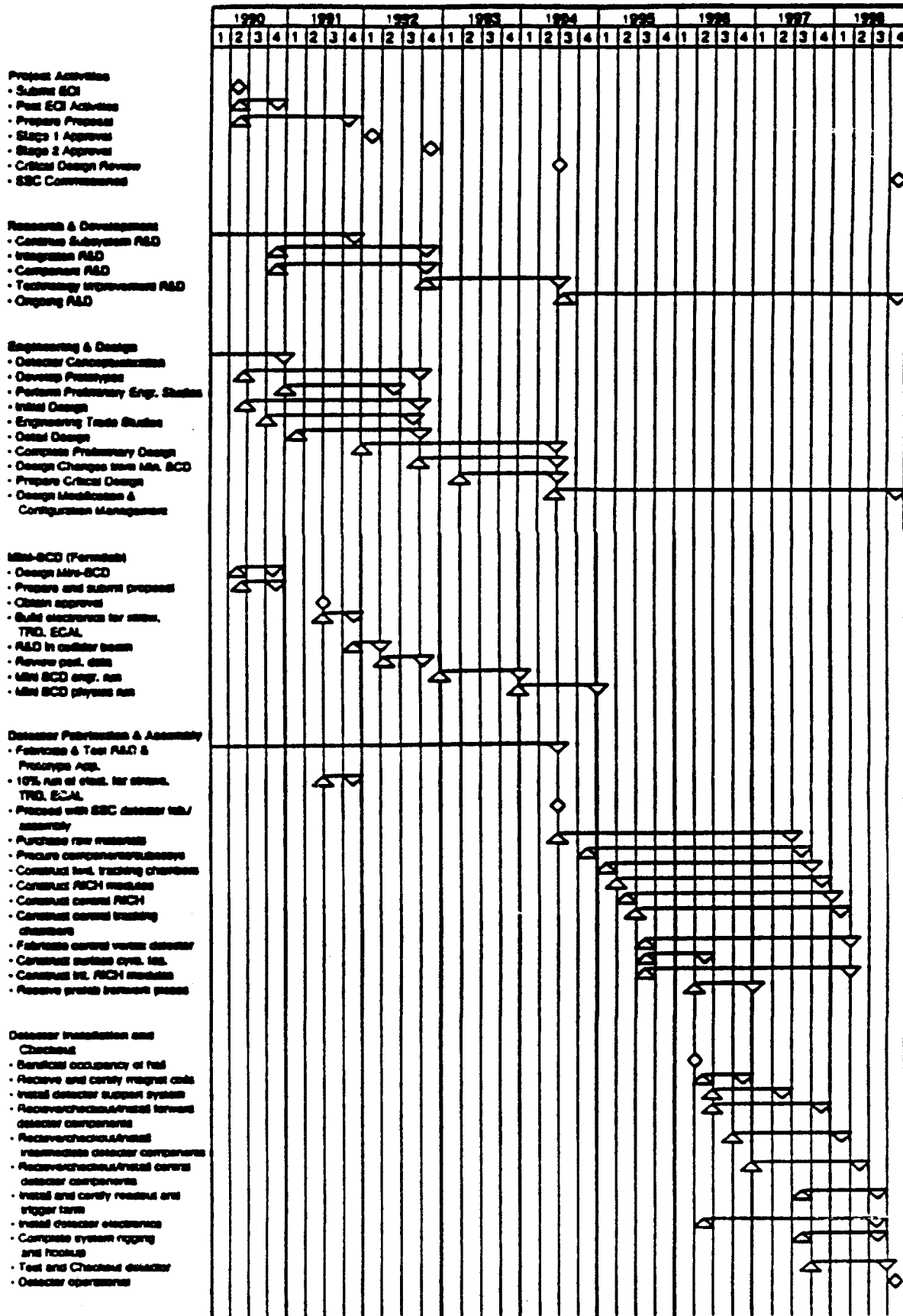


Figure 37: Schedule for the BCD.

Table 21: Summary of Vertex Detector R&D Costs and Commitments.

Task	Institutions	Cost (K\$)
<b>Fast <math>p-i-n</math> Diode Readout</b>		
design	Hughes	100
	U.C. Berkeley-SSL	50
fabrication	Hughes	50
<b>Radiation-Hard Circuits</b>		
3 rad-hard fabrication runs	ORNL	90
6 mos. engineering time	ORNL	60
rad. exposure and beam tests	Oklahoma, Yale	50
3 $p-i-n$ Diode Fabrications	Oklahoma, Yale	120
Total Vertex R&D Costs		520

1. Demonstrate that the time resolution for  $n$  samples scales like  $\sigma/\sqrt{n}$ , where  $\sigma = 150$  ps is the time resolution for one sample.
2. Verify that the scintillator and photomultiplier risetimes are fast enough to yield  $\sqrt{n}$  improvement.

The equipment funds requested for these studies are \$30K. These funds will be divided equally between M. S. Alam (S.U.N.Y. Albany) and D. H. Kaplan (U. of Oklahoma).

A further topic to be studied is the timing properties of scintillating fibers. We request \$15K for Y. Onel (U. of Iowa).

### 9.3 Trigger Simulation

We request funds for two programmers to perform simulations of electron triggers. The amount requested is \$100K including overhead, to be equally divided between A. J. Slaughter (Yale U.) and N. S. Lockyer (U. of Pennsylvania).

### 9.4 RICH

The BCD must identify  $\pi$ ,  $K$ , and  $p$  over a broad momentum range. We propose to design and build a small RICH counter which would test the performance and operation in a high rate environment. The counter would consist of a narrow gap, low pressure, high temperature photoconverter using TMAE and a readout pad chamber that provides good resolution. This smart pad chamber resolution impacts directly on the number of readout channels which dominates the cost and viability of a large area RICH detector. A working group is already committed to begin design work in June 1990.

Engineering support of \$45K and equipment funds of \$10K is requested for M. Adams (U. of Illinois, Chicago) to design, develop and build a 1-mm gap (7-ns drift), low pressure, 80°C TMAE photoconverter. Other people working with M. Adams to design and build the photodetector are S. Kwan (Fermilab), A. M. Lopez, A. Mendez, J. Millian, J. Palathingal (U. of Puerto Rico). A. Mendez and J. Millian are students working on a Master's Thesis on this topic.

Equipment funds for J. Morfin (Fermilab) of \$50K are requested for design construction of a 20 cm × 20 cm multistep avalanche photodetector with smart pad readout. Other people working with J. Morfin are B. Hoeneisen, C. Marin, and C. Jimenez (U. of San Francisco, Quito) and D. Wagoner (Prairie View A&M).

It is possible to increase the momentum coverage of the central RICH if a gas with  $\gamma_t \approx 5$  existed. We request \$30K to J. Morfin (Fermilab) for A. Katritzky (U. of Florida) to design a molecule with the correct properties.

Travel funds of \$20K for the U. of Puerto Rico and U. of San Francisco, Ecuador are to be placed in an account at the SSCL.

## 9.5 Computing

We have been developing simulation code for BCD throughout the past three years. This work will continue through proposal submission and beyond. The BCD collaboration will require 500-1000 MIPS of computing for simulations during the proposal preparation stage in late 1990-1991. The BCD group wishes to satisfy this computing need by sharing the planned 4000 MIPS of dedicated detector simulation computing resources at the SSCL.

Experience with the BCD GEANT vertex detector simulation has shown that 64-bit computing is required for accurate simulation of some detector features. Support of 64-bit GEANT simulation can be provided with a minimum of effort on machines with 64-bit real and integer representations. This simulation support is not widely available in the high energy physics community. The BCD collaboration believes that such computing capability is necessary and should be supported by the SSCL.

The BCD collaboration anticipates both remote and local use of the SSCL computing facilities. Convenient remote access is necessary for the collaborators throughout the country and abroad. We also anticipate having approximately four physicists on average working at the SSCL on BCD simulation during the next six months. This local effort will increase to 10 physicists by the fall of 1991. These physicists should be provided with desktop workstations.

## 10 Cost Estimate

Table 23 presents a preliminary cost estimate of the BCD detector. The total estimated cost in base-year-1990 dollars is approximately \$208M, including contingency and an allocation for engineering, design, inspection, and acceptance (EDIA).

The estimate was prepared using the parametric technique described in SSC-SR-1045 (Draft) Cost Estimates of the SSC Experimental Systems. This method characterizes the conceptual detector by mechanical and electrical components within the various subsystems and applies a unit price that has been determined by historical data from previously built

Table 22: Summary of R&D Costs.

Projects	Cost (K\$)
Vertex Detector	520
Time of Flight	45
Trigger Simulation	100
RICH	155
<b>Total R&amp;D Costs</b>	<b>820</b>

detectors. We have used a hybrid of the unit prices provided in SSC-SR-1045 and unit prices estimated by members of the collaboration and outside sources. The main point of departure from previous work is in the area of front-end electronics where we have prepared more detailed estimates. Also, system costs for items such as the preconverter, switch, triggering, and the computer were a result of tailoring to the specific needs of the BCD. The costs for analyzing magnets includes transportation and rigging of the Chicago Cyclotron Magnet (Forward magnet) from Fermilab, and an offer from Lawrence Livermore Laboratory to supply magnet coils free of charge (Central magnet). A contingency allowance was also included and is determined to be less for mechanical and systems costs than electronic costs. A traditional contingency in the 30% range is expected to be offset by further optimizations in the detector design and production costs.

Another way of summarizing the detector cost is by region:

1. Central and Intermediate tracking ..... \$27M
2. Central particle identification ..... \$14M
3. Intermediate particle identification ..... \$53M
4. Forward tracking and particle identification ..... \$18M
5. Data acquisition ..... \$36M
6. Contingency and EDIA ..... \$60M
7. Total ..... \$208M

The BCD detector estimate provided herein is for planning purposes and is appropriate for this EOI. The Proposal to be submitted in 1991 will include more detail as will be available after accomplishment of several milestones, R&D activities, and further engineering and design work.



Table 23: Cost estimate for the BCD detector in 1990 dollars. The estimate presents the mechanical and electronics costs separately for the various subsystems.

BCD DETECTOR COST ESTIMATE							
SUBSYSTEM	UNIT	QTY	COST CODE	UNIT COST \$K	SUBTOTAL \$K	TOTAL \$K	PERCENT OF TOTAL
VERTICAL DETECTOR							
MECHANICAL	METER**2	8	BCDM	1,000.0	8,000		
ELECTRONICS	KOHAN	1,300	BCDE1	5.0	6,500	12,000	3.9%
TRACKING							
CENTRAL							
MECHANICAL	KSTRANS	200	BCDM	33.0	6,600		
ELECTRONICS	KOHAN	200	BCDE2	32.8	6,560	13,160	6.3%
FORWARD							
MECHANICAL	KSTRANS	50	BCDM	33.0	1,650		
ELECTRONICS	KOHAN	6	BCDE2	32.8	208	1,858	0.9%
RICH							
CENTRAL							
MECHANICAL	METER**2	24	RICH1	175.0	4,200		
ELECTRONICS	KOHAN	27	BCDE3	10.0	270	4,470	2.1%
INTERMEDIATE							
MECHANICAL	METER**2	62	RICH1	175.0	10,850		
ELECTRONICS	KOHAN	155	BCDE3	10.0	1,550	12,400	6.0%
FORWARD							
MECHANICAL	METER**2	6	RICH1	175.0	1,050		
ELECTRONICS	KOHAN	27	BCDE3	10.0	270	1,320	0.6%
TRD							
CENTRAL							
MECHANICAL	METER**2	77	TRD1	21.0	1,617		
ELECTRONICS	KOHAN	15	BCDE3	10.0	147	1,764	0.8%
INTERMEDIATE							
MECHANICAL	METER**2	140	TRD1	21.0	2,942		
ELECTRONICS	KOHAN	28	BCDE3	10.0	282	3,224	1.5%
FORWARD							
MECHANICAL	METER**2	24	TRD1	21.0	488		
ELECTRONICS	KOHAN	12	BCDE3	10.0	123	621	0.3%
TOP							
CENTRAL							
MECHANICAL	METER**2	104	BCDM	8.0	834		
ELECTRONICS	KOHAN	15	BCDE4	150.0	2,250	3,084	1.5%
INTERMEDIATE							
MECHANICAL	METER**2	141	BCDM	8.0	1,128		
ELECTRONICS	KOHAN	15	BCDE4	150.0	2,250	3,378	1.6%
FORWARD							
MECHANICAL	METER**2	14	BCDM	8.0	112		
ELECTRONICS	KOHAN	8	BCDE4	150.0	1,125	1,237	0.6%
PREDCONVERTER	SYSTEM	1	BCDB1	5,000.0	5,000	5,000	2.4%
CALORIMETER							
CENTRAL							
MECHANICAL	TONNES	123	C1	16.5	2,063		
ELECTRONICS	KOHAN	7	BCDE5	180.0	1,272	3,335	1.6%
INTERMEDIATE							
MECHANICAL	TONNES	307	C1	16.5	5,088		
ELECTRONICS	KOHAN	14	BCDE5	180.0	2,438	7,504	3.6%
FORWARD							
MECHANICAL	TONNES	62	C1	16.5	1,353		
ELECTRONICS	KOHAN	8	BCDE5	180.0	1,087	2,420	1.2%
MUCH DETECTOR							
INTERMEDIATE							
MECHANICAL	TONNES	9,682	BCDM	2.0	19,324		
ELECTRONICS	KOHAN	68	BCDE6	51.0	4,468	23,788	11.4%
FORWARD							
MECHANICAL	TONNES	2,681	BCDM	2.0	5,362		
ELECTRONICS	KOHAN	28	BCDE7	55.1	1,543	6,907	3.3%
MAGNETS							
CENTRAL	SYSTEM	1	BCDE2	1,500.0	1,500		
FORWARD	SYSTEM	1	BCDE3	2,968.0	2,968	4,468	2.1%
SWITCH	SYSTEM	1	BCDB4	6,000.0	6,000	6,000	2.9%
TRIGGER	SYSTEM	1	BCDB5	10,000.0	10,000	10,000	4.6%
COMPUTERS	SYSTEM	1	BCDB6	20,000.0	20,000	20,000	9.6%
CONTINGENCY							
MECHANICAL	%	70,150	BCDC1	15.0%	10,523		
ELECTRONICS	%	32,319	BCDC2	25.0%	8,080		
SYSTEMS	%	45,469	BCDC3	15.0%	6,820	25,423	12.2%
EDIA @ 20%	%	73,381	EDIA1	20.0%	34,672	34,672	16.7%
DETECTOR TOTAL						288,833	100.0%

## 11 References

- [1] K. Foley *et al.*, *Bottom and Top Physics*, Proceedings of the Workshop on Experiments, Detectors and Experimental Areas for the Supercollider, (Berkeley 1987) R. Donaldson and G. Gilchriese editors.
- [2] K. Foley *et al.*, *A Beauty Spectrometer for the SSC*, Proceedings of the Workshop on Experiments, Detectors and Experimental Areas for the Supercollider, (Berkeley 1987) R. Donaldson and G. Gilchriese editors.
- [3] M. P. Schmidt, *B Physics at Hadron Colliders*, Proceedings of the Summer Study on High Energy Physics in the 1990's (Snowmass, 1988) S. Jensen, editor.
- [4] K.T. McDonald, *Prospects for Beauty Physics at Hadron Colliders*, AIP Conf. Proc. 185, 526 (1988).
- [5] P. Karchin, *Hadron Colliders as Bottom Factories*, in the Proceedings of the Meeting of the Division of Particles and Fields of the American Physical Society (Storrs, Connecticut, August, 1988), World Scientific; *Prospects for B-Physics at Hadron Machines*, in the Proceedings of the 24<sup>th</sup> Recontres de Moriond (Les Arcs, France, March, 1989), " '89 Electroweak Interactions and Unified Theories", J. Tran Thanh Van, ed., Editions Frontieres, 1989.
- [6] E. Fernandes *et al.*, *Lifetime of Particles Containing b Quarks*, Phys. Rev. Lett. 51, 1022 (1983).
- [7] N.S. Lockyer *et al.*, *Measurement of the Lifetime of Bottom Hadrons*, Phys. Rev. Lett. 51, 1316 (1983).
- [8] P. Nason, S. Dawson, and R.K. Ellis, *The Total Cross Section for the Production of Heavy Quarks in Hadronic Collisions*, Nucl. Phys. B303, 607 (1988); *The One Particle Inclusive Differential Cross Section for Heavy Quark Production in Hadronic Collisions*, Nucl. Phys. B327, 49 (1989).
- [9] H. Albrecht *et al.*, *Observation of  $B^0$ - $\bar{B}^0$  Mixing*, Phys. Lett. 192B, 245 (1987);
- [10] M. Artuso *et al.*,  *$B^0$ - $\bar{B}^0$  Mixing at the  $\Upsilon(4S)$* , Phys. Rev. Lett. 62, 2233 (1989).
- [11] H. Castro *et al.*, *Letter of Intent for the BCD, A Bottom Collider Detector for the Fermilab Tevatron* (October 7, 1988).
- [12] M. Bauer, B. Stech, and M. Wirbel, *Exclusive Non-Leptonic Decays of D-, D<sub>s</sub>-, and B-Mesons*, Z. Phys. C 34, 103 (1987).
- [13] See, for example, G. Bélanger *et al.*, *Weak Decays: Theoretical Summary*, Proceedings of the Summer Study on High Energy Physics in the 1990's (Snowmass, 1988) S. Jensen, editor, p. 339.
- [14] M. Bander, D. Silverman, and A. Soni, *CP Noninvariance in the Decays of Heavy Charged Quark Systems*, Phys. Rev. Lett. 43, 242 (1979).
- [15] L.-L. Chau and H.-Y. Chang, *B Decays without Final-State Charm Particles and CP Noninvariance*, Phys. Rev. Lett. 59, 958 (1987).
- [16] J.-M. Gérard and W.-S. Hou, *CP Nonconservation and CPT: Reassessment of Loop effects in Charmless B Decays*, Phys. Rev. Lett. 62, 855 (1989).
- [17] D. London and R.D. Peccei, *Penguin Effects in Hadronic B Asymmetries*, Phys. Lett. 223, 257 (1989); M. Gronau, *CP Violation in Neutral-B Decays to CP Eigenstates*, Phys. Rev. Lett. 63, 1451 (1989).
- [18] This section follows P. Krawczyk, D. London, R.D. Peccei, and H. Steger, *Predictions of the CKM Model for CP Asymmetries in B Decay*, Nucl. Phys. B307, 19 (1988).
- [19] First introduced by L. Miani, *CP Violation in Purely Lefthanded Weak Interactions*, Phys. Lett. 62B, 183 (1976); our notation follows L. Wolfenstein, *Parametrization of the Kobayashi-Maskawa Matrix*, Phys. Rev. Lett. 51, 1945 (1983).
- [20] The relevant box diagram was first calculated by J. Ellis, M.K. Gaillard, and D.V. Nanopoulos, *Left-Handed Currents and CP Violation* Nucl. Phys. B109, 213 (1976). That this leads to  $p/q$  being a pure phase and very small  $|\epsilon_B|$  seems to have been first noticed by J.S. Hagelin, *Weak Mass Mixing, CP Violation, and the Decay of b-Quark Mesons*, Phys. Rev. D 20, 2893 (1979).
- [21] First discussed by A.B. Carter and A.I. Sanda, *CP Nonconservation in Cascade Decays of B Mesons*, Phys. Rev. Lett. 45, 952 (1980); *CP Violation in B-Meson Decays*, Phys. Rev. D 23, 1567 (1981).

- [22] I.I. Bigi and A.I. Sanda, *Notes on the Observability of CP Violations in B Decays*, Nucl. Phys. B193, 85 (1981).
- [23] First discussed in L.-L. Chau and W.-Y. Keung, *Comments on the Parametrization of the Kobayashi-Maskawa Matrix*, Phys. Rev. Lett. 53, 1802 (1984).
- [24] J.G. Morfin and Wu-Ki Tung, *Parton Distribution Functions Determined from a Global Analysis of Deep Inelastic and Drell-Yan Scattering Data*, Fermilab-Pub-90/74.
- [25] F. Olness and Wu-ki Tung, Int. J. Mod. Phys. A2, 1413 (1987).
- [26] J. F. Arens et al., *SSC R&D Proposal: Development of Technology for Pixel Vertex Detector*, proposal to the SSC Laboratory (Sept., 1989).
- [27] W. Chen et al., *SSC Detector Subsystem R&D Proposal to Develop Track and Vertex Detector Based on Silicon Drift Devices*, (Oct. 1989).
- [28] M. Caccia et al., *A Si Strip Detector with Integrated Coupling Capacitors*, Nucl. Instr. and Meth. A260, 124 (1987).
- [29] P. Holl et al., *Strip Detectors with Capacitive Readout and a New Method of Integrated Bias Coupling*, IEEE Trans. Nucl. Sci. NS-36, 251 (1989). *The Aleph Minivertex Detector*, Nucl. Instr. and Meth. A257, 587 (1987).
- [30] G.R. Kalbfleisch, P.L. Skubic, M.A. Lambrecht, and C.D. Wilburn, *Charge Correlation Measurements from a Doubled-Sided Solid State Ministribe Detector*, IEEE Trans. Nucl. Sci. NS-36, 272 (1989).
- [31] G. Luts et al., *Low Noise Monolithic CMOS Front End Electronics*, Nucl. Instr. and Meth. A263, 163 (1988).
- [32] W. Buttler et al., *Noise Performance and Radiation Hardness of the CAMEX64 Analog Multiplexing Readout Chip*, Contribution to the XXIV International Conference on High Energy Physics (Munich, August, 1988).
- [33] J.T. Walker et al., *Development of High Density Readout for Diode Strip Detectors*, Nucl. Instr. and Meth. 226, 200 (1984).
- [34] A. Litke et al., *A Silicon Strip Vertex Detector for the MARK II Experiment at the SLAC Linear Collider*, Nucl. Instr. and Meth. A265, 93 (1988).
- [35] P.P. Allport, P. Seller and M. Tyndal, *A Low Power CMOS VLSI Multiplexed Amplifier for Silicon Strip Detectors*, Nucl. Instr. and Meth. A273, 630 (1988).
- [36] S. Kleinfelder et al., *A Flexible 128 Channel Silicon Strip Detector Instrumentation Integrated Circuit with Sparse Data Readout*, IEEE Trans. Nucl. Sci. NS-35, 171 (1988).
- [37] S. J. Watts, *CCD Vertex Detectors*, Nucl. Instr. and Meth. A265, 99 (1988).
- [38] S.L. Shapiro et al., *Silicon PIN Diode Array Hybrids for Charged Particle Detectors*, SLAC-PUB-4701 (September 1988).
- [39] S. Holland, *Fabrication of Detectors and Transistors on High-Resistivity Silicon*, Nucl. Instr. and Meth. A275, 537 (1989).
- [40] S. Parker et al., Nucl. Instr. and Meth. A275, 494 (1989).
- [41] T. Ohsugi et al., *Radiation Damage in Silicon Microstrip Detectors*, Nucl. Instr. and Meth. A265, 105 (1988).
- [42] D.E. Groom, *Radiation Levels in SSC Detectors*, Nucl. Instr. and Meth. A279, 1 (1989).
- [43] T. Kondo, *Radiation Damage of Silicon Devices by Neutrons and R&D for JCCD Readout*, Proc. High Energy Physics in the 1990's, Snowmass 1988, (World Scientific Publishing Co., 1989), p. 732.
- [44] H.F.-W. Sadrozinski, *Development of Radiation Hard Front-End Readout Electronics at UC Santa Cruz*, Proc. 5th Wire Chamber Conference (Vienna, Feb., 1989), Nucl. Instr. and Meth. (1989).

- [45] H. Ikeda and N. Ujiie, *Radiation Damage of Bipolar SST Due to Fast Neutrons*, Nucl. Instr. and Meth. , 508 (1989).
- [46] D.E. Dorfan, *A Fast Bipolar Microstrip Readout Chip*, Nucl. Instr. and Meth. A279, 186 (1989).
- [47] H. Mulderink, N. Michels, and H. Jöstlein, *Mechanical and Thermal behavior of a Prototype Support Structure for a Large Silicon Vertex Detector (BCD)*, Fermilab TM-1616 (August 23, 1989); H. Jöstlein and J. Miller, *Heat Resistance and Air-Pressure Drop in a Model of the BCD Silicon Vertex Detector*, Fermilab TM (Jan. 1990).
- [48] C. Lindenmeyer, *Proposed Method of Assembly for the BCD Silicon Strip Vertex Detector Modules*, Fermilab TM-1627 (Oct. 16, 1989).
- [49] GigaBit Logic 10G PicoLogic Family 10G040A MUX and 10G041A de-MUX.
- [50] H. Nishimoto, *Modulation Schemes for Very High Bit Rate Optical Transmission Systems*, invited paper, Optical Fiber Communication Conference (1990).
- [51] T. Susaki et al., *10-Gbit/s Optical Transmitter Module with Multiquantum Well DFB LD and Doped-Channel Hetero-MOSFET Driver IC*, Optical Fiber Communication Conference (1990).
- [52] M.J. Little et al., *The 3-D Computer*, Proc. IEEE International Conference on Wafer Scale Integration (San Francisco, January, 1989).
- [53] L.A. Roberts, *Monte Carlo Simulation of Silicon Vertex Detector for Bottom Collider Detector*, Fermilab preprint FN-488 (June, 1988).
- [54] M. Frautschi et al., *The Amy Inner Tracking Chamber*, Ohio State U. preprint (Oct. 1989), submitted to Nucl. Instr. and Meth.
- [55] C. Lu et al., *Proposal to the SSC Laboratory for Research and Development of a Straw-Tube Tracking Subsystem*, Princeton U. preprint DOE/ER/3072-56 (Sept. 30, 1989).
- [56] C. Lu et al., *Prototype Study of the Straw Tube Proportional Chamber*, Princeton U. preprint DOE/ER/3072-56 (Feb. 1990).
- [57] H.H. Williams et al., *SSC Subsystem Proposal for Front-End Electronics*, (Sept. 1989).
- [58] L. Callewaert et al., *Front End and Signal Processing Electronics for Detectors at High Luminosity*, IEEE Trans. Nuc. Sci. NS-36, (1989); F.M. Newcomer et al., *High Speed Bipolar Integrated Circuits for SSC Applications*, to be published in Nucl. Instr. and Meth.
- [59] R.L. Gluckstern, *Uncertainties in Track Momentum and Direction Due to Multiple Scattering and Measurement Errors*, Nucl. Instr. and Meth. 24, 381 (1963).
- [60] Proceedings of the SLC Workshop on Experimental Use of the SLAC Linear Collider, SLAC-247 (March, 1982), p. 158.
- [61] D.G. Cassel and H. Kowalski, *Pattern Recognition in Layered Track Chambers Using a Tree Algorithm*, Nucl. Instr. and Meth. 185, 235 (1981).
- [62] K. Kodam et al., *Hybrid Emulsion Spectrometer for the Detection of Hadronically Produced Heavy Flavor States*, Nucl. Instr. and Meth. A289, 146 (1990).
- [63] M. Kuhlen, *Study of Scintillating Fibers for a High Resolution Time of Flight System at the SSC*, CALT-68-1547 (1989).
- [64] J. Sequinot and T. Ypsilantis, *Photo-ionization and Čerenkov Ring Imaging*, Nucl. Instr. and Meth. 142, 377 (1977).
- [65] See, e.g., M. Adams et al.,  *$\pi/K/p$  Identification with a Large-Aperture Ring-Imaging Čerenkov Counter*, Nucl. Instr. and Meth. 217, 237 (1983); R.J. Apsimon et al., *A Ring Imaging Čerenkov Detector for the CERN Omega Spectrometer*, IEEE Trans. Nuc. Sci. NS-32, 674 (1985).
- [66] D.W.G.S. Leith, *Status of Čerenkov Ring Imaging*, Nucl. Instr. and Meth. A265, 120 (1988).

- [67] R. Arnold *et al.*, *A Ring Imaging Čerenkov Detector, the Delphi Barrel RICH Prototype*, Nucl. Instr. and Meth. **A270**, 289 (1998).
- [68] S. Majewski *et al.*, *Low-Pressure Ultraviolet Photon Detector with TMAE Gas Photocathode*, Nucl. Instr. and Meth. **A264**, 235 (1988).
- [69] R. Cherhib and A. Breskin, *On the Properties of Low-Pressure TMAE-Filled Multistep UV-Photon Detectors*, Nucl. Instr. and Meth. **A264**, 251 (1988).
- [70] H.O. Anger, *Instr. Soc. Am. Trans.* **5**, 311 (1966); C. Martin *et al.*, *Wedge-and-Strip Anodes for Centroid-Finding Position-Sensitive Photon and Particle Detectors*, *Rev. Sci. Instr.* **52**, 1067 (1981).
- [71] O. Siegmund *et al.*, *Application of the Wedge and Strip Anode to Position Sensing with Microchannel Plates and Proportional Counters*, *IEEE Trans. Nuc. Sci.* **NS-30**, 503 (1983).
- [72] S. Rescia, private communication.
- [73] A. Denison *et al.*, *Fermilab-Conf-84/134-4*; C.W. Fabjan *et al.*, *Nucl. Instr. and Meth.* **185**, 119 (1981).
- [74] D. Errede, H. Fenker, P. Mantsch, and M. Sheaff, to be submitted to *Nucl. Instr. and Meth.*
- [75] A.M. Lopes and J.C. Palathingal, *Optimization of the Transition Radiation Detector*, BCD internal note.
- [76] T. Coane *et al.*, *Scintillator Based Calorimetry for the SSC*, SSC Subsystem Proposal (Oct. 1989).
- [77] D.W. Hertzog *et al.*, *A High Resolution Lead/Scintillator Fiber Electromagnetic Calorimeter*, U. Illinois Pre-print No. Ill-(NPL)-90-001 (1990), submitted to *Nucl. Instr. and Meth.*
- [78] H.P. Paar, *Status of Scintillating Fiber Calorimetry*, Plenary talk, EFCA Study Week on Instrument Technology for High Luminosity Hadron Colliders (Barcelona, Spain, 14-21 September 1989).
- [79] G. Battistoni, *et al.*, *Nucl. Instr. and Meth.* **152**, 423 (1978); **164**, 57 (1979); **176**, 297 (1980); **202**, 459 (1982); **217**, 345 (1983).
- [80] K. Lau and D. Hungerford, *et al.*, private communication, 1990.
- [81] R. Santonico and R. Cardarelli, *Development of Resistive Plate Counters*, *Nucl. Instr. and Meth.* **187**, 377 (1981); R. Cardarelli, R. Santonico, A. Di Biagio, and A. Lucci, *Progress in Resistive Plate Counters*, *Nucl. Instr. and Meth.* **A263**, 20 (1988); M. Bertino, *et al.*, *Performance of Resistive Plate Counters at Beam Flux up to 140 Hz/cm<sup>2</sup>*, *Nucl. Instr. and Meth.* **A283**, 654 (1989).
- [82] A. Bodek, *Punchthrough in Hadronic Shower Cascades, Muon Identification, and Scaling Laws for Different Absorbers*, Univ. of Rochester preprint UR 911, ER13065-412 (April 1985).
- [83] E. Barsotti *et al.*, *Digital Triggers & Data Acquisition Using New Microplex & Data Compaction IC's*, *Proceedings of the Workshop on High Sensitivity Beauty Physics at Fermilab* (Nov. 11-14, 1987) J. Slaughter, N. Lockyer, M. Schmidt, editors, p. 369.
- [84] M. Bowden *et al.*, *A High-Throughput Data Acquisition Architecture Based on Serial Interconnects*, Fermilab preprint (Nov. 1988).
- [85] J. Rattner, in *Proceedings of the Workshop on B Physics at the SSC* (DeSoto, June 1989).
- [86] L.D. Gladney *et al.*, *Proposal to SSC Laboratory for Research and Development for a Parallel Computing Farm* (Oct. 1989).
- [87] L.D. Gladney *et al.*, *Initial Experience with the Intel i860 Microprocessor*, U. Penn preprint UPR-0184E (March, 1990).
- [88] A.J. Weinstein *et al.*, *Subsystem R&D Proposal to Develop a Silicon Tracking System*, proposal to the SSC Laboratory (Sept. 1989).